UNIVERSITY OF Southampton

University of Southampton Research Repository

Copyright © and Moral Rights for this thesis and, where applicable, any accompanying data are retained by the author and/or other copyright owners. A copy can be downloaded for personal non-commercial research or study, without prior permission or charge. This thesis and the accompanying data cannot be reproduced or quoted extensively from without first obtaining permission in writing from the copyright holder/s. The content of the thesis and accompanying research data (where applicable) must not be changed in any way or sold commercially in any format or medium without the formal permission of the copyright holder/s.

When referring to this thesis and any accompanying data, full bibliographic details must be given, e.g.

Thesis: Rory Oliver Brown (2019) "Modelling decretion discs in Be/X-ray binaries using Smoothed Particle Hydrodynamics", University of Southampton, Department of Physics and Astronomy, PhD Thesis, 152.

Modelling decretion discs in Be/X-ray binaries using Smoothed Particle Hydrodynamics

Rory Oliver Brown

A thesis presented for the degree of
Doctor of Philosophy

Department of Physics and Astronomy
University of Southampton
UK
May 2019

UNIVERSITY OF Southampton

Research Thesis: Declaration of Authorship

Print name:	RORY BROWN

Title of thesis:	Modelling decretion discs in Be/X-ray binaries using Smoothed Particle Hydrodynamics

I declare that this thesis and the work presented in it is my own and has been generated by me as the result of my own original research.

I confirm that:

1. This work was done wholly or mainly while in candidature for a research degree at this University;
2. Where any part of this thesis has previously been submitted for a degree or any other qualification at this University or any other institution, this has been clearly stated;
3. Where I have consulted the published work of others, this is always clearly attributed;
4. Where I have quoted from the work of others, the source is always given. With the exception of such quotations, this thesis is entirely my own work;
5. I have acknowledged all main sources of help;
6. Where the thesis is based on work done by myself jointly with others, I have made clear exactly what was done by others and what I have contributed myself;
7. Either none of this work has been published before submission, or parts of this work have been published as: [please list references below]:

Brown R. O., Coe M. J., Ho W. C. G. and Okazaki A. T., 2018, MNRAS, 477, 4810
Brown R. O., Coe M. J., Ho W. C. G. and Okazaki A. T., 2019, MNRAS, 486, 3078

Signature:		Date:	19/02/2019

Abstract

Be stars are dynamic systems even when completely isolated. Variabilities in the emission of these stars across all wavelengths are observed with periods ranging from a few minutes to many decades. Be stars are generally accepted to be surrounded by a decretion disc that gives rise to a number of these observable variabilities. The fact that this disc must be formed of material that is ejected from the surface of the star requires a complex mechanism that is still not fully understood. Be stars coupled with a compact object companion in a Be/X-ray binary have exhibited a large variety of complex behaviour. As Be/X-ray binaries are also the largest population of high mass X-ray binaries, they are a valuable resource for the investigation of the extreme physics of compact objects.

In this thesis, a code that implements the computational method of smoothed particle hydrodynamics (SPH) is used to model Be/X-ray binaries. SPH simulations have a resolution that is dependent on the density of individual regions. Thus, SPH is suited to modelling the circumstellar discs of Be stars because there is a considerable range between the maximum and minimum densities. Such a model can describe the properties of the disc in detail during binary interactions and allows a comparison to observable Be/X-ray binaries.

This thesis builds upon the previous work that has been done to investigate the properties of the circumstellar discs of Be stars. It begins with an investigation of a broad range of disc properties. The same simulations are then shown to agree with observationally determined relationships between the Be star's disc size, the orbital period and the semi-major axis of the binary. The Be/neutron star binary SXP 5.05 is then targeted with simulations attempting to reproduce the observations of the I-band and X-ray flux during a large optical outburst that occurred in 2013. It is found that the outburst can be replicated by a sudden and considerable increase in the mass ejection of the Be star. Be/X-ray binaries with different compact object companions are then modelled. The simulations agree with previous suggestions that Be stars with black hole companions have smaller discs and are fainter X-ray sources. Finally, the observational implications gleaned from these simulations and the possibilities of future work are considered.

Contents

List of Figures

List of Tables

Acknowledgements

A PhD is an undertaking that not only takes a long time to complete but also a considerable amount of perseverance and possibly even a part of the person undertaking it. It goes without saying that I have not completed this process without the support and aid of a large number of wonderful people. I would like to take the time in this section to thank all these people.

Firstly, I would like to acknowledge the support from the Engineering and Physical Sciences Research Council Centre for Doctoral Training grant EP/L015382/1. I also acknowledge the use of the IRIDIS High Performance Computing Facility, and associated support services at the University of Southampton, in the completion of this work. Numerical computations were also performed on the Sciama High Performance Compute (HPC) cluster which is supported by the ICG, SEPNet and the University of Portsmouth.

It should be obvious that my supervisors, Wynn Ho and Malcom Coe, have been of great help. I would like to thank them for all their advice and the considerably large time they have spent helping with my difficulty in writing. I feel lucky to have had supervisors who have been happy to meet every week and have agreed to help with my work every step of the way.

Atsuo Okazaki has made a huge impact on my work throughout my PhD. Not only is he the one from which the code was received (the code that produced most of my work) but he has also been a fantastic source of feedback and discussion throughout the years. I would like to thank him for always being welcoming and understanding. I would also like to thank him for making my stay in Japan more comfortable when I visited to work with him. Atsuo Okazaki has also been an inspiration in terms of his character and work.

I would like to thank Phil Charles and Ignacio Neguerela for their participation in my viva and for all the helpful comments they made on my thesis.

There are countless colleagues in the department who have eased the difficulties of every day work and provided insight for my work. If any of you are reading this, thank you for being a part of my life for the last four and a half years!

Firstly, I will thank those who were in my office specifically. Jamie Court, who was on my neighbouring desk and my housemate for the final year, has been of great help. He has always been extremely knowledgeable in a huge variety of astronomy and I could always count on him to know something about anything that I was not sure about. I must also thank Jamie for being a source of laughter and fun throughout my time in the department. Peter Boorman, whom is in general a delightful person, has always been very kind and helpful. Once again, he is another person I could ask for discussion on a wide variety of topics and to offer strange treats that he acquired. I should also mention his wonderful baking that he would regularly bring to the department. Adam Hill has always been quick to jump in and help on any programming issues. He truly has been of great help in Python and in the module I took in my first year that he lectured. I think he would have been a fantastic academic. Michael Johnson was a great source of fun and good conversation in the department. I enjoyed his presence (despite some of his time being dedicated to computer science and not physics) and am sure he will continue to be a cool guy. Dominic Ashton and John Paice, whom I only knew for a year, have both beena welcome addition to the office and I wish them the best in their PhDs.

There are many of those outside of my office that I have cherished the company of. One of these people is Triana Almeyda, who has been a wonderful friend and a helpful colleague. She has not only offered support in some times I have found very difficult but also provided fantastic advice and insight at multiple times during the latter part of my PhD, after I had the pleasure of meeting her. I have no doubt she will go on to be a fantastic academic and I wish her the best of luck in her career. I would like to thank Bella Boulderstone for her infectious positive energy and general repsonsibility in the department. She has always tried to help other students and I hope she continues to be such an upstanding member of the department. John Coxon must be thanked for providing a welcoming and friendly presence and for every fantastic conversation I have had with him. Stephen Browett was always a good friend and fantastic company. Bella, John and Stephen were a large part of me feeling more welcome to the department as a whole. I would like to thank Pip Grylls for making me laugh often and for his friendship, despite him accusing me of being nice for an agenda. I thank Sam Mangham for always being a helpful and kind person and for offering help at multiple stages of my PhD. David Williams needs to be thanked for his energetic attitude and unending energy during his studies in the department that inspired me to do better. I would like to thank Alessandra Constantino for being a wonderful friend to me and for often putting a smile on my face. I thank Charlotte Angus and Phil Wiseman for their repeated contributions of cute GIFs and articles and for the fact that I have only had positive and wonderful interactions with both of them. I would like to thank Victoria Lepingwell for her top-notch banter and for being an inspiration. I would

like to thank Christian Knigge for providing a great deal of help during my first two vivas and providing vital insight and fantastic discussions.

There are so many more members of the department that have been of great influence and for largely the same reason: they are all wonderful people and have been helpful whenever I have needed aid. To prevent this section from becoming a document of its own, I shall simply just thank the remainder of the department.

I would like to thank my colleagues within the NGCM for making the first year of my PhD bearable. These colleagues include Ioannis Begleris, Paul Chambers, Bob Entwistle, Stephen Gow, Josh Greenhalgh, James Harrison, Jan Kamenik and Jonathan Waters. The initial directors of the the NGCM also did a large amount for me in the first year and so I must thank Ian Hawke and Hans Fanghor.

I must also thank Alex Carciofi and Amanda Rubio for discussion on the matter of radiative tranfer and HDUST.

I would like to thank Peter Prince and Emily Nixon for their support during some hard times and for always offering me a place to stay whilst I am in Southampton. I also thank Alex Hutson for similarly being a wonderful friend during difficult times. I cannot go without thanking my friends outside of Southampton who have always made me feel like I have a second home. Michael Milligan and his partner Louise Blampied have been a unbelievable influence on my life for the last 14 years and I cannot thank them enough for it. Joshua Barr, Martin Cole, Willis Delamare, Stephen Dunne and Shane Sammut have also been a large part of my life for the last 14 years and must be thanked accordingly.

Finally, I would like to thank my family. Firstly, my brother for always being a sound influence and voice in my life and for being generally supportive. I must thank both of my parents for being heroes to me and being excellent role models in all aspects of life. My Mother, whom has always been there for me, I cannot thank enough for everything she has done and I am sure she will continue to do. My father, whom was one of the most gentle and kind people I have ever had the pleasure of knowing, unfortunately passed away in the first year of my PhD. I hope that in finishing this, I will have done well by him. May he rest in peace.

Chapter 1

Introduction

The focus of a considerable amount of astronomical research is to understand the extreme physics of compact objects (white dwarfs, neutron stars and black holes) but observing them directly is very difficult. Therefore, the best method to investigate compact objects is to observe their interactions with infalling matter, i.e. accretion. An X-ray binary is one of the most abundant kinds of system that accommodates an accreting compact object.

Be/X-ray binaries are the largest population of high mass X-ray binaries and consist of a B-type star and a compact object. The Be star possesses a circumstellar disc that arises from the ejection of matter from the surface of the star. The disc is dynamic in nature and thus provides an extensive assortment of possible interactions with the compact object.

Computational methods have developed considerably in the last few decades to include comprehensive means to model the dynamics, temperature and emission of the Be star's circumstellar disc. This has led to the development of a theory that encapsulates the features of the disc. However, there is still more work to be done in order to fully understand the wide variety of observed variabilities.

In this thesis, the behaviour of Be star discs are examined in a variety of cases. The general properties of Be/neutron star binaries are considered with a focus on steady state systems allowing for a broad comparison. A distinct Be/X-ray binary system, SXP 5.05, is modelled during its particularly rare outburst event that occurred in 2013. Comparisons are then made between black holes and neutron stars when coupled with Be stars in a binary, highlighting some of the features seen in the first confirmed Be/black hole binary, MWC 656. All of the work builds on the previous applications of hydrodynamical models to Be/X-ray binaries and provides further evidence for the currently accepted disc theory for Be stars.

1.1 Be stars

Be stars are non-supergiant B spectral type stars that have, or have had at some time, one or more Balmer lines in emission (Jaschek and Egret, 1982). This population of stars contains some of the brightest stars in the sky. For example, α Eri (B3 V) is the tenth brightest star in the sky when ordering by V-band magnitude, with an apparent magnitude of $m_{\mathrm{V}} = 0.40 - 0.46$ (Samus et al., 2009). In comparison to many other main sequence stars, Be stars have high rates of mass outflow, with a median of $\sim 10^{-10}\mathrm{M}_{\odot}\,\mathrm{yr}^{-1}$) estimated from simulations. They also rotate very quickly (Slettebak, 1988), with critical fractions of $W \geq 0.6$ (Frémat et al., 2005) and some even exceeding the critical limit entirely (Rivinius, Štefl and Baade, 2006). The critical fraction, W, is defined as

$$W = \frac{v_{\mathrm{rot}}}{v_{\mathrm{kep}}}, \tag{1.1}$$

where v_{rot} is the rotational velocity at the equator and v_{kep} is the Keplerian orbital velocity at the equator. A star is rotating critically when $v_{\mathrm{rot}} = v_{\mathrm{kep}}$. This rapid rotation, in addition to non-radial pulsations, is thought to lead to a diffuse and gaseous circumstellar disc (Rivinius, 2000). This is commonly referred to as a decretion disc. The disc is the dominant source of material for accretion onto a binary companion, because the stellar wind of a Be star is generally weak. The understanding of these systems has improved greatly over the last few decades due to large public databases of photometry, polarimetry and spectroscopy, complimented by the advancement of computational methods.

This section discusses the history and the distinct features of Be stars. Firstly, the discovery and classification of Be stars is outlined. Then the emission of Be stars is briefly discussed, including its dynamical behaviour. Finally, there is an examination of both the mechanisms which are considered to give rise to the ejection of matter from the surface of the Be star: rapid rotation and non-radial pulsations.

1.1.1 Discovery and classification

Be stars were first discovered by Secchi (1866), with an observation of γ Cas (B0.5 IV) exhibiting a Hβ emission line that was brighter than expected of a B-type spectrum. For the next 65 years, all stars with B-type spectra and Balmer line emission were considered part of the same population of stars. Struve (1931) then eliminated stars with P Cygni profiles and attributed the spectra of some stars to binarity, such as β Lyr (B8). The upper main sequence objects (those in luminosity

classes V to III) still conforming to the criteria were suggested by Struve to be rapidly rotating stars. Struve suggested that this rotation leads to ejection of matter from the star at the equator, thus forming a Keplerian disc that revolves around the star. This disc is responsible for the Balmer emission lines seen in the spectrum. Struve also noted that the rotation of the star would lead to it being warped into a "lens-shaped" body. The suggestion of a circumstellar disc at the star's equator led to Be stars being unified with shell stars. Shell stars refer to stars that exhibit Balmer lines with absorption cores much more sharp than one would expect from the width of normal photospheric lines. Struve suggested that shell stars are simply a Be star which is observed edge-on, or in other words, through the disc. When the entire length of the disc is along the observer's line of sight, one would see narrow absorption lines (illustrated in Figure 1.1). This geometry was eventually confirmed through interferometric observations (Quirrenbach et al., 1994).

A more formal definition of Be stars was proposed by Jaschek and Egret (1982) and then modified by Collins (1987) thus replacing "hydrogen lines" with "Balmer lines". This minor modification is important because early main sequence B stars can produce infrared hydrogen lines from photospheric emission alone (Zaal et al., 1999). The classical definition is as follows:

> Be stars are non-supergiant B spectral type stars that have, or have had at some time, one or more Balmer lines in emission.

This definition is still commonly used despite being a very broad statement. The aim of this definition is to capture only the stars that are capable of forming their own discs but technically any B-type star with circumstellar material of a sufficient density ($\geq 10^{-13}$ g cm^{-3}) falls within this classification. This is because circumstellar gas above such a density (and thus of sufficient equilibrium temperature) always exhibits Balmer line emission when orbiting a B-type star.

Be stars are capable of exhibiting both a standard photospheric emission spectrum expected of a B-type star and a much broader emission spectrum with tens of Angstroms in Hα equivalent width. What is even more distinct about Be stars is their ability to vary between these two states of emission over a matter of years. This is why it is necessary to contain the statement "or have had" in the classical definition because if a B-type star is not currently displaying Balmer lines in emission, it does not mean that this star is not capable of forming a disc. Thus, once a star is classified as a Be star, it remains one even if it ceases to exhibit the defined features. This also means that a B-type star that has never been classified as a Be star, could at any time become one (such as δ Sco).

O-type stars exhibiting Balmer line emission are also classified equivalently to Be stars because they are also upper main sequence stars and have morphologically similar spectra. Most are of late O subtype and close to the B star range (Conti

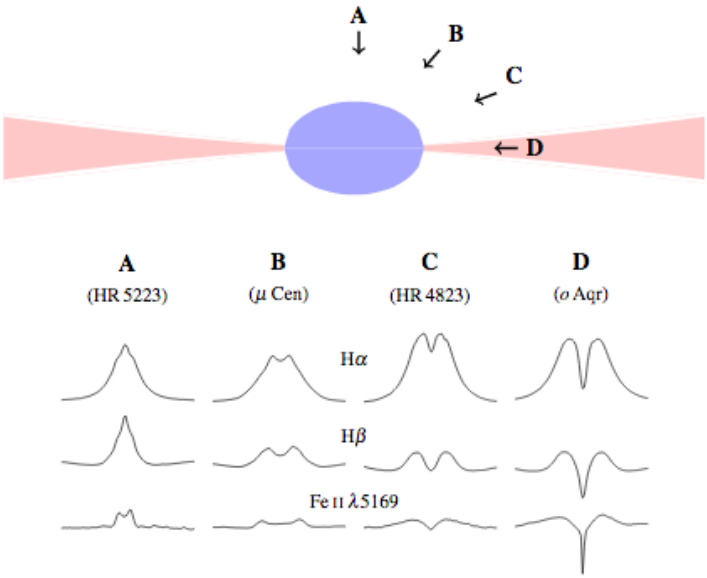

Figure 1.1: Figure 1 from Rivinius, Carciofi and Martayan (2013). It illustrates the effect of viewing a Be star and its disc at different viewing angles. The top image shows the "lens-shaped" Be star in blue with the surrounding flared circumstellar disc in red. The lower diagrams show examples for three line emission profiles when viewed at the four angles specified, A through D.

and Leep, 1974; Negueruela et al., 2004). Technically, A and F-type shell stars exist and some even show weak Hα emission (Slettebak, 1986; Waters et al., 1988). Hence, there are objects outside of the classical definition that may possess circumstellar discs and other features similar to Be stars.

1.1.2 Spectral type and mass

Following the definition above, only stars with B-type spectra can be classified as a classical Be star. In a catalogue given by Jaschek and Egret (1982), there are Be stars of all subtypes from B0-B9. There are more Be stars of earlier spectral class but this could be an observational bias as they are hotter stars. This implies that classical Be stars have masses ranging from $\sim 2 - 20 M_{\odot}$ (Schmidt-Kaler, 1982).

As previously mentioned, Oe stars are often considered equivalently to Be stars, as they behave very similarly. As Oe stars are typically of late O subtype, these stars can be considered to have masses of $\sim 20 - 40 M_{\odot}$ (Silaj et al., 2014).

In binary systems the observed companions are more commonly late Oe stars (O7 - O9) or early Be stars (B0 - B2) (Raguzova and Popov, 2005; Coe and Kirk, 2015). These spectral types imply that the approximate masses of these stars lie between $9 M_{\odot}$ and $30 M_{\odot}$. However, when they exist in a binary they are undermassive for their spectral type (see Section 1.3.3).

1.1.3 Emission

The observed spectral energy distribution (SED) of a Be star differs from the standard photospheric spectrum of a B-type star due to the presence of the circumstellar disc. The disc both absorbs radiation from the central star and emits radiation that is dependent on the properties of the disc. The relation between these processes and the emergent spectrum is dependent on both the wavelength of the emission and the viewing angle of the Be star. An example is ultraviolet emission, where the light scatters off the disc. Therefore when the Be star is viewed pole-on, the UV emission is enhanced and it is depleted when looking along the length of the disc.

There are three components to the emission of an isolated Be star system: the central Be star, the stellar wind and the circumstellar disc. The central star displays the same emission as a B-type star (see Section 1.1.1) which emits as a black body. One of the brightest Be stars, α Eri, has a luminosity of $\sim 10^{37}$ erg s^{-1} (Carciofi et al., 2008).

In general, the stellar wind of Be stars is similar to a normal B-type star but Be star winds should be stronger during mass outflow events (Grady et al., 1987, 1989). The variation in the strength of the wind is dependent on the rotation speed of the Be star. The stellar wind's X-ray emission in isolated Be star systems is typically in the range $10^{30} - 10^{32}$ erg s^{-1} (Cassinelli et al., 1994; Naze et al., 2011).

The Be star's circumstellar disc is the brightest component of the Be star system in optical and infra-red wavelengths. To what extent is dependent on the size and density of the disc. Two examples of this are the isolated Be star ω CMa with an apparent V-band magnitude that has been observed to vary by ~ 0.5 (Ghoreyshi et al., 2018) and the Be/X-ray binary SXP 5.05 that has an apparent I-band magnitude observed to vary by ~ 0.4 (Coe et al., 2015). Hence, the disc can grow to be at least as bright as the central Be star. This only occurs in certain wavelengths such as the V-band and I-band as the disc mainly emits in the optical and infra-red (Carciofi and Bjorkman, 2008).

A huge amount of work has gone into studying the emission of the disc but this is largely out of the scope of the work in this thesis. An extensive review of Be stars including a comprehensive introduction to the various aspects of Be star emission is included in (Porter and Rivinius, 2003) and Rivinius, Carciofi and Martayan (2013). As the focus of the work in this thesis is the behaviour of the disc, this section will only cover topics involving observables that are related to the dynamics of the disc.

Dynamic behaviour

The emission of Be stars varies on a broad range of timescales from a few minutes to many decades. As mentioned in Section 1.1.1, a Be star can go from emitting a normal B-type spectrum to an excess in a broad range of wavelengths (or vice versa) in a matter of years. This is due to the growth and/or dissipation of the disc. Both the density and size of the disc determine the observed emission (Faes et al., 2013) and hence it can be assumed that the disc is responsible for most of the variabilities observed in Be stars.

A distinctive trait of Be stars is the variation in the line emission, particularly the fluctuations in the ratio between the peaks of the emission line. These are named V/R variations (see Section 1.1.3) due to the relative changes in the violet and red peaks. These variations have periods much longer than the rotation period of the star and are thus ascribed to the circumstellar disc. They are also much longer than the rotation period of the disc's Keplerian motion and therefore must be due to some evolving structure in the disc (see Section 1.1.3).

The shortest period line profile variabilities occur on timescales of between 0.5 and 2 days and are observable in virtually every single Be star system. A single Be star can exhibit multiple of these rapid variabilities with different periods. These are attributed to the Be star itself and arise due to non-radial pulsations (see Section 1.1.4).

V/R variations

A common variability in the emission of Be stars is the relative changes in the redward and blueward peaks in the line profiles, and has been named V/R variations. A number of the important observable properties are outlined by Okazaki (1991) and were updated with more recent findings by Rivinius, Carciofi and Martayan (2013). These are as follows:

1. The periods of V/R variations range from years to decades and are therefore hundreds of times larger than the orbital period of the material in the disc and thousands of times larger than the rotation period of the star.

2. There is no relation between the period of the V/R variations and the spectral type of the central Be star.

3. The length of the V/R period can change from cycle to cycle (Štefl et al., 2009; Ruždjak et al., 2009).

4. The entire line profile shifts redward when the blue peak is stronger and vice versa.

5. In binary systems containing a shell star, V/R variations are sometimes phase locked to the orbital motion (Štefl et al., 2007).

6. Some shell stars exhibit a third peak during the variation of the Hα profile (Štefl et al., 2009).

7. Lags between the V/R variations of different optical emission lines and infrared lines have been observed (Wisniewski et al., 2007)

8. A positive correlation between the V/R variability and the presence of discrete absorption components has been found in studies of UV spectra (Doazan et al., 1987; Telting and Kaper, 1994).

Okazaki (1991) and Papaloizou, Savonije and Henrichs (1992) provided theoretical models to explain these variations that involve a precessing, one-armed density wave. This density wave rotates much slower than the orbit of the material in the disc and was shown to have a period consistent with V/R variations. In the case of binarity, the most popular theory is currently the precession of an eccentric disc (see Section 1.3.5).

1.1.4 The Be phenomenon

The presence of a disc surrounding the Be star is generally accepted but the actual mechanism that gives rise to the outflowing material has been very difficult to determine. Stellar wind is not a large contributor in the ejection of the disc material, because they are typically weak in B-type stars (Prinja, 1989; Krtička, 2014). Another suggested possibility is leverage due to the magnetic field of the Be star but no sufficiently strong magnetic fields were found in a sample of 100 Be stars, by the 2012 survey, "Magnetism in Massive Stars" (MiMeS) (Wade et al., 2012). The most popular theory of the source of the disc-forming mass outflow is the combination of rapid rotation and non-radial pulsations.

Stellar rotation

Be stars are some of the fastest rotating stars (aside from compact objects) in terms of the projected rotational velocity or $v \sin i$ (Townsend et al., 2004). Hence, they are excellent objects for testing theories about fast rotating stars. One such example is testing the difference between the pulsational properties of rapid-rotating stars and non-rotating stars. This provides an insight into the interior structure of rotating stars (Reese et al., 2009; Lee, 2012; Reese et al., 2013).

A star rotating greater than or equal to the critical rotation, is capable of ejecting mass from the surface of the star into a Keplerian orbit. Here, critical rotation is defined as the point where the rotational velocity at the equator is equal to the

Keplerian orbital velocity of a particle at the equator. Despite the fact that Be stars rotate so rapidly, it cannot be the only mechanism responsible for the production of the disc. There are Be stars that have been shown not to rotate close to the critical rotation (McSwain et al., 2008; Meilland et al., 2012) and there are B-type stars that rotate faster than many Be stars and yet do not possess disc line emission (McAlister et al., 2005). Hence, there must be some additional feature of Be stars that provides additional angular momentum to the matter at the equator: this is widely accepted to be non-radial pulsations.

Non-radial pulsations

As mentioned in Section 1.1.3, there are very short period (from 0.5 to 2 days) variabilities in the emission of Be star systems that originate from the Be star itself. However, there has been much debate in the past concerning the source of these variables. It could be due to either rotation or pulsation (Porter and Rivinius, 2003). Rivinius, Baade and Štefl (2003) suggested that the mechanism is a specific kind of pulsations, namely low order, g-mode (or "gravity"-mode) non-radial pulsations (NRPs), with grouped multiperiodicity. The first confirmation of multiperiodicity in the pulsations was made by Walker et al. (2005) whilst observing the Oe star, ζ Oph. However, since the recent advances in astroseismology (Aerts, Christensen-Dalsgaard and Kurtz, 2010), the multiperiodicity of Be stars is often observed.

Pulsations as a contributing mechanism to the Be phenomenon was proposed around 30 years ago by Baade (1988). Despite indications that outbursts and changes in the pulsation behavior of Be stars may be correlated (Bolton, 1982; Penrod, 1986), it has been shown that the amplitude of a single pulsational mode is not sufficient to form a Be star disc (Owocki, 2006). Constructive interference between multiple modes was first observed giving rise to mass ejection events in the Be star system, μ Cen (Rivinius et al., 1998). Work is still continuing into the role of NRP modes in relation to the Be phenomenon but recent work shows that systems have a mass ejection rate controlled by a hierarchy of modes (Baade, 2018).

1.2 Decretion discs

It has become widely accepted that classical Be stars possess a circumstellar disc formed from ejected matter. The rapid rotation and non-radial pulsations (see Section 1.1.4) of the central star create an outwardly diffusing, gaseous disc. There is a large variety of observational behaviour seen in Be stars and models including a decretion disc have managed to explain a number of them. For example, recent work has shown accurate modelling of the lightcurve of ω CMa (Ghoreyshi et al.,

2018). Even more complicated features, such as V/R variations (see Section 1.1.3), can be explained qualitatively using a disc (Okazaki, 1991).

This section will discuss the generally accepted disc model and how it can explain a variety of the observational features of a Be star system. Firstly, the geometry of the disc will be discussed, including the flaring of the disc and its density profile. Secondly, the motion of the material in the disc will be outlined. Following this, the dynamical behaviour of the disc is examined. Finally, the most popular method for modelling the circumstellar discs of Be stars, the Viscous Decretion Disc model, is described.

1.2.1 Geometry

To explain the large dependence of the SED on the inclination of the system and the phenomenon of shell stars, the mass outflow of the Be star must be a flattened disc-like structure. This general picture has been confirmed through optical long baseline interferometry (Quirrenbach et al., 1994). Although this method was able to unequivocally show the existence of a flattened envelope, it can only determine either the thickness or the inclination of the disc. This is because the appearance of the disc is dependent on both these quantities, with no way to disentangle them.

Disc flaring

It is not possible to specify whether the structure surrounding the Be star is a disc or just an oblate envelope without determining its thickness. A few years after the determination of the flattened envelope, Wood et al. (1997) showed that the spectropolarimetric observations of ζ Tau could only be explained by either a thin disc with an opening angle of 2.5° or a thick disc with an opening angle of 52° (opening angle is measured from the equatorial plane of the disc). In the same year, Quirrenbach et al. (1997) combined polarimetry with interferometric techniques, and so determined an upper limit to the disc opening angle of 20° for the same system. Thus, the envelopes of Be stars must be thin discs with small opening angles.

For an isothermal, rotationally supported disc, there is a dependence of the disc height on the radius from the central star. This dependence is only affected by the gas pressure and gravity of the star (Bjorkman, 1997). The scale height of the disc is given by

$$H(r) = \frac{c_{\mathrm{s}}}{v_{\mathrm{orb}}} \frac{r^{3/2}}{R_*^{1/2}}, \tag{1.2}$$

where $v_{\rm orb}$ is the Keplerian orbit velocity of a particle on a circular orbit at the star's equator and R_* is the radius of the star. $c_{\rm s}$ is the isothermal speed of sound on the disc given by

$$c_{\rm s} = \sqrt{\frac{k_{\rm B}T}{\mu m_{\rm H}}}, \tag{1.3}$$

where T is the isothermal electron temperature, μ is the mean molecular weight of the gas. Thus, the height of the disc grows with radius and yields a flaring disc.

Density in the disc

The density profile of the disc has a large effect on the results of any modelling and thus initial attempts to model the disc were limited by the variety of suggested concepts (Gehrz, Hackwell and Jones, 1974; Waters, 1986). Hence, it was helpful to agree upon a satisfactory definition for the density profile of the disc. As mentioned in Section 1.2.1, the most common view of the density of the disc is one supported by the gas pressure in the vertical direction and held in a rotationally stable state by the gravity of the central star. Radially, the density falls off as a power law

$$\rho(r) = \rho_0 \left(\frac{r}{R_*}\right)^{-n}, \tag{1.4}$$

where n is the power law index and ρ_0 is the base gas density, i.e. the density of the circumstellar material at the Be star's surface.

Measurements of the size of a given band's emission region provide information about the bulk properties of the disc material. Both the size of the emission regions and the continuum SED can be modelled using radiative transfer techniques to determine the density of the disc. There have been many attempts to fit the power law of the density profiles of Be star circumstellar discs. Table 1.1 shows the results from seven fits to specific decretion discs. The works by Carciofi et al. (2006, 2007, 2009) use radiative transfer techniques and a fixed power law index to fit the SED, polarization and line profiles. Tycner et al. (2008) and Jones, Sigut and Porter (2008a) modelled and then analysed the interferometry and spectroscopy of the Be star systems.

The value of n was more broadly investigated by Silaj et al. (2010) through the fitting of the Hα profiles of 56 Be stars. They found that the power law index lies in the range $1.5 \leq n \leq 4$ but provides the best fits at a value of $n = 3.5$. Touhami, Gies and Schaefer (2011) were able to reproduce statistical properties of the colour

Table 1.1: Examples of the base gas density, ρ_0, and power lax index, n for fits to the density profile of Be star discs.

System	ρ_0	n	Reference
δ Sco	4.5×10^{-10}	3.5 (fixed)	Carciofi et al. (2006)
α Eri	7×10^{-13}	3.5 (fixed)	Carciofi et al. (2007)
ζ Tau	5.6×10^{-11}	3.5 (fixed)	Carciofi et al. (2009)
χ Oph	2×10^{-11}	2.5	Tycner et al. (2008)
κ Dra	2×10^{-11}	2.5	Jones, Sigut and Porter (2008a)
β Psc	1.5×10^{-10}	4.2	Jones, Sigut and Porter (2008a)
ν Cyg	3×10^{-12}	2.1	Jones, Sigut and Porter (2008a)

excesses of 130 Be stars by using a simple radiative transfer model. They added a Gaussian dependence on the height of the disc as follows

$$\rho(r, z) = \rho_0 \left(\frac{r}{R_*} \right)^{-n} \exp \left[-\frac{1}{2} \left(\frac{z}{H(r)} \right)^2 \right], \tag{1.5}$$

where z is the vertical coordinate and $H(r)$ is the scale height that is described by Equation 1.2.

Size of the disc

It is difficult to determine the physical size of the Be star's disc through observations to the point where only a few studies have made an attempt to create a definition for this quantity (Rivinius, Carciofi and Martayan, 2013). A given line or band is only emitted by a certain region of the disc (Faes et al., 2013) and hence any observation can only estimate the size of a portion of the circumstellar envelope. It is sometimes possible for an emitting area to span the entirety of the disc when it is tidally truncated in a binary.

Predicting the size of any particular Be star's disc is made even more difficult due to its dynamic nature. This would require a good understanding of the mechanism that forms the disc, which is still not fully understood (see Section 1.1.4). However, these discs have been shown to reach sizes of hundreds of stellar radii (Dougherty and Taylor, 1992).

1.2.2 Disc rotation

The proposal of a circumstellar disc orbiting Be stars provided an explanation for the observed double peaked line emission (see Figure 1.2). The motion of the disc material towards and away from the observer Doppler shifts the observed wavelength. This mechanism also imparts a dependence on the viewing angle of the

system. However, it is important to understand the specific motion of the gas because it provides information about the nature of the formation.

Initially, three cases for the azimuthal velocity of the disc, v_ϕ, were proposed

1. $v_\phi \propto r^{-1}$: stellar wind from a rotating star, where the dominant force is the radial radiation pressure.
2. $v_\phi \propto r^{-1/2}$: a disc with standard Keplerian rotation for particles orbiting a body due to gravitational forces.
3. $v_\phi \propto r$: plasma trapped by strong magnetic fields and corotating with the star.

Case 3 is immediately ruled out by the shape of the emission line profiles. For the line shapes observed in Be star systems, it is required that the velocity decreases with radius. Hummel and Vrancken (2000) showed more work is required to eliminate either Case 1 or 2 because the emergent line shapes can be similar.

Theoretical models created to explain V/R variations (Okazaki, 1991; Papaloizou, Savonije and Henrichs, 1992) suggested the existence of a precessing, one-armed density wave. It is shown that non-Keplerian disc motion would cause these oscillation modes to be unstable. Eventually, spectrally resolved interferometry and spectroastrometry of emission lines finally confirmed the Keplerian nature of the disc (Meilland et al., 2007b; Delaa et al., 2011; Kraus et al., 2012; Wheelwright et al., 2012).

It should be noted that although the disc material may often be expected to flow on circular Keplerian orbits, there are cases where the motion must be non-circular orbits. One such case is in discs exhibiting V/R variations, where there is always a non-zero velocity component projected along the observer's line of sight. Another example is where the binary companion's orbit is misaligned to the plane of the disc (see Section 1.3.5).

1.2.3 Dynamics of the disc

Possibly the most difficult thing to understand about Be star systems, is the growth and decay of the disc which is currently impossible to predict. Some systems have been observed to remain stable for very long times, such as ζ Tau. Others, e.g. π Aqr, exhibit a gradual disappearance of observational features due to the dissipation of the disc (Wisniewski et al., 2010; Draper et al., 2011). ω Ori is an example of a Be star developing a circumstellar disc from scratch (Guinan and Hayes, 1984; Sonneborn et al., 1988). All these cases can only be explained through changes in the rate of the mass ejection from the Be star's surface. Clearly, it can only increase, decrease and stay approximately steady. A number of systems exhibit

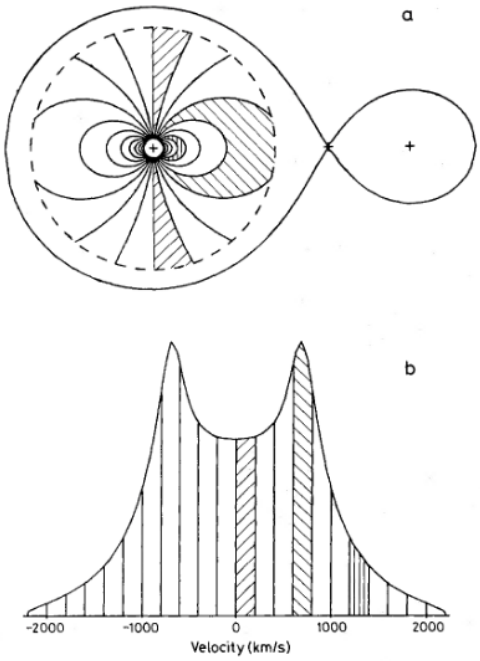

Figure 1.2: Figure 1 from Horne and Marsh (1986). (a) A Keplerian accretion disc in a binary shown from a top-down view. (b) The velocity profile of an emission line profile from the disc. Emission in the shaded areas of the line profile correspond to the similarly shaded areas of the Keplerian disc.

both irregular and regular variability such as ω CMa, which displays the latter nature in the form of quasi-cyclic variability (Štefl et al., 2003). It has been shown recently that the variabilities in the light curve are well modelled by different regimes of high and low mass ejection (Ghoreyshi et al., 2018).

When monitored during dissipation, the high velocity components of the line profile begin to disappear. This was suggested to be due to a depleted inner region of the disc (Rivinius et al., 2001). This occurs because the Be star continues to accrete infalling material when the mass ejection ceases. This has been supported by viscous disc models Haubois et al. (2012). In fact, viscous disc models (see Section 1.2.4) have been able to explore many dynamical aspects of the discs of Be stars, such as expected mass ejection rates during disc growth and disc dissipation (Rímulo et al., 2018).

1.2.4 Viscous Decretion Disc model

A consensus has been reached that the viscous decretion disc (VDD) model, first suggested by Lee et al. (1991) and subsequently developed by Bjorkman (1997), Okazaki (2001) and others, is the best candidate to explain the observed properties of Be discs (Carciofi, 2011; McGill, Sigut and Jones, 2011). The decretion disc of a Be star has been shown to be Keplerian from spectro-interferometry (Meilland et al., 2007a; Kraus et al., 2012) and hence, the developed hydrodynamical VDD

models conform to this criterion (Okazaki, 2001; Jones, Sigut and Porter, 2008a). More recent results from simulations using this model are currently able to explain most of the observable properties of Be stars (Klement et al, 2015).

The basic hydrodynamics of the VDD model are identical to viscous accretion disc models for young stellar objects (Shakura and Sunyaev, 1973; Pringle, 1981) (see Section 1.4.2) aside from one key factor - the flow of matter in the disc can go both outwards and inwards. Keplerian disc material is introduced to the simulation just outside the Be star's surface. When material is supplied to the disc, the new matter increases the total angular momentum of the disc and hence, the disc can grow in size. On the other hand, when no material is supplied to the disc the model simplifies to the case of an accretion disc (provided there is already an existing disc). A lot of the initial work with the VDD model assumed a constant rate of mass injection and an isothermal disc (Bjorkman, 1997; Porter, 1999; Okazaki, 2001). These models were able to reproduce the majority of the key theoretical features expected of Be star discs in a steady state.

Radiative transfer techniques were then applied to the resultant density profiles determined from simulated steady state discs to investigate the behaviour of the temperature (Carciofi et al., 2006; Sigut and Jones, 2007; Carciofi and Bjorkman, 2008; McGill, Sigut and Jones, 2011). Figure 1.3 shows two figures from Carciofi et al. (2006). The first is an illustration of the temperature within the disc, showing a cool, inner region and a hot, outer region. This is expected given the emission lines that arise from the disc. The second part of Figure 1.3 shows how the temperature varies with radius for four models (Model 1 has the lowest base gas density and Model 4 has the highest). The inner disc is shown to be non-isothermal: the temperature initially falls rapidly and reaches a minimum that is dependent on the density of the model. The temperature rises to $\sim 60\%$ of the effective temperature of the star.

As discussed in Sections 1.1.3 and 1.2.3, the circumstellar discs of Be stars are dynamic in nature and so the next logical step was to use the VDD model to simulate the evolution of the disc over time. Haubois et al. (2012) studied the growth and dissipation of the disc using hydrodynamical simulations. When the disc is fed at a constant rate, the disc grows and asymptotically approaches the theoretically determined density profile. But when the simulation begins with a pre-existing disc and the mass ejection rate is reduced to zero, the disc assumes two separate behaviours. The inner part of the disc is accreted back onto the Be star and the outer region continues to diffuse outward. Haubois et al. (2012) name the separation between the two regions the "stagnation point" which moves away from the star with time. The radial velocity at the stagnation point is zero. It was noted that the viscosity parameter (see Section 1.4.2), α, affects the time it takes for the disc to evolve. A growing disc with $\alpha = 1$ grows ten times faster than one with

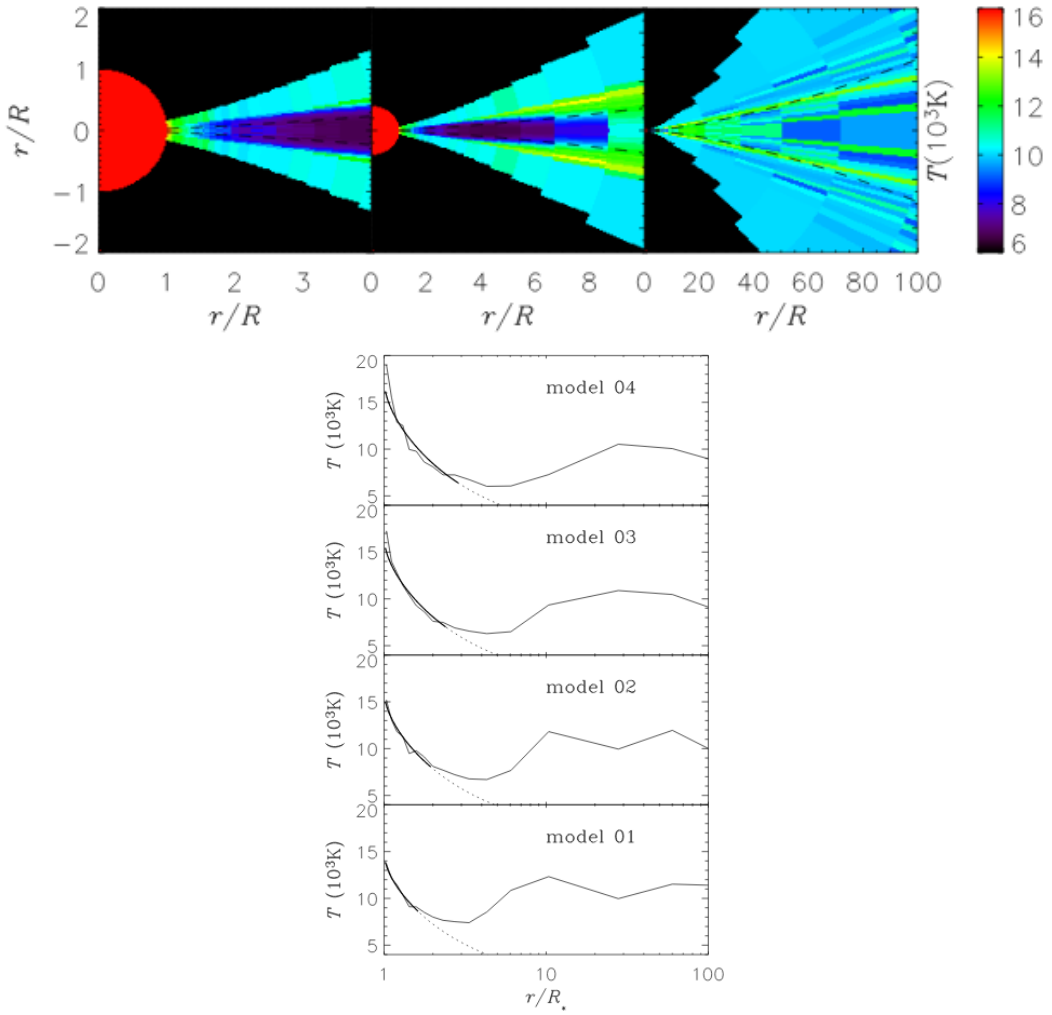

Figure 1.3: Figure 6 and 7 from Carciofi et al. (2006). Top: An illustration of the temperature structure for model 2 at three radial scales. Bottom: The radial dependence of the equatorial temperature for models 1, 2, 3, and 4 (increasing base gas density, respectively). The thick curve is a fit to a flat blackbody reprocessing disc (Adams et al., 1987). Base gas densities for the models are as follows (in units of 10^{-11} g cm^{-3}): 1: 1.66, 2: 4.15, 3: 8.39, 4: 16.6. Density at each point in the disc is calculated using a similar expression to Equation 1.5.

$\alpha = 0.1$.

Only recently have VDD models and radiative transfer methods been combined because they are both computationally expensive. Rímulo et al. (2018) used the 3D NLTE radiative transfer code, HDUST (Carciofi et al., 2006; Carciofi and Bjorkman, 2008), and the 1D thin-disc code SINGLEBE (Okazaki, 2007) to explore the parameter space of viscosity and mass ejection for a sample of 54 observable Be stars. It was found that the typical mass and angular momentum loss rates associated with the disc events are of the order of $\sim 10^{-10}$ $\mathrm{M_\odot\,yr^{-1}}$ and $\sim 5 \times 10^{36}$ $\mathrm{g\,cm^2\,s^{-2}}$, respectively. It was also found that, for the entire sample, the median values for the viscosity parameter during disc growth and dissipation are $\alpha_{\mathrm{growth}} = 0.63$ and $\alpha_{\mathrm{diss}} = 0.26$, respectively.

Ghoreyshi et al. (2018) convincingly modelled the light curve of the isolated Be star system, ω CMa, using the same two codes. ω CMa is one of the brightest Be stars that can be observed ($m_{\mathrm{V}} \approx 3.6$ to 4.2) and so has often been a target for observations. The viscosity parameter, mass ejection and angular momentum loss rates are all determined through analysis of the simulation data. It is shown that the disc's viscosity and the Be star's mass ejection must vary with time to reproduce the light curve. This is in agreement with the predicted dynamic nature of the disc.

A three-dimensional SPH code (Okazaki et al., 2002) was used in conjunction with HDUST by Panoglou et al. (2018). Convincing evidence is provided for the phase-locked variations in the emission lines from the disc. As one of the earliest attempts to combine a three-dimensional VDD model and three-dimensional radiative transfer, this is an indicator of the power of combining these two methods.

1.2.5 Horne and Marsh line profiles

Be stars are well known for the Hα emission produced by their discs (Rivinius, Carciofi and Martayan, 2013). These profiles are one of the most direct methods of observing the behaviour of the circumstellar disc. Hα profiles provide information about the inclination of the system via the prominence of a double-peaked structure that arises due to Doppler effects. The relative size of the disc can be inferred from the equivalent width of the Hα profile (Hanuschik, 1989) or the separation of the peaks (Huang, 1972).

Horne and Marsh (1986) applied a simplification of radiative transfer techniques to accretion discs to formulate line emission shapes for optically thin and optically thick cases (also see Marsh (1987); Horne (1995) for further details). This method has since been applied to Be star decretion discs by Okazaki (1996) and Hummel and Vrancken (2000). The method is unreliable for extreme inclination angles ($\geq 80°$).

Horne and Marsh (1986) suggested a basic expression for the broadening of the line emission by Doppler shifts. These Doppler shifts are due to the orbital motion of the material in the disc along the line of sight. This shear broadening is expressed as

$$V_{shear} = -\frac{H}{2R} V_K \sin i \tan i \sin \phi \cos \phi, \tag{1.6}$$

where i is the inclination of the disc, ϕ is the azimuthal angle in the disc plane, H is the disc height, R is the radius and V_K is the local value of the Keplerian velocity. The line optical depth is given by

$$\tau_\nu = \frac{W(R)}{\cos i} \frac{\lambda_0}{\sqrt{2\pi}\Delta V} \exp\left[-\frac{1}{2}\left(\frac{V - V_D(0)}{\Delta V}\right)^2\right], \tag{1.7}$$

where λ_0 is the rest wavelength and ΔV is given by

$$\Delta V = \sqrt{\Delta V_{th}^2 + V_{shear}^2} \tag{1.8}$$

where ΔV_{th} is the thermal broadening. $W(R)$ is given by

$$W(R) = \frac{\pi e^2}{mc} f \Sigma(R), \tag{1.9}$$

where f is the absorption oscillator strength and $\Sigma(R)$ is the surface density. In the previously mentioned treatments of shear broadening, the disc density is provided by a theoretical function and in the case of the Be star, Equation 1.5 is used as a description of the density of the disc. Okazaki (1996) assumes a (continuum-subtracted) line intensity emerging from the emission layer of a Be star's circumstellar disc that is given by

$$I_\nu = S(1 - e^{-\tau_\nu}), \tag{1.10}$$

where S is the source term, i.e. the function that describes the emission at every point in the disc.

1.3 Be/X-ray binaries

Be/X-ray binaries are the largest population of observable High Mass X-ray Binaries (HMXBs) (Rappaport and van de Heuvel, 1982; van de Heuvel and Rappaport, 1987; Coleiro et al., 2013). The varying size of the disc, coupled with the interaction of a compact object leads to a variety of observable effects. Some of these, such as giant outbursts (see Section 1.3.5) and superorbital modulation of X-ray lightcurves, are not well understood. Superorbital modulation is when the X-ray flux of the system varies on periods longer than one orbit and hence requires physical mechanisms in addition to accretion. Comprehending these phenomena can lead to a better understanding of the extreme physics of neutron stars and black holes (see Reig (2011) for a comprehensive review).

Now that the features of the central star have been covered in Section 1.1, the features that arise due to binarity are discussed in this section. Firstly, typical properties of Be/X-ray systems are discussed. Secondly, a definition of X-ray binaries is provided and their key features are outlined. Then, the possible compact objects that can exist in a binary with a Be star are identified. Finally, the interactions between the binary companion and the disc are examined, including the tidal truncation and misaligned orbits. This section is particularly relevant to Chapter 4, where simulations are used to investigate the general properties of Be/X-ray binaries.

1.3.1 Be/X-ray binary properties

The orbits of Be/X-ray binaries are generally wide, i.e. from ten to hundreds of days. However, there are systems that have much larger orbital periods such as PSR J2032+4127 that has a binary period of ~ 50 years (Coe et al., 2019). Observed Be/X-ray binaries are also largely eccentric ($0.1 \leq e \leq 0.9$) (Okazaki and Negueruela, 2001) but the majority of system with known eccentricities lie between $0 < e \leq 0.6$ (Brown et al., 2018).

The optical and infrared flux of a Be/X-ray binary is completely dominated by the Be star companion (Reig, 2011). Given that the two main observational characteristics of Be stars are the emission lines (such as Hα) and an excess of IR emission (see Section 1.1.3), observations of these wavelengths allows for the understanding of the Be star alone. The X-ray emission provides information on the surroundings of the compact object and thus it is possible for both binary components to be considered simultaneously. The only effect on the optical emission that occurs from binarity is V/R variations that are driven by the compact object (see Section 1.1.3).

Due to the nature of accretion in Be/X-ray binaries (i.e. from the circumstellar disc

Table 1.2: Typical values for Be/X-ray binary properties.

Orbital period	10 days - 1 yr
Eccentricity	$0.1 \leq e \leq 0.6$
X-ray luminosity	$10^{34} - 10^{38}$ erg s^{-1}
Hα Equivalent Width	≥ -50 Å
Base gas density	$10^{-12} - 10^{-9}$ g cm^{-3}
Size of Be star's disc	$< 200 R_{\odot}$
Neutron star spin period	1 - 1000 s

of the Be star), the X-ray flux of these systems is heavily dependent on the orbit of the compact object. Typically observed Be/X-ray binaries have an X-ray flux that increases by a large factor (> 10) at one or more points during the orbit of the compact object (see Section 1.4 for more details on such outbursts) (Okazaki and Negueruela, 2001). This is because the majority of observed Be/X-ray binaries are eccentric and the compact object passes close to the disc at periastron. There are some systems that have been observed to emit a low X-ray luminosity persistently ($L_{\mathrm{X}} \sim 10^{34}$ erg s^{-1}) due to the compact object spending it's time in close proximity to the disc for the entire orbit (Reig and Roche, 1999). Persistent sources are known to contain neutron stars with much slower spin periods (> 200s) than the transient sources (La Palombara et al., 2009).

1.3.2 X-ray binaries

X-ray astronomy is a field that has taken great strides since it became possible to use telescopes outside the Earth's atmosphere. Unlike larger systems containing compact objects (such as Active Galactic Nuclei) there are many X-ray binaries (XRBs) that are close to Earth, i.e. in the Milky Way. As the smallest systems containing compact objects, they also vary on the shortest timescales, possessing orbits with periods that can be shorter than a day. This allows for observations of the entirety of the orbital dynamics.

XRBs are systems that contain a compact object (a neutron star, black hole or white dwarf) that is accreting matter from a gravitationally bound star. The gravitational potential energy of the infalling matter is converted into heat and hence the inner parts of the accreting regions around the compact objects are extremely hot. Some of this thermal energy is converted into X-ray photons. These X-rays provide the only method of probing the extreme physics close to black holes and neutrons stars.

It can often be difficult to determine the nature of the compact object in an XRB. The compact object itself is often not bright enough (aside from in X-ray emission) to be seen when close to another star. It can be possible to determine the mass of the object by fitting an orbital model to the dynamics of the system. As neutron

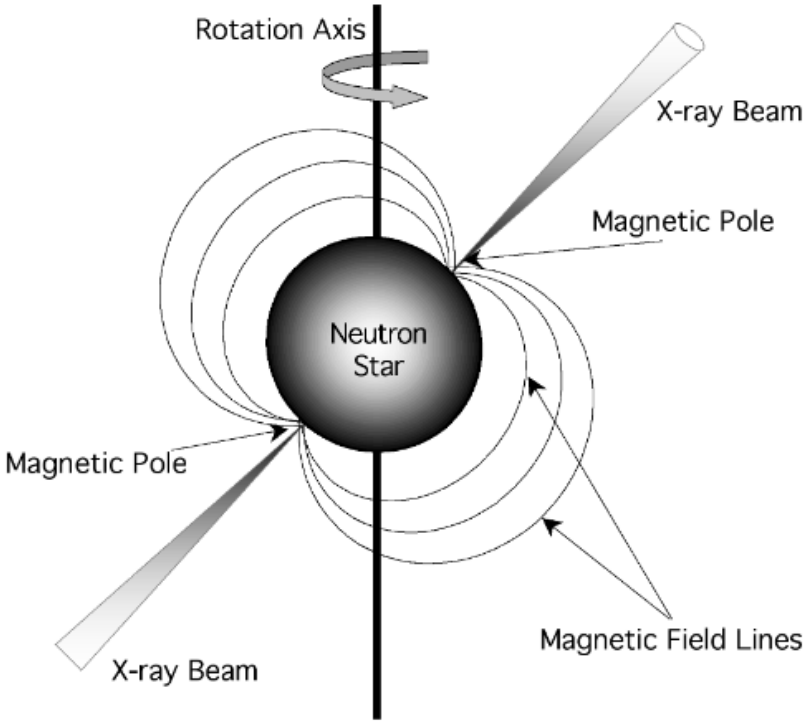

Figure 1.4: Figure 1 from Sheikh et al. (2006). A diagram of a pulsar i.e. a neutron star with its rotation axis misaligned with respect to its magnetic field axis.

stars, black holes and white dwarfs are all expected to be in different mass ranges, this can determine the compact object's nature. Another method of identification is the existence of pulsations, which only occur in neutron star systems. The axis of rotation of a neutron star is often misaligned to its magnetic axis. Hence, when matter falls along the magnetic field lines, the resultant beam of emission will rotate about the spin axis. This leads to a time-dependent variation in the emission that we observe: that has a period dependent on the spin of the neutron star (see Figure 1.4).

There are multiple mechanisms that lead to the accretion of matter onto the compact object and these separate XRBs into two populations. Low-Mass X-ray Binaries (LMXBs) are systems that accrete via Roche lobe overflow as the stellar wind of the donor stars are insufficient to power a bright X-ray source. Mass transfer via Roche lobe overflow occurs at rates of $\sim 10^{-11} - 10^{-7} M_{\odot}\mathrm{yr}^{-1}$ (Iben, Tutukov and Fedorova, 1997). In HMXBs, the companion star has far more substantial stellar winds or other methods of mass loss that remove between $10^{-10} - 10^{-6} M_{\odot}\mathrm{yr}^{-1}$ (Kudritzki and Puls, 2000). A nearby black hole, neutron star or white dwarf will capture a large enough fraction of this to produce X-ray emission (typically $\leq 10^{38}$ erg s^{-1}) (Negueruela, 2010). In the case of HMXBs, the donor star is a OB star. These stars can be roughly ten to a hundred times more massive than the Sun.

1.3.3 Evolution of X-ray binaries

It is pertinent to first discuss the evolution of isolated stars before binary evolution because it determines key steps in the evolution of binary star systems. A star's evolution is driven by the fusion of materials inside it, where one of the products of the fusion is radiation. The radiation causes the gas to contract that, in turn, heats the gas due to the release of gravitational potential energy. A star will undergo fusion until there is insufficient fuel to balance the gravitational forces. At this point, it will become a compact object (a white dwarf, neutron star or black hole). The nature of the compact object that a star will evolve into is dependent on its initial mass. For a more complete review of the evolution of single stars, see Cox and Giuli (1968) and Kippenhahn and Weigert (1990).

White dwarfs

White dwarfs are formed from stars with a mass of $M < 10M_{\odot}$, they are roughly the size of the Earth and have a mass similar to the Sun. The collapse of white dwarfs is prevented by the electron degeneracy pressure of the internal matter - quantum mechanical pressures become important at high densities (because of the mechanism described by the Pauli exclusion principle) (Fontaine, Brassard and Bergeron, 2001). This pressure is actually only capable of stabilising the white dwarf up to the Chandrasekhar limit when it will then collapse into a neutron star through a Type Ia supernova (Mazzali et al., 2007) (see Section 1.3.3). This can only happen when the white dwarf accretes matter from some other source, i.e. when it is in a binary. A Type Ia supernova occurs when a white dwarf raises its core temperature enough to begin carbon fusion. Do to the large amount of carbon this creates a disruptive runaway fusion. However, the dominant mechanism for the production of Type Ia still remains unclear (Piro, Thompson and Kochanek, 2014).

Cataclysmic Variable (CV) is the name given to a particular kind of binary star system that includes an accreting white dwarf (Hameury and Lasota, 2002). When the density and temperature of the accreted hydrogen reaches a certain threshold, a runaway fusion reaction occurs which rapidly converts the layer into helium. This "nova" increases the brightness of the system considerably.

Neutron stars

Neutron stars are one evolutionary end-point of high mass stars ($M > 10M_{\odot}$) and they have a radius and mass of $R_{\rm NS} \sim 10km$ and $M_{\rm NS} \geq 1.4M_{\odot}$ (Özel and Freire, 2016). Similar to white dwarfs, the collapsing forces are balanced by a quantum mechanical degeneracy pressure, but in this case by neutrons, not electrons. The higher overall mass of the initial star means that the electron degeneracy pressure is

not sufficient to resist collapse and the electrons and protons in the matter get squeezed together to form neutrons and neutrinos, with the neutrinos escaping the star. Neutron stars are known for their magnetic fields and spin - many neutron stars are even classified through the means of pulsating emission. X-ray pulsars accrete matter along the magnetic field lines and the resultant beam of emission will rotate about the spin axis, giving rise to a precisely periodic variation in brightness with time. These pulsations vary from 1 ms to 15 s (Manchester, 2017). Although this is often a good method to determine that the nature of a compact object is a neutron star, systems with long pulse periods could possibly be magnetic CVs.

Black holes

A black hole is the result of a star, neutron star or white dwarf no longer having sufficient pressure forces to balance gravitational forces (Carroll, 2004). For the cases of neutron stars, it requires that they accrete matter over time. When a star collapses further, the entirety of the mass forms a central singularity. Black holes therefore do not have a physical radius like any other star, but a radius at which the gravitational forces are so extreme that even light cannot escape, called the Schwarzschild radius (Schwarzschild, 1916). This radius is given by

$$r_{\mathrm{S}} = \frac{2GM}{c^2}, \tag{1.11}$$

where M is the mass of the black hole. The mass of a black hole quite possibly has no limits with supermassive black holes lying at the centre of galaxies with dynamically measured masses of up to billions of solar masses.

Be/X-ray binary compact object candidates

It is theoretically possible for the compact object companion in a Be/X-ray binary to be a black hole, neutron star or a white dwarf. There are systems where a black hole or white dwarf is a candidate but the vast majority of Be/X-ray binaries have been confirmed to contain a neutron star. Binary evolution models suggest a small number of Be/black hole (Be/BH) binaries (Belczynski and Ziolkowski, 2009; Ziolkowski and Belczynski, 2011) (~ 2 in total) should exist but there should be a large population of white dwarfs ($\sim 70\%$) (Raguzova, 2001). However, there have only been a handful of Be/white dwarf systems detected (Sturm et al., 2012; Li et al., 2012) and a single confirmed Be binary with a black hole companion (Casares et al., 2014). The single confirmed Be/BH binary, MWC 656, will be discussed further in Chapter 6 along with comparisons between black holes and neutron stars as binary partners.

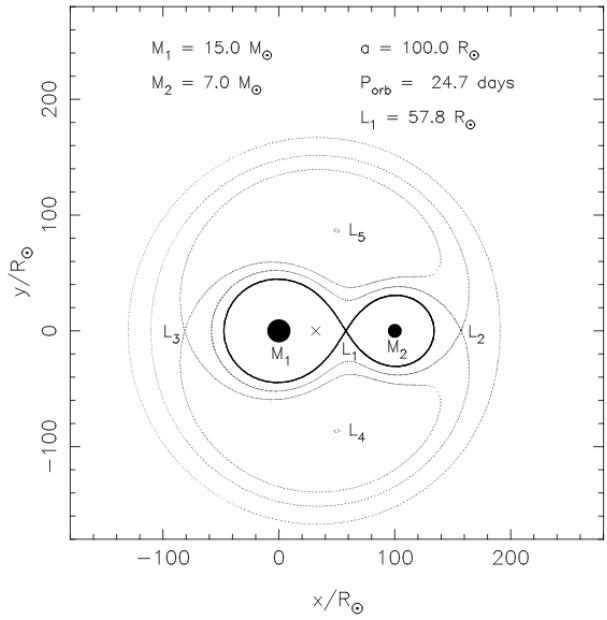

Figure 1.5: Figure 16.9 from Tauris and van den Heuvel (2006). A cross-section in the equatorial plane of the critical equipotential surfaces in a binary. The thick curve crossing through L_1 is the Roche-lobe.

Roche Lobe overflow

The two stars in the binary differ from isolated systems because during their evolution as a pair, mass will be transferred between the two. The mass transfer between the two stars occurs through Roche Lobe Overflow (RLO). The gravitational forces of the two stars create a number of equipotential surfaces (van de Heuvel, 1994) which is demonstrated in Figure 1.5. A star that expands during its evolution can grow to fill the "pear-shaped" Roche Lobe illustrated by the thick line (or the surface, L_1). Any matter leaving this surface will fall onto the other star in the binary system.

When the donor in a binary star system grows during its evolution, it fills its Roche Lobe and matter falls onto the accretor star. RLO continues until the hydrogen-rich envelope of the donor star has been stripped as it no longer fills its Roche Lobe. A star that has only lost its hydrogen envelope and retains its helium envelope is called a "helium star". If a star also has its helium envelope stripped then it is referred to as a "CO star".

Studies from more than 30 years ago (Conti, 1978; Rappaport, Verbunt and Joss, 1983) suggested that the OB supergiants in HMXBs are too luminous for their mass. This is because when an OB star transfers mass via Roche Lobe overflow, the outer layer of the star is peeled off. However, the luminosity of the star is determined by its core and not the mantle, and hence the donor star in a Be/X-ray binary will be undermassive for its observed spectral type (Kaper, 2001). This is

the case for SXP 5.05, the system discussed in Chapter 5. Table 1.3 gives a few examples of HMXBs that have stars that are undermassive for their spectral type. The difference between the expected and observed mass varies for each individual system and does not even seem to be related to the spectral type.

Table 1.3: Examples of HMXB systems that contain a star that is undermassive for its spectral type.

System	Spectral type	Expected mass[1] ($M_\odot$)	Binary mass ($M_\odot$)
SXP 5.05	B0.2 V	16	13 [2]
4U1538-52	B0 Iab	17.5	16.4 [3]
LMC X-4	O7 III-IV	~ 35	15.8 [3]
Cen X-3	O6.5 II-III	~ 41	18.4 [3]

[1] Values for expected mass taken from Silaj et al. (2014), [2] Coe and Kirk (2015), [3] van Kerkwijk, van Paradijs and Zuiderwijk (1995).

However, the response of the donor star to its mass loss has important implications for the evolution of the binary. Donor stars with radiative envelopes (where the primary method of heat transport is radiation) will usually shrink or remain constant in size (Tauris and Savonije, 1999). When the envelope is convective, the star expands instead due to the greater than adiabatic temperature gradient. In some systems, the orbit shrinks fast enough to allow the growing envelope of the donor star to encompass both stars.

Common envelope

The Common Envelope (CE) phase leads to a drag-force that is exerted on the accretor companion in the binary system. This drag arises from the motion of the companion star through the expanded envelope of the donor star, which causes the binary separation to decrease. The loss of orbital angular momentum by the binary often causes the common envelope to be ejected. Reviews on common envelopes are given by Iben and Livio (1993) and Taam and Sandquist (2000).

Supernova explosions

Both RLO and a CE phase can strip the hydrogen envelope of the donor star and possibly its helium envelope. If the star is then massive enough, the star will collapse and then explode. This explosion is called a supernova. For a helium star to collapse into a neutron star, it's mass must be above $2.8M_\odot$ (or a mass of greater than $\sim 10M_\odot$). If the helium star's mass is less than $2.8M_\odot$, the star contracts and forms a white dwarf. It can also collapse into a black hole if the mass is greater than $\sim 8M_\odot$ (Kaper and van der Meer, 2007). Due to the virial theorem, the orbit

of the system will be disrupted if more than half of the binary mass is ejected during this process (Blaauw, 1961).

A supernova occurs because the gravitational collapse of the star releases a large amount of energy that causes the explosion (Heger et al., 2003). This can also be caused by a white dwarf in a binary system that accretes material, increasing its core temperature until runaway nuclear fusion is triggered (known as a Type Ia supernova). Supernovae are classified according to their observed light curves and the absorption lines that appear in their spectra (Cappellaro and Turatto, 2001). The most general grouping, supernovae with spectra that exhibit Balmer emission lines, are Type II and those that do not are Type I.

The supernova's explosion provides a kick to the newly formed compact object that determines the orbit of the new binary system (Lai, Wang and Han, 2006). This implies some asymmetry in the supernova process but the exact mechanism responsible for this has not been fully determined. Suggestions include large-scale convection above the core (Fryer, 2004) and a post-natal electromagnetic boost (Janka et al., 2005). Such an asymmetric supernova can cause a Be star's disc to be misaligned with respect to the orbital plane (see Section 1.3.5).

Future evolution

As shown in Figure 1.6, a Be/X-ray binary will continue to evolve through the steps described above but with the unexploded star as the new donor. The Be star will expand to encompass the compact object in a CE phase and then after a second supernova, the system will end up as a binary neutron star system.

1.3.4 Tidal interactions

As described in Section 1.2.1, the circumstellar disc of the Be star can grow to hundreds of stellar radii. This lies far outside the neutron star's orbit in most observed Be/X-ray binaries (most Be/X-ray binaries have an orbital period of less than 150 days and hence a semi-major axis of $a < 50$ stellar radii) . The proximity of an orbiting compact object to the decretion disc gives rise to a wide variety of observable effects. Figure 1.7 shows a schematic diagram of a Be/X-ray binary where the neutron star's orbit passes directly through the Be star's disc.

One of these observable effects is V/R variations induced by the binary partner, as mentioned briefly in Section 1.1.3. This phase-locked variability has been seen in a few Be/X-ray binary systems, including π Aqr (Pollmann, 2012). V/R variations arising due to the orbital motion can be suppressed by the inherent dynamics of the disc, such as any strong V/R variations already present in the disc.

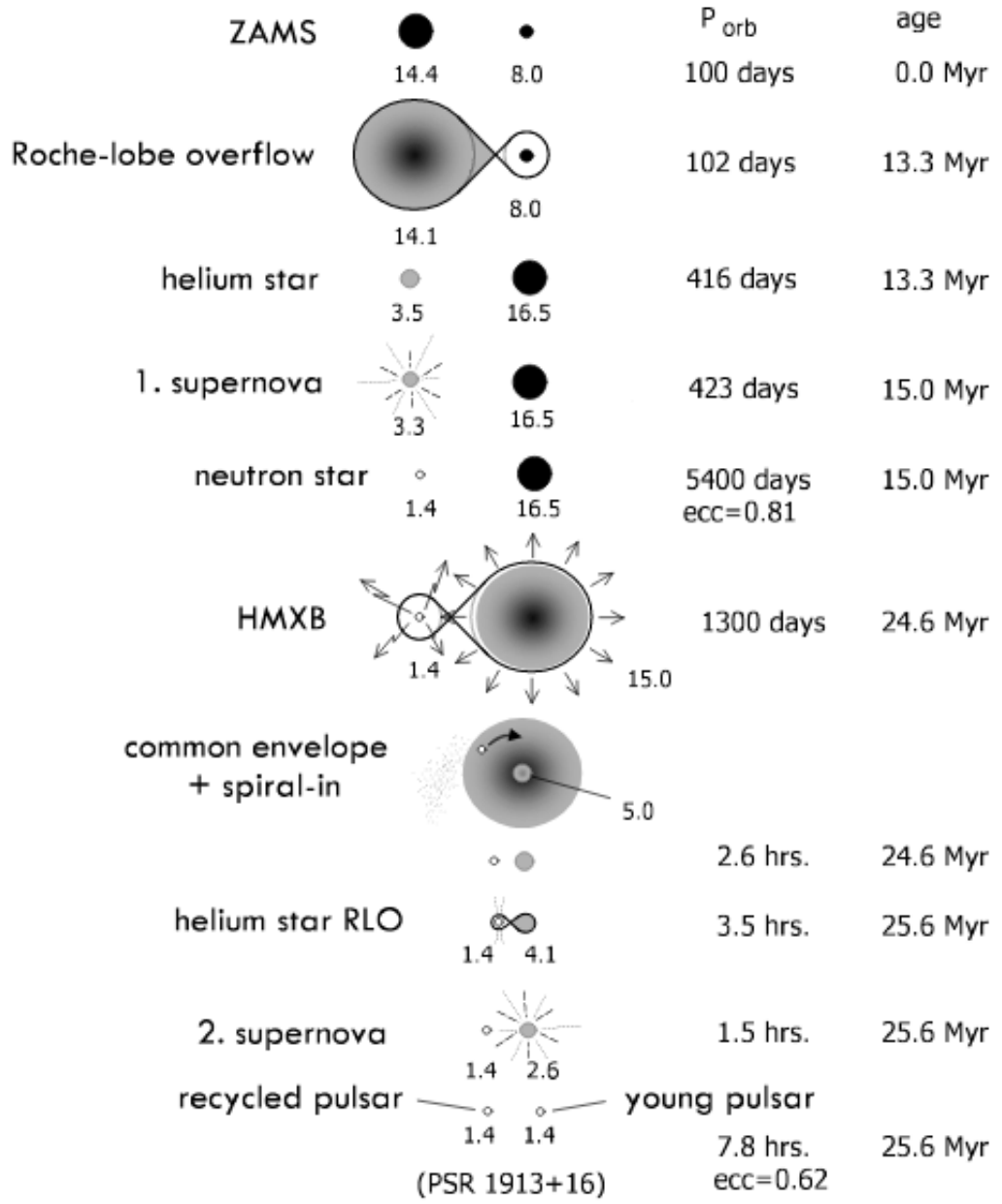

Figure 1.6: Figure 16.15 from Tauris and van den Heuvel (2006). Cartoon depicting the formation of a Be-star/HMXB and then evolving into a double neutron star system. Such a binary will experience two supernova explosions.

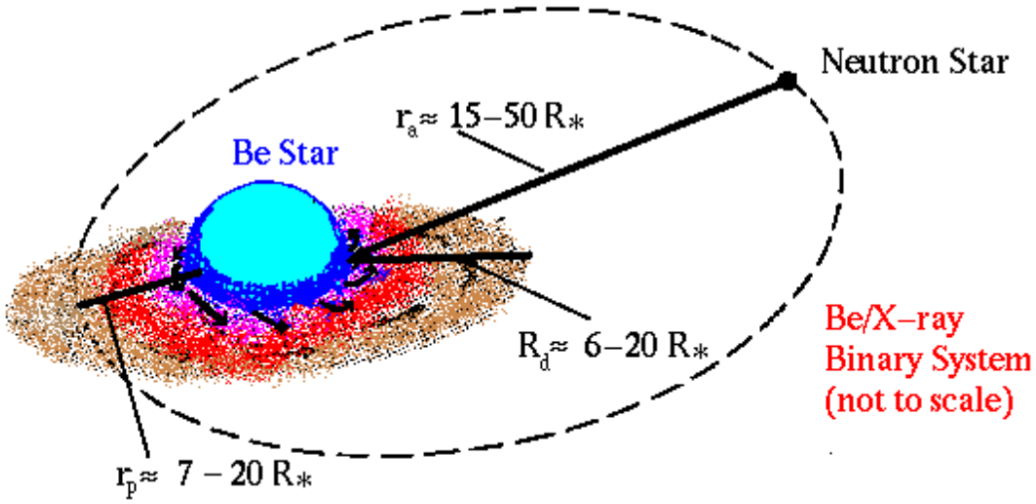

Figure 1.7: An adapted version of Figure 1 from van de Heuvel (2004) taken from http://skinakas.physics.uoc.gr/en/research/xray_binaries.html. Diagram of a Be/X-ray binary containing a neutron star with a descriptions of the typical scales involved.

Tidal truncation

The orbit of the compact object has not only been shown to induce variability in the disc but also to curtail the disc's size. Tidal truncation was first detailed by Okazaki et al. (2002) when modelling Be/NS binaries using a VDD model. However, the results apply to any binary system containing a Be star. This study shows that the truncation radius is at the point where the tidal torque balances the viscous torque. Hence, this radius depends on the properties of the disc and binary companion. More recently it has been shown that the tidal truncation is heavily dependent on the mass of the compact object companion (Brown et al., 2018) (see Chapter 6).

The tidal forces of the compact object have been shown to change the density of the disc. The density inside the truncation radius becomes larger than would be the case for the exact same Be star without a compact object. The density outside of the truncation radius drops off faster than the power law seen in the rest of the disc. Figure 1.8 illustrates this effect. The panel on the left shows the gradual build up of the disc over time and it is clear that there is a radius where the density drops off much more rapidly. The right panel shows three disc properties at equilibrium. The density profile (solid line) is the same as the final curve in the left panel. The dashed line shows the azimuthal velocity normalised by the critical velocity of the Be star, v_ϕ. The profile of v_ϕ behaves identically to the same quantity for an isolated Be star's disc up until a radius of $r \sim 0.7a$. This is to say that the curve is proportional to $r^{-1/2}$.

Tidal truncation is more complex when the orbit is not circular; in this case the interaction with the disc becomes a function of orbital phase. The disc is allowed to

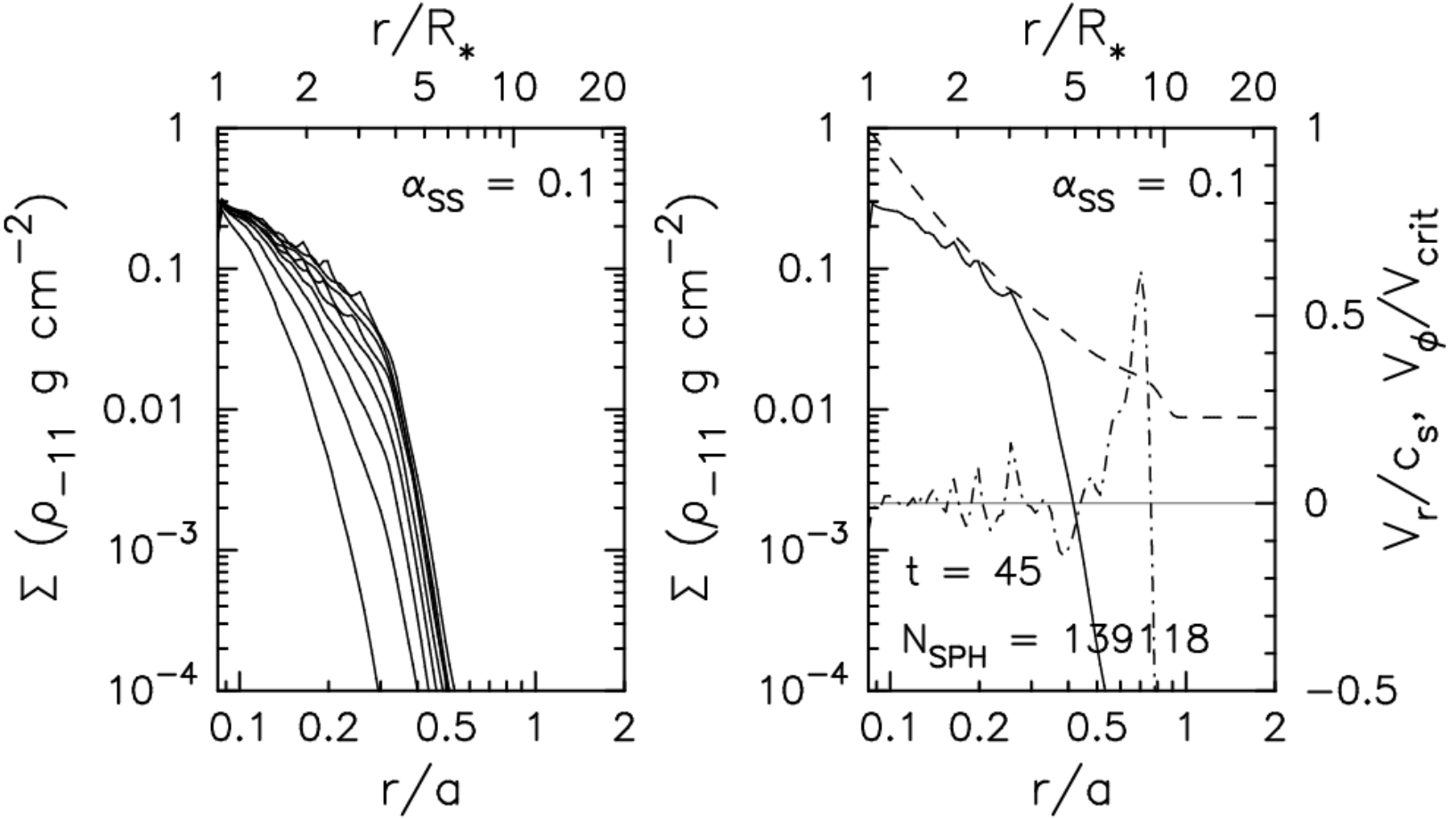

Figure 1.8: Figure 9 from Okazaki et al. (2002). Both plots are created from the results of a high resolution model of a Be/X-ray binary with a neutron star companion. The orbital period and eccentricity of the system are $P_{\rm orb} = 24.3$ days and $e = 0.34$, respectively. The model assumes a constant Shakura-Sunyaev viscosity parameter of $\alpha_{\rm SS} = 0.1$ (see Section 1.4.2). The left panel shows the evolution of the surface density of the disc with time, starting from the lowest curve and ending at the highest. Each contour is separated by five orbital periods. The right panel shows information about the disc structure at the end of the simulation. The solid, dashed and dash-dotted lines denote the surface density, the azimuthal velocity normalised by the critical velocity of the Be star, and the radial Mach number, respectively. In both panels, the density is integrated vertically and averaged azimuthally and the velocity components are averaged both vertically and azimuthally. Two quantities are shown in the right panel: t is the number of orbits that have passed since the beginning of the simulation and $N_{\rm SPH}$ is the number of SPH particles used to model the disc.

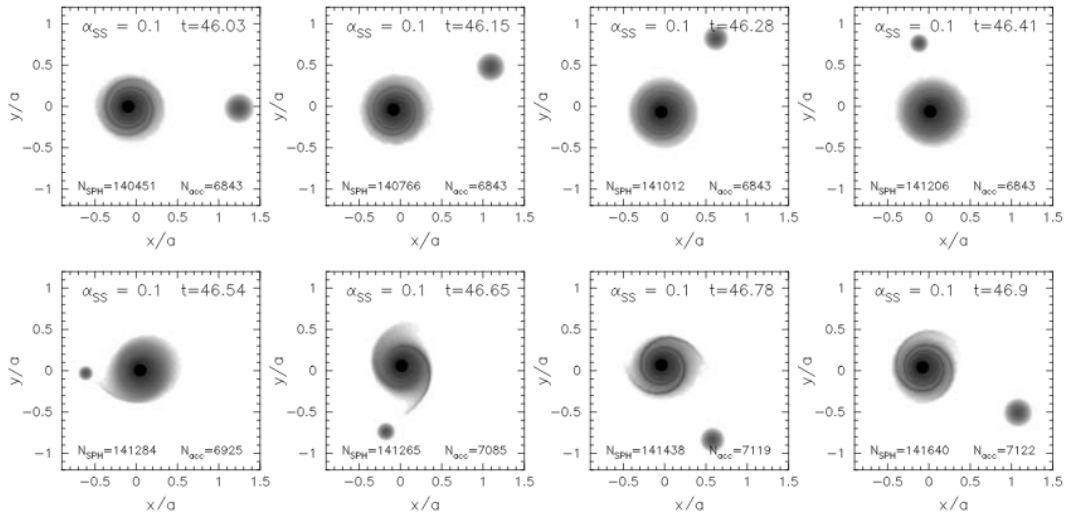

Figure 1.9: Figure 11 from Okazaki et al. (2002). Snapshots of the high resolution system shown in Figure 1.8. The grayscale shows the logarithm of the surface density. The dark spot near the origin is the Be star and the other dark spot orbiting the disc represents the neutron star. Annotated at the top of each panel is the Shakura-Sunyaev parameter, $\alpha_{\rm SS}$, and the elapsed simulation time in units of orbital period. The number of SPH particles, $N_{\rm SPH}$, and the integrated number of particles captured by the neutron star, $N_{\rm acc}$, are shown at the bottom of each panel.

grow whilst the compact object is further away, but is truncated at a smaller radius due to a smaller binary separation at periastron. A spiral structure is excited by the binary partner near periastron and it dissipates due to viscous and Keplerian shear during the rest of the orbit (see Figure 1.9). This effect does occur in circular orbits but exists as a single, less-pronounced arm that tracks the binary partner. Boyle and Walker (1986) made the first attempt to model a Be/X-ray binary with an eccentric orbit, targeting A0538-66. They were able to describe the general characteristics of the interactions between the disc and neutron star but stated that many more particles would be required to produce a detailed model.

All of the work discussed so far is for systems where the orbital plane is the same as the disc plane. There are a wider variety of effects that occur when the disc is misaligned to the orbit of the compact object and this will be discussed in Section 1.3.5.

1.3.5 Misaligned orbits in Be/X-ray binaries

If an asymmetric supernova explosion (see Section 1.3.3) occurs in a binary star system containing a Be star, the explosion can cause the binary orbit to be misaligned with respect to the spin of the unexploded Be star. Should the spin of the Be star be misaligned for any reason, its circumstellar disc will form at an angle to the orbital plane (Martin et al., 2009, 2010). Be stars are thought to commonly possess decretion discs that are misaligned to the binary orbit (Martin et al., 2011).

This is the case for the system modelled in Chapter 5, SXP 5.05, where the disc has an approximate inclination angle of 90°.

Consider a particle orbiting the primary component in a binary system (see Figure 1.10 for an illustration). The particle has negligible mass relative to each star in the binary. The orbit-averaged equations of motion for the particle have a conserved quantity, which is the component of the particle's orbital angular momentum parallel to the angular momentum of the disc-forming star. This conserved quantity can be expressed as follows

$$L_z \propto \sqrt{(1 - e_{\rm p}^2)} \cos i_{\rm p} = \text{constant}, \tag{1.12}$$

where $e_{\rm p}$ is the eccentricity of the particle's orbit and $i_{\rm p}$ is the inclination of the particle's orbital plane to the orbital plane of the binary. Hence, a particle that is initially on a highly misaligned and an initially circular orbit undergoes oscillations to and from more eccentric orbits at smaller inclinations, i.e. closer to the orbital plane. This three-body phenomenon is known as Kozai-Lidov (KL) oscillations (Kozai, 1962; Lidov, 1962).

For KL oscillations to occur, the initial inclination of the particle's orbit must be above a critical value of $\cos^2 i_{\rm p0} < \cos^2 i_{\rm crit} = \frac{3}{5}$, or equivalently $39° \lessapprox i_{\rm p} \lessapprox 141°$. Note that due to the direction of the motion and the position of the ellipse, such a system is not symmetric about 90 degrees. The inclination angle is also bound by the initial and critical inclinations, i.e. $\cos^2 i_{\rm p0} \leq \cos^2 i_{\rm p} \leq \cos^2 i_{\rm crit}$. Using Equation 1.12, the maximum eccentricity for a particle that has an initially circular orbit is given by

$$e_{\rm max} = \sqrt{1 - \frac{5}{3} \cos^2 i_{\rm p0}} \tag{1.13}$$

(Innanen et al., 1997). The period for KL cycles, $\tau_{\rm KL}$, as derived by Kiseleva et al. (1998), is given by

$$\frac{\tau_{\rm KL}}{P_{\rm orb}} \approx \frac{M_1 + M_2}{M_2} \frac{P_{\rm orb}}{P_{\rm p}} (1 - e^2)^{\frac{3}{2}} \tag{1.14}$$

where e is the eccentricity of the binary and $P_{\rm orb}$ and $P_{\rm p}$ are the orbital periods of the binary and the particle, respectively. $\rm M_1$ and $\rm M_2$ are the masses of the primary and secondary of the binary, respectively. For the cases of this thesis, the primary and secondary are the Be star and compact object, respectively.

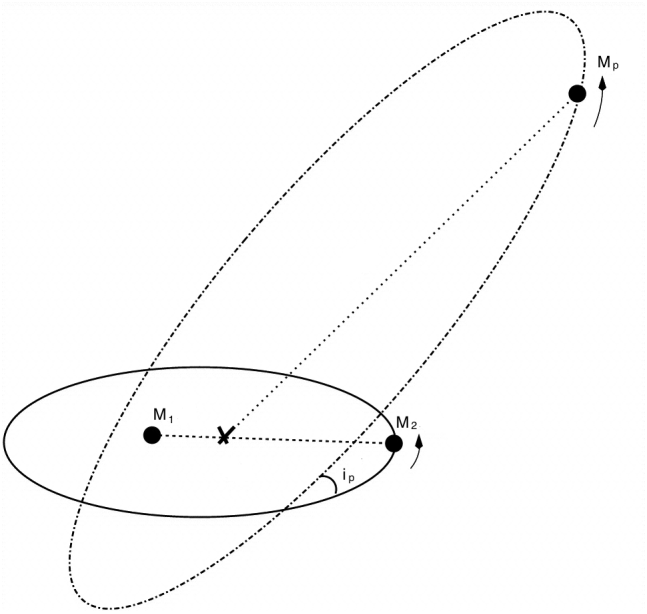

Figure 1.10: Diagram of a particle of mass M_p undergoing Kozai-Lidov oscillations in a binary system. The primary and secondary of the binary have masses of M_1 and M_2, respectively. The orbital plane of the particle is shown at an angle of i_p to the binary orbital plane.

Martin et al. (2014) used three dimensional hydrodynamical simulations to show that highly misaligned accretion discs around one element of a binary system exhibit KL oscillations. They use the SPH, PHANTOM (Price and Federrath, 2010; Lodato and Price, 2010). They implement a standard Shakura-Sunyaev model for the disc as described in Section 1.4.2. In the test particle simulations, it was found that the analytic period for KL cycles (Equation 1.14) should include a dependence on the initial inclination of the orbit. Due to this lack of dependence, Equation 1.14 is only valid up to a factor of a few. They show that the KL mechanism arises in both their test particle simulations and the simulations of an entire disc of hydrodynamic fluid (with no self-gravity). It should be noted that if the self-gravity of the disc is sufficiently strong, the KL oscillations may be suppressed (Batygin, 2012).

Martin et al. (2014) continued this work by applying the simulations to Be/X-ray binaries with the aim of explaining the difference between Type I and Type II outbursts (see Section 1.4). They target the Be/X-ray binary 4U 0115+63 by modelling a system with a binary period of $P_{\rm orb} = 24$ days and an eccentricity of $e = 0.34$. Simulations of all disc inclinations, including coplanar, show regular accretion that occurs every orbit and is likened to Type I outbursts. The simulations with a sufficiently misaligned disc ($i \geq 60°$) form a much larger disc because of the weaker tidal torque. This allows a strong growth of eccentricity in the outer regions of the disc. Thus, the disc becomes eccentric on a faster timescale, i.e. ~ 10 binary orbits. A highly misaligned disc exhibits an additional regime of accretion onto the neutron star. The neutron star accretion rate increases by an

order of magnitude after ~ 21 orbital periods due to the extreme eccentricity of the disc. It is suggested that this is a Type II outburst.

1.4 Accretion

The term accretion refers to the gradual deposition of matter onto the surface of an object under the influence of gravity. As discussed in Section 1.3.2, there are multiple means through which an astrophysical object can accrete matter: Roche Lobe overflow, stellar winds and circumstellar discs. When matter falls onto a massive object, such as a star, the gravitational potential of the matter is converted into other forms of energy such as heat and radiation. In this thesis, Roche Lobe overflow is not relevant because it occurs predominantly in LMXBs and the focus of this thesis is to examine the decretion disc as the dominant source of accretion. In this thesis, accretion is assumed to be the same as the number of particles that fall inside the compact object's radius under gravity. In other words, more complicated accretion mechanisms, such as accretion discs, are neglected.

In its simplest form, accretion is the conversion of the infalling mass directly into a luminosity. For a compact object of mass, M and radius, R the gravitational potential energy released by the accretion of an amount material of mass, m, onto its surface is

$$E = \frac{GMm}{R}. \tag{1.15}$$

The luminosity of any given accreting object can only be, at maximum, equal to the rate of this change in energy due to the infalling material. Energy can be lost through others means such as viscous heating of an accretion disc. Thus, it is conventional to include an efficiency term, η, that represents the fraction of the energy that is converted into radiation (Frank et al., 2002). This yields the following description of luminosity

$$L_{\rm acc} = \eta \frac{GM\dot{m}}{R}. \tag{1.16}$$

where, $\dot{m}$ is the rate of accretion. For a black hole, where the radius is given by Equation 1.11, this simplifies to

$$L_{\rm acc} = \eta \dot{m} c^2. \tag{1.17}$$

Sometimes material falling onto a massive object under the influence of gravity forms an accretion disc to conserve angular momentum. In many cases, the disc flow is confined very close to the disc's orbital plane, so close that the disc can be approximated as two-dimensional. Under the assumption that the disc height is much smaller than its radial size, the properties of the disc can be parameterised entirely by the cylindrical coordinates r, ϕ and z. This is called the thin disc approximation and has been very successful as a basis for a wide variety of models, such as the VDD model (see Section 1.2.4).

There are a number of systems that exhibit large increases (that can be up to an order of magnitude in size) in X-ray luminosity with rise times of $1 \sim 10$ seconds (Lewin and Joss, 1983). These X-ray bursts are only seen in accreting neutron star systems. Such X-ray bursts are separated into two populations: Type I and Type II bursts. Type I bursts are thought to occur when a thin layer of helium, generated from the fusion of accreted hydrogen, is ignited. This thermonuclear flash deposits a huge amount of energy at the surface of the neutron star, heating it and releasing X-rays. Type I bursts are known for having a FRED profile (fast rise, exponential decay): the rise of the peak X-ray luminosity during the burst is very quick and then the brightness decays slowly (∼minutes). Type II bursts are much more erratic, they show no slow decay and can sometimes show rapid successions of bursts separated by a few minutes. The physical mechanism behind Type II bursts has not yet been confirmed and there could be more than one process responsible. The key feature that is agreed upon is that they are due to dramatic changes in the accretion rate of the system.

In Be/X-ray binaries, Type I and Type II outbursts refer to two different mechanisms (Negueruela and Okazaki, 2000) and are sometimes referred to as normal and giant outbursts, respectively, to reduce confusion. Normal outbursts occur once per orbit and typically have an X-ray luminosity of $L_{\mathrm{X}} \sim 10^{36-37}$ erg s^{-1} but there have been systems observed with higher X-ray luminosities during normal outbursts. These outbursts occur due to the regular accretion of the compact object as it passes close to the disc.

Giant outbursts possess luminosities of $L_{\mathrm{X}} > 10^{37}$ erg s^{-1} and can last up to several weeks. They occur less frequently and do not correlate with the orbital parameters. The magnetic field of the neutron star is known to create variations in X-ray flux, because the magnetic pressure can stem the accretion flow until a sufficient mass is supplied. This is suggested to occur in $4U0115+63$ (Campana et al., 2001). However, the neutron star in $A0535+262$ has been shown to have an insufficient magnetic field to cause the variabilities in the X-ray flux (Okazaki, 2013). Thus magnetic pressure this cannot be the only mechanism responsible for giant outbursts. Giant outbursts are generally considered to occur due to large increases in the accreted material during disc warping events (Martin et al., 2014) (see

Section 1.3.5).

1.4.1 Eddington limit

An accreting compact object will radiate energy with the strength of the emission being dependent on the amount of infalling matter. As the photons leaving the surface of the compact object exert a force, there is a point where the infalling matter is obstructed by radiation pressure. This maximum accretion rate is called the Eddington limit (Heinzeller and Duschl, 2007).

Consider a particle with mass, $m_{\rm p}$, and a Thomson cross section of $\sigma_{\rm T}$. The Eddington limit occurs at the point where the luminosity force is equal to the gravitational force on the particle

$$\frac{L\sigma_{\rm T}}{4\pi cr^2} = \frac{GM_X m_{\rm p}}{r^2}. \tag{1.18}$$

Hence, the Eddington luminosity is given by

$$L_{\rm edd} = \frac{4\pi Gcm_{\rm p}}{\sigma_{\rm T}} M_X \approx 3.3 \times 10^4 \left(\frac{M_X}{M_\odot}\right) L_\odot \tag{1.19}$$

and the Eddington accretion limit is given by

$$\dot{M}_{\rm edd} = \frac{4\pi cm_{\rm p}}{\sigma_{\rm T}} R_X \approx 1.5 \times 10^{-8} \left(\frac{R_X}{10{\rm km}}\right) M_\odot\,{\rm yr}^{-1}. \tag{1.20}$$

Most systems that exhibit luminosities greater than the Eddington limit are known for their extreme mass-loss rates such as the O-type star η Car. It underwent outbursts over 150 years ago that suggest mass loss rates of $0.5 M_\odot\,{\rm yr}^{-1}$ (Smith and Owocki, 2006). Some systems, such as novae and supernovae, have been observed to exceed the Eddington luminosity for short periods of time (Shaviv, 2002).

Ultraluminous X-ray sources (ULXs) is the term used for objects that are particularly bright X-ray sources ($L_{\rm X} > 10^{39}$ erg s^{-1}) but are still less luminous than active galactic nuclei (Roberts et al., 2017). These systems are notable because they exceed the Eddington luminosity for neutron stars and even stellar black holes. This is particularly strange because the X-ray emission arises from accretion which is prohibited by the resultant radiation pressure. There are a few suggestions as to what could explain this such as beamed X-ray emission and X-ray

binaries containing black holes with a greater mass than typical stellar black holes (Miller, Fabian and Miller, 2004).

1.4.2 Shakura-Sunyaev viscosity

As one of the most prolific phenomena seen in astrophysics, accretion discs required models that could explain the inward motion of matter orbiting a star or compact object. Shakura and Sunyaev (1973) suggested such a model that caused a step change in the theoretical treatment of all discs. This was generalised to the Kerr-metric by Novikov and Thorne (1973). Even 45 years later, their model (or a modification thereof) is used as a basis for the vast majority of computational discs. All the work in this thesis is performed using a code that implements a Shakura-Sunyav disc model, which we discuss here.

The aim of the model that Shakura and Sunyaev introduced was to describe a geometrically thin non-self gravitating disc using hydrodynamical equations. A number of assumptions are made in the α-model suggested by Shakura and Sunyaev (1973) that are as follows:

- The disc is non-self gravitating: the mass of the disc is much smaller than the mass of the central object, such that the gravitational forces from the disc can be neglected
- The disc is geometrically thin: the height of the disc is much less than the radial distance.
- The disc is steady and does not change significantly with time.
- The disc is axisymmetric and is the same in any given radial direction.
- The azimuthal motion of the material in the disc is much greater than any radial motion.
- The vertical direction maintains hydrostatic equilibrium.
- The disc is optically thick in the vertical direction.
- The disc is radiatively efficient: the viscous heating of the disc is immediately radiated away.
- There are no magnetic fields in the disc.

Angular momentum is transported outwards in accretion discs, allowing for the disc material to flow towards the accreting object. Viscous forces allow both the transport of angular momentum and the radiation of heat away from the disc. In the α-model, viscosity is generated by turbulent motion that is on the same length scales as the height of the disc. The viscosity, ν, is defined as

$$\nu = \alpha c_s H, \tag{1.21}$$

where c_s is the speed of sound in the disc, H is the height of the disc and α is a variable parameter that describes the strength of the viscous forces. The creation of this viscosity term does not actually provide any explanation as to where the viscous forces arise from but simply groups all of the sources into one resultant term. What this does allow is a means to model observed systems and constrain the value of α.

The work outlined by Shakura and Sunyaev (1973) specifically involves black holes but the disc theory is applicable to any disc, provided the disc satisfies the above assumptions. For example, the emission properties of X-ray binaries (Cannizzo, 1993) and UV/soft X-ray emission of AGNs (Sun and Malkan, 1986) have been successfully fitted by this model. New models have been developed from the α-model that allow for the explanation of more complex discs - such as the use of the VDD model to simulate Be star discs (see Section 1.2.4). The inclusion of viscosity in the code used in this thesis is discussed further in Chapter 2.

1.5 Thesis outline

In this thesis, the behaviour of the circumstellar discs of Be stars in Be/X-ray binaries is investigated. The SPH technique is used to model these discs and largely follows the practices of the extensive work of A. T. Okazaki on the same systems, for example in Okazaki et al. (2002). The science in this thesis aims to build on the previous knowledge of the circumstellar discs of Be stars by constraining their properties.

In Chapter 2, the computational method of smoothed particle hydrodynamics is introduced, as well as details of the implementation of the code used throughout the work in this thesis. It begins with a derivation of the basic principles of SPH and the benefit of using a variable smoothing length. Following that, more specific aspects of the SPH code are discussed, such as the assumed interpolation kernel and artificial viscosity. Then the method used for individual particle timesteps is described. Finally, the use of sink particles for the stars is outlined.

Chapter 3 further discusses the details of the SPH code used and the model it implements. Firstly, the model used by the code is covered. The speed up of the code is then tested on both High Performance Computing clusters that were available during the project; Southampton's Iridis 4 and Portsmouth's Sciama cluster. The code implements the shared memory multiprocessing method, OpenMP, and therefore it is important to understand the optimum settings to save

on computational time. General properties of the simulated disc are then presented and compared to the currently accepted model of Be star circumstellar discs. Finally, some early work into line profiles is discussed.

In Chapter 4 an investigation into the general properties of Be/X-ray binaries is performed. Five simulation parameters are varied: the viscosity of the disc, the mass ejection of the Be star, the orientation of the disc relative to the orbital plane and the orbital period and eccentricity of the binary. This is done with the aim to see how certain characteristics (the base gas density, the accretion onto the neutron star and the size of the Be star's disc) of the Be/X-ray binary change with the aforementioned simulation parameters. Then a subset of the simulations that were performed in the earlier parts of the chapter are used to test two observational relations that were found by Coe and Kirk (2015).

Chapter 5 provides an in-depth study into the observable behaviour of a specific Be/neutron star (Be/NS) binary, SXP 5.05. This system underwent an optical outburst in 2013 that is unique to the entirety of its observed behaviour to date. Simulations are performed that target this system during its outburst, requiring a detailed evolution of the mass ejection and viscosity of the Be star's circumstellar disc. The aim is to reproduce the observed I-band data, obscuring column density of neutral hydrogen, X-ray data and Hα line emission. Firstly, the most complete set of data, the OGLE I-band observations, are used as a basis to narrow down the appropriate simulations. As an optical outburst can only be caused by growth in the disc, the visible area of the disc is used as a comparison to the optical data. The column density of neutral hydrogen that obscures the neutron star is used to find the best-fitting simulation and then is used to calculate the X-ray data. Finally, Hα emission line profiles shapes are calculated and compared to the observations.

In Chapter 6, the differences between neutron star and a black hole companions in Be/X-ray binaries are investigated. To date, there has only been one Be/X-ray binary that has been confirmed to contain a black hole, MWC 656 (Casares et al., 2014). Previous work suggests that the truncation of the disc is greater in Be/BH binaries and that this leads to a fainter X-ray source. The aim of this chapter is to provide evidence for the previous two statements. Firstly, the size of the disc is presented for varying compact object mass and varying eccentricity. Then the maximum, average and orbital evolution of the X-ray luminosity is investigated for the same set of simulations.

Finally, Chapter 7 summarises the work in this thesis, gives some concluding discussions and considers further work for the computational modelling of circumstellar discs and their behaviour in Be/X-ray binaries.

Chapter 2

Smoothed Particle Hydrodynamics

The Smoothed Particle Hydrodynamics (SPH) method for describing fluids was first outlined by Lucy (1977) with the intent for use in astrophysical problems. Lucy applies the method to fission in optically thick protostars and it is shown that the technique behaves well at low spatial resolution and can therefore be applied to three-dimensional problems. It also considerably reduces the computational power required to simulate hydrodynamic phenomena. It was also developed independently by Gingold and Monaghan (1977) for polytropic stellar modelling, noting the ability to add rotational and magnetic fields with little difficulty. SPH has since been developed considerably, with the theory of kernel estimation being discussed in Gingold and Monaghan (1982). Monaghan and Gingold (1983) then investigated the simulation of shocks via SPH, showing the need for a new description of artificial viscosity.

This chapter begins by briefly covering the basic principles of SPH and discusses some of its advantages and drawbacks. Then there is a description of the implementation of the code used for the work in this thesis, including the use of varying timesteps for individual particles. Finally, the use of sink particles in the code is elaborated upon.

2.1 Derivation

The original derivation of the principles of SPH was as a Monte-Carlo method to solve the hydrodynamic equations (Lucy, 1977). Following this, functions that interpolate the properties of the fluid were applied to the technique (Gingold and Monaghan, 1982; Monaghan and Gingold, 1983), providing a better estimation of the scaling of the method.

Consider a function $f(\mathbf{r})$ that is defined in a space, $\xi(\mathbf{r})$. A smoothed approximation can be obtained using a kernel function, $W(\mathbf{r}, h)$, as follows

$$\langle f(\mathbf{r})\rangle = \int_{\xi} f(\mathbf{r}')W(\mathbf{r}-\mathbf{r}', h)\mathrm{d}\mathbf{r}'. \tag{2.1}$$

W must satisfy the condition

$$\int_{\xi} W(\mathbf{r}', h)\mathrm{d}\mathbf{r}' = 1. \tag{2.2}$$

This kernel function is parametrised by the *smoothing length*, h, and in the case that $h \to 0$,

$$\langle f(\mathbf{r})\rangle \to f(\mathbf{r}). \tag{2.3}$$

For Equation 2.3 to hold, the kernel is usually strongly peaked at $r = 0$. Hence, the kernel often becomes a delta function of $\mathbf{r}$, $\delta(\mathbf{r})$, as $h \to 0$. Provided that the kernel is indeed strongly peaked, $f(\mathbf{r})$ can be expanded in a Taylor series about $\mathbf{r}$. If it is also an even function then the leading term in h vanishes and the following is recovered

$$\langle f(\mathbf{r})\rangle = f(\mathbf{r}) + \mathcal{O}(h^2). \tag{2.4}$$

In the additional case, that the kernel is a function of r alone (i.e. it is spherically symmetric), then

$$\langle f(\mathbf{r})\rangle = f(\mathbf{r}) + c\frac{h^2}{6} \bigtriangledown^2 f(\mathbf{r}) + \mathcal{O}(h^3), \tag{2.5}$$

where c is independent of h. A function $f(\mathbf{r})$ can always be replaced by a smoothed equivalent to within the accuracy of the smoothing process and means that for any 2 functions $A(\mathbf{r})$ and $B(\mathbf{r})$

$$\left\langle \frac{A(\mathbf{r})}{B(\mathbf{r})} \right\rangle = \frac{\langle A(\mathbf{r})\rangle}{\langle B(\mathbf{r})\rangle} + \mathcal{O}(h^2). \tag{2.6}$$

Consider that there are N discrete points of information about the system and the points are distributed as

$$n(\mathbf{r}) = \sum_{j=1}^{N} \delta(\mathbf{r} - \mathbf{r}_j), \tag{2.7}$$

then it is possible to multiply the integrand in Equation 2.1 by $n(\mathbf{r}')/\langle n(\mathbf{r}')\rangle$ whilst preserving the accuracy of the method. Doing so reduces the integrand to

$$\langle f(\mathbf{r})\rangle = \sum_{j=1}^{N} \frac{f(\mathbf{r}_j)}{\langle n(\mathbf{r}_j)\rangle} W(\mathbf{r} - \mathbf{r}_j, h). \tag{2.8}$$

SPH describes the system by using points to represent fluid elements and hence, each point has an associated mass, m_j. Therefore, the number density at a given position, $\mathbf{r}_j$, can be written as

$$\langle n(\mathbf{r}_j)\rangle = \frac{\rho(\mathbf{r}_j)}{m_j}. \tag{2.9}$$

We can also update Equation 2.8 with the substitution of Equation 2.9

$$\langle f(\mathbf{r})\rangle = \sum_{j=1}^{N} \frac{m_j}{\rho(\mathbf{r}_j)} f(\mathbf{r}_j) W(\mathbf{r} - \mathbf{r}_j, h). \tag{2.10}$$

This equation is the starting point for SPH as it leads to smoothed approximations of all the physical quantities of the fluid. The most evident example of this is density, where $f(\mathbf{r}) \equiv \rho(\mathbf{r})$ and thus the smoothed approximation is

$$\langle \rho(\mathbf{r})\rangle = \sum_{j=1}^{N} m_j W(\mathbf{r} - \mathbf{r}_j, h). \tag{2.11}$$

Replacing the physical quantities of a fluid with summations over weighted particles allows for each quantity to be described by a continuous function. When no particles are lost from a SPH simulation, the continuity equation is satisfied by Equation 2.11 (Benz, 1990).

It is also important to determine the smoothed versions of the gradients of the

physical properties. Following the definition of a smoothed quantity in Equation 2.1 the gradient of a fluid property is given by

$$\langle \bigtriangledown f(\mathbf{r}) \rangle = \int_{\xi} \bigtriangledown f(\mathbf{r}') W(\mathbf{r} - \mathbf{r}', h) \mathrm{d}\mathbf{r}'. \tag{2.12}$$

Using integration by parts, it can be rewritten as

$$\langle \bigtriangledown f(\mathbf{r}) \rangle = \int_{S} f(\mathbf{r}') W(\mathbf{r} - \mathbf{r}', h) \ \mathbf{n} \ \mathrm{d}a + \int_{\xi} f(\mathbf{r}') \bigtriangledown W(\mathbf{r} - \mathbf{r}', h) \mathrm{d}\mathbf{r}'. \tag{2.13}$$

Provided the solution space extends far enough such that either the kernel or the function, $f(\mathbf{r})$, vanishes then the first term can be neglected. Then the second term in Equation 2.13 can be rewritten as a summation as follows

$$\langle \bigtriangledown f(\mathbf{r}) \rangle = \sum_{j=1}^{N} \frac{m_j}{\rho(\mathbf{r}_j)} f(\mathbf{r}_j) \bigtriangledown W(\mathbf{r} - \mathbf{r}_j, h). \tag{2.14}$$

Equation 2.10 and Equation 2.14 provide a method to determine the smoothed versions of a simulated fluid's quantities and the local gradient of any quantity. However, it is required that the gradient of the kernel function does not vanish. Calculating gradients is important for pressure and viscous forces which is, in turn, vital to evaluate the motion of the particles.

SPH is a Lagrangian method, meaning that it uses information on the dynamics of the system, i.e. the SPH particles are the equivalent of the grid in other numerical methods. They form a moving grid with the forces between them evaluated via the interpolating kernel. As the particles mirror the density distribution, spatial resolution issues are straightforwardly solved with SPH as regions requiring higher spatial resolution will naturally be populated by more particles.

2.1.1 Variable smoothing lengths

To fully utilise the dynamic spatial resolution of SPH, a variable smoothing length must be implemented. Consider a particle in a system modelled by SPH that lies a distance greater than the smoothing length from any other particle. Smoothed quantities for this particle cannot be evaluated as it has no neighbours. Hence, it does not make sense to prescribe the same smoothing length, h, to every single particle in a system modelled by SPH. In other words, the smoothing length must

be dependent on the spatial resolution that is required. As the particles in SPH can move to regions of different particle density, smoothing length must be dependent on space and time.

However, when the smoothing length varies spatially, the errors derived in Equation 2.5 and Equation 2.6 must be reconsidered. Equation 2.1 is now

$$\langle f(\mathbf{r})\rangle = \int_{\xi} f(\mathbf{r}')W(\mathbf{r}-\mathbf{r}', h(\mathbf{r}'))\mathrm{d}\mathbf{r}'. \tag{2.15}$$

It has been shown that the additional errors caused by a spatially dependent smoothing length are of second order (Monaghan, 1985; Hernuist and Katz, 1989). Therefore, the errors remain of the same order of those that are inherent to SPH.

However, the gradient of the fluid properties does not remain the same due to the new dependence of the smoothing length on $\mathbf{r}$. With the spatially dependent smoothing length, the gradient of the kernel is given by

$$\bigtriangledown_{\mathbf{r}} W(\mathbf{r}-\mathbf{r}', h(\mathbf{r})) = -\frac{1}{|\mathbf{r}-\mathbf{r}'|}\frac{\partial W}{\partial(\mathbf{r}-\mathbf{r}')}(\mathbf{r}-\mathbf{r}') + \frac{\partial W}{\partial h}\bigtriangledown_{\mathbf{r}} h(\mathbf{r}). \tag{2.16}$$

The second term exists if the smoothing length is dependent on $\mathbf{r}$ and was found to be important only in the case where the smoothing length varies on a smaller scale than itself (Evrard, 1988). Hence, as the quantities in SPH tend to be evaluated on a similar scale to the smoothing length, this term is reasonable to neglect. However, Nelson and Papaloizou (1994) showed that including the extra term leads to a marginally improved energy conservation.

The calculation of the force on a particle obviously requires the subsequent opposite force to be exerted on another particle. However, if the smoothing length is different for the two SPH particles, then momentum is not conserved. Thus, a spatially varying smoothing length, unless considered carefully, can violate the law of conservation of momentum. There have been multiple suggestions for the solution of this issue (Gingold and Monaghan, 1982; Evrard, 1988; Hernuist and Katz, 1989). The method used in the code is one that replaces h in the above equations with

$$h(\mathbf{r}, \mathbf{r}') = \frac{h(\mathbf{r}) + h(\mathbf{r}')}{2}, \tag{2.17}$$

or for discrete particles

$$h_{\rm ij} = \frac{h_{\rm i} + h_{\rm j}}{2}. \tag{2.18}$$

This is the method described by Evrard (1988) and subsequently, described by Benz (1990). The implementation of a spatially varying smoothing length maximises the ability of SPH to resolve both high and low-density regions simultaneously. The method of updating the smoothing length is discussed later in Section 2.2.6.

2.2 Code specific implementation

Using the principles outlined above, specific SPH equations for a gaseous disc will now be presented. The interpolation kernel will be discussed first and then the fluid equations will be derived. Finally, individual particle time steps, the time integration and the method of updating the smoothing length will be discussed.

For the remainder of this chapter, all quantities are smoothed and the angled brackets that denote smoothed fluid properties are dropped. All smoothed disc quantities used in this section are still subject to the errors discussed in Section 2.1.

2.2.1 The interpolation kernel

Due to the importance of interpolation in SPH, there have been many suggestions for appropriate kernels. Initially, Gingold and Monaghan (1977) used Gaussian, spherical kernels for three-dimensional problems, of the following form

$$W(r,h) = \frac{1}{\pi^{3/2}h^3} \exp -v^2 \tag{2.19}$$

where $r = |\mathbf{r} - \mathbf{r}'|$ and $v = r/h$. Note that this treatment and other early forms of interpolation kernel include all the simulation particles in the summation. As the fluid forces, density and pressure are all local quantities, it is a waste of computational time to sum over all particles.

It is therefore pertinent to use a kernel that only includes contributions from particles that lie within a given distance and that is related to the smoothing length. The spline kernel developed by Monaghan and Lattanzio (1985) is used within the code and is given by

$$W(r,h) = \frac{\sigma}{h^{\nu}} \begin{cases} 1 - \frac{3}{2}v^2 + \frac{3}{4}v^3 & \text{if } 0 \leq v \leq 1, \\ \frac{1}{4}(2-v)^2 & \text{if } 1 \leq v \leq 2, \\ 0 & \text{otherwise,} \end{cases} \tag{2.20}$$

where ν is the number of dimensions and σ is the normalisation with values of $2/3$, $10/7\pi$ and $1/\pi$ for one, two and three dimensions, respectively. This kernel is much less computationally expensive than the one shown in Equation 2.19, requiring only a small number of neighbouring SPH particles to determine the smoothed quantities.

2.2.2 Equation of state

Now that the interpolation kernel has been determined, the equations describing the properties of the fluid can be rewritten. Note that the kernel is finite and extends only to a radius of $2h$. Density can now be written in terms of the masses of the respective particle and its neighbours as follows

$$\rho_{\mathrm{i}} = m_{\mathrm{i}} W(0, h_{\mathrm{i}}) + \sum_{\mathrm{j}=1}^{N_{\mathrm{n}}} m_{\mathrm{j}} W(r_{\mathrm{ij}}, h_{\mathrm{ij}}), \tag{2.21}$$

where N_{n} is the number of neighbours of particle i and $r_{\mathrm{ij}} = |\ \mathbf{r}_{\mathrm{i}}\ - \mathbf{r}_{\mathrm{j}}|$.

It is also important to define the pressure of the fluid, P. The circumstellar disc is, for the most part, modelled well as isothermal (with a temperature of $T = 0.6T_{eff}$ (Poeckert and Marlborough, 1982; van Kerkwijk et al., 1995; Carciofi and Bjorkman, 2006). Hence, only the isothermal equation of state is necessary. It is given by

$$P = c_s^2 \rho, \tag{2.22}$$

where c_s is the speed of sound in the isothermal gas. Due to the isothermal treatment of the equation of state, energy conservation is inherently satisfied. Modelling the Be star's circumstellar disc as anything other than isothermal requires considerably more work because the disc reprocesses the emission from the star leading to a complex temperature and ionisation structure in the disc. This is out of the scope of this thesis.

2.2.3 Momentum equation

In the absence of gravity, conservation of momentum for an inviscid fluid is given by

$$\frac{\partial \mathbf{v}}{\partial t} + (\mathbf{v} \cdot \bigtriangledown)\mathbf{v} = -\frac{\bigtriangledown P}{\rho}. \tag{2.23}$$

If both sides are multiplied by the interpolation kernel and integrated over the solution space, we get

$$\int_{\xi} W(r', h)\frac{\partial \mathbf{v}}{\partial t}\mathrm{d}\mathbf{r}' + \int_{\xi} W(r', h)(\mathbf{v} \cdot \bigtriangledown)\mathbf{v}\mathrm{d}\mathbf{r}' = -\int_{\xi} W(r', h)\frac{\bigtriangledown P}{\rho}\mathrm{d}\mathbf{r}'. \tag{2.24}$$

Finally, the following is obtained

$$\frac{\mathrm{d}\mathbf{v}}{\mathrm{d}t} = -\bigtriangledown_{\mathrm{r}}\left(\frac{P}{\rho}\right) - \left(\frac{P}{\rho^2}\right)\bigtriangledown_{\mathrm{r}}\,\rho. \tag{2.25}$$

This equation can then be converted into a summation over the SPH particles, as described in Section 2.1. The SPH momentum equation is therefore given by

$$\frac{\mathrm{d}\mathbf{v}_{\mathrm{i}}}{\mathrm{d}t} = -\sum_{\mathrm{j}=1}^{N_{\mathrm{n}}} m_{\mathrm{j}}\left(\frac{P_{\mathrm{i}}}{\rho_{\mathrm{i}}^2} + \frac{P_{\mathrm{j}}}{\rho_{\mathrm{j}}^2}\right)\bigtriangledown_{\mathrm{i}}\,W(r_{\mathrm{ij}}, h_{\mathrm{ij}}), \tag{2.26}$$

where $\bigtriangledown_{\mathrm{i}}$ takes the gradient with respect to the coordinates of particle i. Not only does this equation conserve momentum, it also conserves local angular momentum because all the forces are directed along a line joining the centres of the particles.

2.2.4 Artifical viscosity

Up until this point, all the derived equations for SPH have been for a fluid with negligible or no viscosity. Energy contained in shocks can always be converted to heat in a viscous fluid regardless of the strength of the viscous forces. Viscosity in real fluids allows for the dissipation of heat and without this consideration in the model there is no process by which kinetic energy can be converted into thermal energy. Thus, without introducing an artificial viscosity, the above equations cannot correctly model shocks. In most astrophysical fluids, the viscosity is small.

There are two forms of viscosity that are implemented in the code. Both are equivalent to viscosity pressures and are given by

$$P_\alpha = \Pi_\alpha \rho^2 = -\alpha \rho l c_s \bigtriangledown \cdot \mathbf{v}, \tag{2.27}$$

and

$$P_\beta = \Pi_\beta \rho^2 = -\beta \rho l^2 (\bigtriangledown \cdot \mathbf{v})^2, \tag{2.28}$$

where α and β are free parameters that determine the strength of each viscosity term and l is a typical length scale over which the shock is spread. Both of these viscosity terms behave as bulk viscosities. Note that α is the Shakura-Sunyaev viscosity parameter (see Section 1.4.2). Equation 2.27 is designed primarily to eliminate subsonic velocity oscillations. Equation 2.28 is a second-order, Von Neumann-Richter viscosity. Since it is dependent on the square of the divergence, this form of viscosity becomes more important in the supersonic regime to prevent the particles from passing through each other when very fast shocks occur, i.e. at high Mach numbers. The values for α and β depend largely on the type of astrophysical fluid being modelled but often they are set to $\alpha \approx 1$ and $\beta \approx 2$. For the circumstellar discs of Be stars, α is typically varied between 0.1 and 1.5 depending on the state of the disc and the rate of mass ejection of the Be star (Rímulo et al., 2018). The velocity of the material in the Be star's decretion disc is rarely supersonic so β can safely be set to zero.

The methods used for these two of viscosities are the ones prescribed by Monaghan and Gingold (Monaghan and Gingold, 1983; Benz, 1990; Monaghan, 1992). Although these formulations are now quite old, they have been shown to model shocks well (Monaghan and Gingold, 1983) and are certainly sufficient for the purposes of simulating the decretion discs of Be stars. The artificial viscosity as used in the code, is given by

$$\Pi_{\mathrm{ij}} = \begin{cases} (-\alpha c_{\mathrm{s}} \mu_{\mathrm{ij}} + \beta \mu_{\mathrm{ij}}^2)/\rho_{\mathrm{ij}} & \text{if } \mathbf{v}_{\mathrm{ij}} \cdot \mathbf{r}_{\mathrm{ij}} \leq 0, \\ 0 & \text{if } \mathbf{v}_{\mathrm{ij}} \cdot \mathbf{r}_{\mathrm{ij}} > 0, \end{cases} \tag{2.29}$$

where $\rho_{\mathrm{ij}} = 0.5 \times (\rho_{\mathrm{i}} + \rho_{\mathrm{j}})$ and

$$\mu_{\rm ij} = \frac{h\mathbf{v}_{\rm ij} \cdot \mathbf{r}_{\rm ij}}{\mathbf{r}_{\rm ij} + \eta^2}, \tag{2.30}$$

where $\mathbf{v}_{\rm ij} = \mathbf{v}_{\rm i} - \mathbf{v}_{\rm j}$ and $\eta = 0.1h$. The quantity η is included to prevent the divergence of $\mu_{\rm ij}$ for small separations between particles.

The viscosity is then added to the momentum equation (see Equation 2.26) in the following way

$$\frac{{\rm d}\mathbf{v}_{\rm i}}{{\rm d}t} = -\sum_{\rm j=1}^{N_{\rm n}} m_{\rm j} \left(\frac{P_{\rm i}}{\rho_{\rm i}^2} + \frac{P_{\rm j}}{\rho_{\rm j}^2} + \Pi_{\rm ij} \right) \bigtriangledown_{\rm i} W(r_{\rm ij}, h_{\rm ij}). \tag{2.31}$$

2.2.5 Time integration

When performing simulations, it is vital to have computational time steps that are smaller than any important physical timescale. Failing to do so leads to inaccuracies and often a completely unphysical model. As it takes longer to simulate a system using smaller time steps, it is good practice to utilise the largest time steps possible whilst maintaining the physics.

The base method used for the time integration of the SPH equations in the code is a second order, Runge-Kutta-Fehlberg technique (Albrecht, 1996) with an adaptive time step. The time step for the integration in this method is determined by constraining the changes of certain physical quantities within a given tolerance. This tolerance determines the accuracy of the method. Velocity, acceleration, internal energy and smoothing length are the important variables to consider when determining the time integration step of the simulation. Each time step in the method is followed by a time step determined using the following condition

$$\delta t_{\rm RKF} = \sqrt{\frac{512 \ \ \delta t_{\rm old} \ \lambda}{|Q_{\rm new} - Q_{\rm old}|}}, \tag{2.32}$$

where Q is each physical quantity in turn, and λ is the given tolerance. This method in its basic form constrains all the simulation particles to move with one integration step. The global time step is the minimum of this condition for each physical quantity and for every simulation particle.

In many astrophysical systems, the circumstellar disc of a Be star included, the particles that lie in the regions of highest and lowest density are orders of magnitude different in their spacing. This means that the minimum time step required to

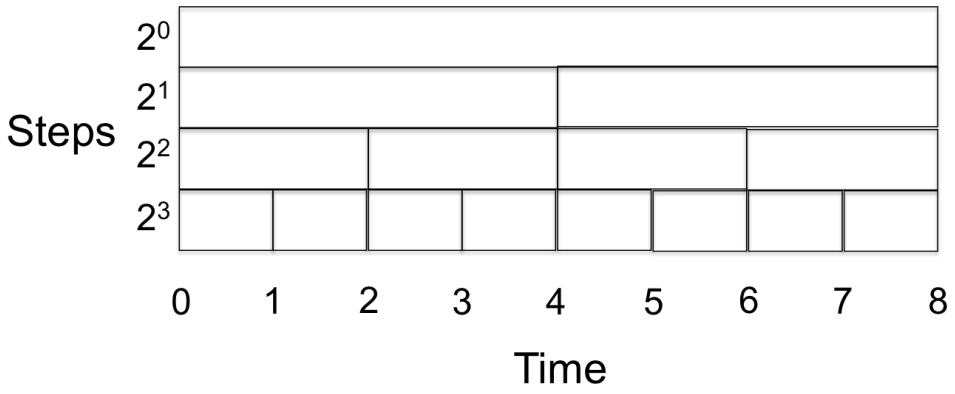

Figure 2.1: An example of the time steps of particles in an individual-time-steps program. Here, there are four levels of time step allowed. The largest time step is the top level, and also corresponds to the synchronisation time at which all the particles are evolved together. The smallest time step is a factor of 2^3 smaller than the largest time step. Clearly, any particle can reduce its time step at any time, as it is always being evolved at the same time as particles with shorter time steps. However, for a particle to increase its time step, it must be being evaluated at the same time as a particle which has a larger time step, otherwise it is not synchronised at the next synchronisation step.

preserve the physics is drastically different. Rather than evolve the entire simulation at the small intervals required by the dense regions, the code implements individual time steps for each SPH particle. A great deal of computational expense is saved by using this method and it was the first major modification made by M. Bate upon receiving the code from W. Benz (Bate et al, 1995).

The code calculates an individual time step for each particle and then they are grouped into bins that are multiples of two times the minimum time step for the simulation. This means that some particles are evaluated at time steps larger than required but it allows for entire groups of particles to be evolved at appropriate time steps. Figure 2.1 illustrates the advantage of the bins being multiples of two - it allows for a hierarchy of grouping in time. Every two time steps, the particles being evaluated at the smallest interval are evolved at the same time as those particles binned at the time step twice the size. This is the same for all groupings of particles up to the largest time step. The method also means that forces between particles only need to be calculated once for each group rather than every individual time step. This leads to considerably reduced computation.

The Runge-Kutta-Fehlberg is no longer sufficient when implementing individual time steps because it is dependent on the properties of the fluid as a whole. Two extra conditions are then required in the determination of the particle time steps: the Courant condition and the force condition, both given in Monaghan (1992).

The first of these two conditions is found by considering a characteristic length scale divided by a characteristic velocity. It is given by

$$\delta t_{cv} = \frac{0.3h}{c_s + h|\bigtriangledown \cdot \mathbf{v}| + 1.2(\alpha c_s + \beta h|\bigtriangledown \cdot \mathbf{v}|)} \tag{2.33}$$

where α and β are the two viscosity parameters (from Equations 2.27 and 2.28) and the final term in the denominator is only included if $\bigtriangledown \cdot \mathbf{v} < 0$. The condition is labelled δt_{cv} because it includes both the Courant condition and the viscous diffusion condition of the fluid (Monaghan, 1989).

The second of these conditions is given by

$$\delta t_f = 0.3\sqrt{\frac{h}{|\mathbf{F}|}} \tag{2.34}$$

where $\mathbf{F}$ is the net acceleration on the particle. These two conditions allow for the method of individual time steps to behave the same as a method using a single time interval for all particles.

The time step for each particle is determined by finding the minimum of the three above conditions (i.e. Equations 2.32, 2.33, 2.34) and then they are all binned in multiples of two. It is important to allow particles to change the time interval at which they are evaluated because it can further save computational expense and particles may move to denser regions that require higher time resolution. Particles in the simulation are allowed to move to larger or smaller time steps but when moving to a larger one, it must fulfil the condition that

$$(\mathrm{d}t_{\mathrm{sync}} - t) \mod \mathrm{d}t = 0, \tag{2.35}$$

where t is the current time, $\mathrm{d}t$ is the time step the particle is transitioning to (that is larger) and $\mathrm{d}t_{\mathrm{sync}}$ is the time at which the particles are synchronised. In addition to this, particles can only increase their time step a maximum of once every two consecutive steps to avoid synchronisation errors. However, particles can reduce their time step as much as is needed.

2.2.6 Varying the smoothing length

As discussed earlier in Section 2.1.1, it is desirable to have a smoothing length that varies spatially to allow regions of different densities to be properly resolved. This means it is important to have an appropriate number of neighbours to perform the SPH summations over. A small number of neighbours can lead to large statistical

Table 2.1: Table of the lower and upper boundaries for the number of neighbours in each dimension, N_{lower} and N_{upper}. Also included is the dimension dependent constant, n_{range}, that is used in Equation 2.40.

Dimensions	N_{lower}	N_{upper}	n_{range}
1	5	10	1
2	20	35	5
3	30	70	12

errors when calculating any smoothed properties. If there are no neighbouring particles at all, the forces and pressure of the fluid simply cannot be calculated at that point, causing the failure of the entire program. In contrast, a very large number of neighbouring particles is more computationally expensive. Hence, it is desirable to have the minimum number of neighbouring particles (to reduce computation time) while retaining a sufficiently large number to keep errors low. The code aims to provide $\sim 10 - 70$ neighbours for each SPH particle, where the number required is proportional to the number of dimensions (see Table 2.1). As all the work presented in this thesis is in three dimensions, the number of neighbouring particles is kept close to ~ 50.

Not only can any SPH particle move to a region with a differing density but the density field of the fluid is free to vary. Therefore, it is necessary for the smoothing length to vary with time so that the number of neighbours can remain near constant. To find the new smoothing length whilst keeping the number of neighbours the same, the following must be adhered to

$$h = h_{\text{old}} \left(\frac{\rho_{\text{old}}}{\rho} \right)^{1/\nu} \tag{2.36}$$

where h_{old} and ρ_{old} are the smoothing length and density before the particle moves to a new region and h and ρ are the new values for smoothing length and density. ν is the number of dimensions. Note that the determination of ρ requires the smoothing length (Equation 2.21). As shown in Benz (1990), the derivative of this can be taken to acquire the following (assuming $\nu = 3$)

$$\frac{\mathrm{d}h}{\mathrm{d}t} = -\frac{1}{3} \frac{h}{\rho} \frac{\mathrm{d}\rho}{\mathrm{d}t}. \tag{2.37}$$

The time derivative of density can then be replaced using the continuity equation, yielding the following

$$\frac{\mathrm{d}h_i}{\mathrm{d}t} = \frac{1}{3}h \bigtriangledown \cdot \mathbf{v}_\mathrm{i}. \tag{2.38}$$

This is the equation used for varying the smoothing length and is integrated in time alongside all the other SPH equations. Sometimes, this equation fails to keep the number of neighbours constant and approaches the upper or lower band. Should this occur, Equation 2.38 is replaced by

$$\frac{\mathrm{d}h_i}{\mathrm{d}t} = \frac{\frac{1}{3}e^x(h \bigtriangledown \cdot \mathbf{v}_\mathrm{i}) \pm e^{-x}2h_\mathrm{i}}{e^x + e^{-x}}, \tag{2.39}$$

where + is chosen if the smoothing length needs to increase and − is chosen if the reverse is true. The parameter, x, is given by

$$x = \begin{cases} (N_\mathrm{upper} - N_\mathrm{n})/(0.3n_\mathrm{range}) & \mathrm{if}(N_\mathrm{upper} - N_\mathrm{n}) < n_\mathrm{range}, \\ (N_\mathrm{n} - N_\mathrm{lower})/(0.3n_\mathrm{range}) & \mathrm{if}(N_\mathrm{n} - N_\mathrm{lower}) < n_\mathrm{range}, \\ \infty & \mathrm{otherwise}, \end{cases} \tag{2.40}$$

where N_upper and N_lower are the upper and lower bands on the number of neighbours a SPH particle should have and n_range is an integer dependent on the number of dimensions (for values of both see Table 2.1). This equation causes the number of neighbours to converge to the desired range should Equation 2.38 ever fail to do so.

2.3 Sink particles

An important aspect of computational modelling is providing simplifications to allow the model to explain physical systems at a reasonable computational expense. In the case where systems reach a large range between the maximum and minimum densities, such as the formation of stars, it is helpful to find methods to accommodate it. The Lagrangian method, SPH, is one such way of alleviating some of these difficulties but an additional simplification that can be made is to use "sink particles". Accreting objects in simulations can be replaced by a single non-gaseous particle that has different properties from the SPH gas particles, such as a polytropic equation of state for a star.

The concept of accreting non-gaseous particles were considered outside of Lagrangian methods by Boss and Black (1982) to investigate the collapse of rotating, isothermal interstellar clouds. They use a finite-difference code with a

central cell designated as a sink cell with a mass and angular momentum of the particles that it replaces. The angular momentum of the sink particle is used to check for global conservation of angular momentum and has no effect on the dynamics of the simulation. This sink cell can then accrete gaseous particles when appropriate, avoiding the need for committing computational time to modelling the central object itself. However, it is fixed in place and so is insufficient for modelling binaries or multiple astrophysical objects with relative motion.

Sink particles in the acquired code were used to aid in the modelling of multiple star formation by Bate et al (1995). Accreting protostars are very computationally expensive to model because a large number of particles become dedicated to the high density regions within each protostar. However, the internal evolution is not of interest in determining where material from the star-forming cloud ends up. Hence, such objects can be replaced with a non-gaseous particle with a mass, linear momentum and angular momentum of the particles that it replaces. Much like the sink cell, these sink particles can then accrete infalling matter simply.

Both the aforementioned applications of sink particles are used to remove massive objects that are not of specific interest in the simulations. Both Boss and Black (1982) and Bate et al (1995) were interested in the evolution of the collapsing clouds of matter rather than the central object that was accreting the material. This is similarly the case for the simulations performed in the work throughout this thesis: the circumstellar disc of the Be star is of interest and not the interior of the Be star itself nor its binary companion. Hence, both components of the binary are modelled using sink particles.

This section will briefly cover the two most important features of the implementation of sink particles in the code. The first is the method of accretion of matter onto the sink particle. The second is the boundary conditions between the sink particle and the surrounding gas particles. The code does contain the additional capability to dynamically create new sink particles but this is not necessary to model Be/X-ray binaries.

2.3.1 Accretion onto sink particles

As the sink particle possesses no properties other than mass and momentum, it interacts with other particles only through gravity. Particles that enter a certain radius can be accreted by the sink particle. There are two accretion radii implemented in the code: an inner and outer accretion radius. The inner accretion radius is an absolute boundary of the star, i.e. any gas particle moving inside this radius is accreted with no exception. The sink particle largely functions as a single point in the simulations but this accretion radius acts as the radius of the star, providing a surface for the SPH particles to interact with.

The outer accretion radius is more complex. Any gas particle that comes within the accretion radius must satisfy several criteria to confirm if it should be accreted. Firstly, the particle must be gravitationally bound to the sink particle. Then the angular momentum of the particle about the sink particle must be less than that required to form a circular orbit. Finally, the gas particle must be more tightly bound to the candidate sink particle than any other sink particle. This outer accretion radius was implemented in the initial code to ensure that particles that would leave the accretion radius would not be accreted and also to ensure that gas particles are not accreted prematurely by another sink particle lying close to the candidate. Bate et al (1995) used an outer accretion radius that is 10-100 times larger than the inner radius. This is because when modelling collapsing clouds and the formation of protostars, it is important to make sure that the correct sink particle accretes the SPH particle first. For the simulations of Be/X-ray binaries, it is still implemented but at a size slightly larger than the actual radius of the star (~ 1.1). This acts as a means to minimise the large number of interactions that occur at the Be star's surface but is otherwise not very important as the Be star and compact object are in close proximity.

When a gas particle is accreted, the sink particle acquires its mass, linear momentum and angular momentum. The sink particle's position is then moved to the centre of mass of the accreted particle and the sink particle. The gas particle is then labelled as accreted and is removed or repurposed as a newly injected particle at the Be star's surface (this will be discussed in greater detail in Chapter 3). There is an absence of an accretion disc surrounding the sink particle modelling the neutron star which is a major simplification. The consequences of this will be further considered in Chapter 3.

2.3.2 Boundaries for sink particles

As with any simplification, the replacement of stars with a single point has inaccuracies that need to be accounted for. A large problem is the discontinuity in the number of SPH particles that occurs at the accretion radius of the sink particle. The nature of SPH is that it determines the properties of the fluid from neighbouring particles and so such a discontinuity is obviously a problem. Here the corrections to boundary conditions are briefly discussed but for further details on these corrections and the testing of sink particles in the code, see Bate et al (1995).

There are four aspects of the simulation that need to be altered to accommodate this issue. The first of these is the fact that the density of particles close to the accretion radius are underestimated because of these missing neighbours in the summation in Equation 2.21. To correct for this, the neighbouring particles are separated into two groups: those in between the SPH particle and the sink particle

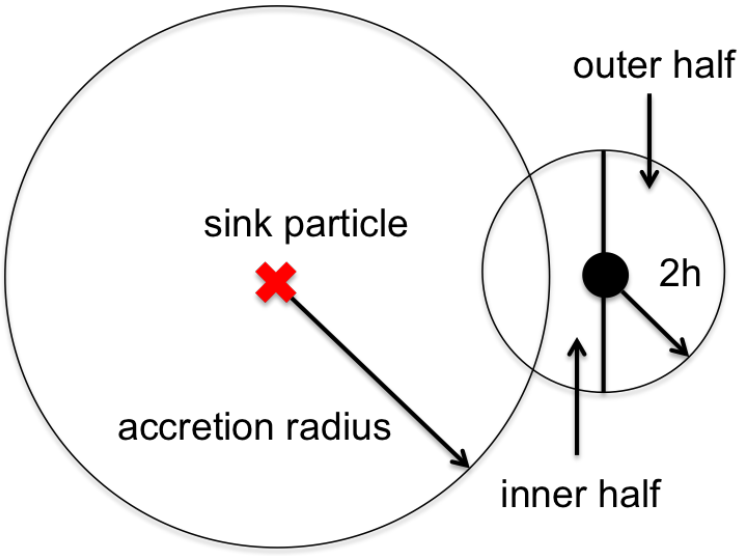

Figure 2.2: An illustration of the sink particle implementation with an SPH gas particle close to the accretion radius. The sink particle and SPH particle are represented by the red cross and solid black circle, respectively. The sink particle is surrounded by a circle that demonstrates its assumed accretion radius. The SPH particle's kernel cutoff (at $2h$) is shown by the smaller circle and is separated into two sections: the inner and outer halves of the circle. The inner half overlaps with the accretion radius and so is missing some neighbouring particles. The outer half, however, is unaffected by the proximity to the accretion radius.

and the neighbours lying outside of both (see Figure 2.2). For a gas particle that is close to the accretion radius of the sink particle, the inner group of neighbours is depleted by the accretion radius. A linear fit of the density gradient is made for both the inner and outer group and the comparison between these two fits allows for a correction to density to be determined.

Secondly, the smoothing lengths of the particles close to any sink particle's accretion radius also need to be larger. As mentioned before in Section 2.2.6, it is desirable to keep the number of neighbours roughly constant and a particle at the accretion radius can be missing up to half the neighbouring particles it should have. The smoothing length is altered at the same time as density. When the inner and outer groups are compared, the number of missing neighbouring particles is calculated from the density correction. It is assumed that the neighbours are somewhat equally spaced in both groups. This number of missing neighbours allows the smoothing length to be changed accordingly.

The third issue is that the particles at the edge of the boundary of accretion experience a lack of pressure forces due to the absence of SPH particles. Hence, they are more likely to fall into the sink particle's accretion for the radius. The pressure correction is calculated using the same method as density but it is only necessary to change the radial pressure forces. This is because any missing pressure force due to the accretion radius can only be along a radial line from the sink particle to the SPH particle. An equal and opposite force is applied to the sink

particle to conserve linear momentum.

Finally, the viscosity boundary conditions must be considered. Standard SPH artificial viscosity implementation incorporates two kinds of viscosity: a bulk viscosity and a shear viscosity component (Meglicki, Wickramasinghe and Bicknell, 1993). Bulk viscosity is contained as a term in Equation 2.31 but shear viscosity arises due to the interaction of particles with each other across a shear flow over a finite distance of the order of h. Technically, in the limit where the simulation becomes continuous ($h \to 0$), this shear viscosity ceases to exist. The viscosity boundaries must be accounted for or the angular momentum transport is much greater than it should be. Any particle near the accretion boundary should be gaining angular momentum (through viscosity) from particles closer to the sink particle and transferring it to particles further out. The inner particles become depleted due to the accretion radius and no longer supply angular momentum to particles in the disc. To solve this, the components of acceleration due to viscosity in two directions are calculated: the component tangential to the accretion radius and the component in the direction the SPH particle is travelling. These components are calculated using the corrected viscous accelerations from the previous time step. An estimate for the acceleration of the particle is then calculated using the mean of the neighbours' accelerations further away from the sink particle. The value of the correction is the difference between this estimate and the values of viscous acceleration calculated for the current timestep using SPH methods. Again, an equal and opposite force is applied to the sink particle to conserve momentum.

However, a constraint must be added for this boundary correction to viscosity. The net correction to acceleration cannot be in the direction of motion for the particle. Without this constraint, the particle may gain angular momentum and transfer it to the neighbouring particles further out in the disc. This then increases the estimations of the viscous acceleration due to those partners which further increases the angular momentum of the original particle.

All these corrections are gradually applied as the SPH particle approaches the sink particle. There are multiplied by smoothly varying functions varying from 0 to 1. This function has a different dependence on the distance from the sink particle for each corrected property. This dependence is determined by the length-scales over which the property becomes important in the summation of neighbouring particles.

Chapter 3

SPH Code Implemetation

The code was originally developed by W. Benz (Benz, 1990; Benz et al., 1990) with minor modifications made by I. A. Bonnell starting from the principles developed by Lucy (1977) and Gingold and Monaghan (1977). M. Bate received the code and used it to model the formation of multiple protostar systems (Bate et al, 1995). A. T. Okazaki then acquired the code from M. Bate and implemented the VDD model (see Section 1.2.4), thus allowing the code to simulate Be/X-ray binaries (Okazaki et al., 2002; Hayasaki and Okazaki, 2004). The code is a three-dimensional SPH (see Chapter 2) FORTRAN program that employs the parallelisation software, OpenMP.

3.1 Properties of the disc model

The Be star's decretion disc is modelled by an ensemble of particles of equal mass. Unless specified otherwise, the mass of every particle is $\sim 10^{-15}\mathrm{M}_{\odot}$. The temperature profile of the disc is complex in nature but requires an equally complex radiative transfer code to correctly model (see Section 1.2.4). Hence, the model disc is assumed to be isothermal with a temperature of $T = 0.6T_{eff}$ which has been found to be a largely acceptable approximation (Poeckert and Marlborough, 1982; van Kerkwijk et al., 1995; Carciofi and Bjorkman, 2006). In reality, the inner region ($\sim 5 - 10R_{\odot}$) of an isolated Be star's disc has a rather complex temperature profile and only outside of this is the disc close to isothermal (see Figure 1.3). When the Be star is coupled with a compact object in a Be/X-ray binary the disc is far more dynamic and the temperature profile of the disc will be further complicated. Despite the fact that detailed mechanics of the disc could be affected by the isothermal simplification, the largest problem with the assumption is that any emission from the disc is difficult to model accurately. In the work in this thesis, any disc emission is calculated through relative disc size or the Horne and Marsh method for computing line profiles (see Section 1.2.5).

The particles are injected into the disc with Keplerian velocity at a random azimuthal angle at 1.05 stellar radii from the centre of the Be star. They are placed at a random small distance from the equatorial plane that lies between $\pm 0.03 R_*$. Both the Be star and the neutron star are modelled using sink particles (see Section 2.3).

The most important aspect of the code is its ability to reproduce the properties of the Be star's circumstellar disc. This section will consider the state of the disc produced in the simulations, showing the code's capability. See Chapter 1 for the properties of the disc inferred from observations and theoretical calculations. The simulations shown in this chapter contain a Be star of radius $M = 18 M_\odot$ and mass $R = 7 R_\odot$ to target a B0 star (Schmidt-Kaler, 1982).

It should be noted that the presence of an accretion disc that surrounds the compact object is neglected in this model. Hence, all accretion onto the neutron star or black hole is determined simply by the particles that fall into the radius of the neutron star. A compact object with a given rate of mass capture may well have a very different accretion rate due to the creation of a surrounding disc. Radiation pressure is also neglected in the model because aside from extreme cases (see Section 5.5.1) the distances over which the radiation pressure interacts with the disc are much smaller than the size of the disc.

This model also does not take into account the radiation pressure from the emitting compact object. The pressure caused by the emitted photons can also affect the rate at which matter is accreted onto the compact object. It can also affect the surrounding circumstellar material, should the compact object be moving through the disc. However, as the scale of the Be star's circumstellar disc is so large, radiation pressure effects from the compact object may be small.

3.1.1 Density profile

Each SPH particle has an associated density that is calculated from nearby particles (see Chapter 2) and this associated density should be related directly to the spacing and mass of the simulation particles. Figure 3.1 shows a comparison between two methods of calculating disc density for an isolated Be system. The first of these is the value of density assigned to each simulation particle and is shown by the blue data points. The second method (shown by the red line) is the calculation of the average density of annular rings at successive radial points in the disc. It is calculated as follows

$$\rho_{\text{approx}} = \frac{n_{\text{p}} m_{\text{p}}}{\pi (r_2^2 - r_1^2) z}, \tag{3.1}$$

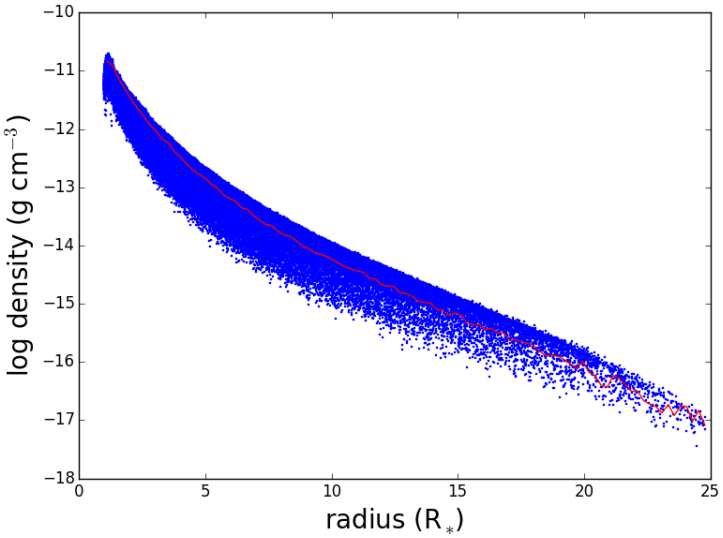

Figure 3.1: The relationship between the logarithm of the density of the decretion disc and radius for a simulated and isolated Be star. The blue scatter points show the density value associated with each SPH particle in the disc. The red line shows the average density at annular rings using Equation 3.2.

where $n_{\rm p}$ is the number of particles, $m_{\rm p}$ is the mass of the particles, z is the full height of the disc and r_1 and r_2 are two radial points that define the annular ring in the disc. These two methods are shown to be virtually identical but the red line behaves sporadically at large radii due to a decreasing number of SPH particles.

The density profile of the Be star's disc is expected to be a radial power law and a vertical Gaussian. The power law index should lie between 1.5 and 4 (Silaj et al., 2010) and the base gas density, should lie between $10^{-12}\mathrm{g\,cm^{-3}} \sim 10^{-10}\mathrm{g\,cm^{-3}}$ (Carciofi et al., 2006, 2007, 2009; Tycner et al., 2008; Jones, Sigut and Porter, 2008a). Figure 3.2 demonstrates the power law density profile of the disc with a linear fit shown by the red line. The equation of the fit is given by

$$\log \rho = -3.15 \times \log R - 10.6 \tag{3.2}$$

where ρ is the density of the disc in $\mathrm{g\,cm^{-3}}$ and R is the radius from the Be star in stellar radii. Both the base gas density and the power law index lie within expected values. Using a least squares fitting method and the model for the density profile in Touhami, Gies and Schaefer (2011), the power law index is 3.5. However, the curve shown in Figure 3.2 is clearly a broken power law with the density in the outer regions of the disc dropping off more rapidly. Figure 3.3 shows the vertical density profile of the Be star's disc at three different radii. All three curves show a Gaussian relation with the maximum of the curve decreasing with radius.

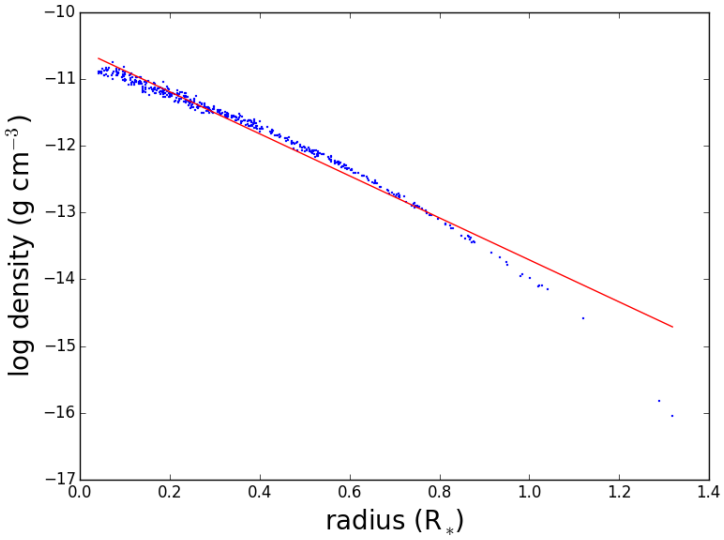

Figure 3.2: The relationship between the logarithm of the disc's density and the logarithm of the disc's radius for an isolated Be star. The blue scatter points show the density associated with SPH particles that lie within a short distance of the equatorial plane of the Be star. The red line shows a linear fit to the data using a simple polynomial fit routine. The gradient and y-intercept for the fit is given by Equation 3.1.

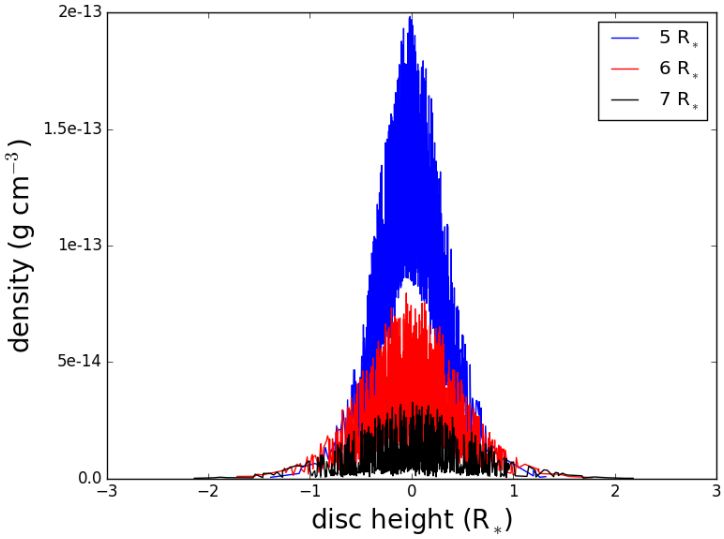

Figure 3.3: The relationship between the density of the disc and the vertical distance from the equatorial plane of the isolated Be star. The different colours show the relationship for three different radii.

3.1.2 Keplerian motion

Another confirmed characteristic of the Be star's disc is the Keplerian motion of the disc material. Figure 3.4 shows the speed of the particles in the disc in three different cases. The first panel is for an isolated Be star and the motion of the particles is shown to be Keplerian. The second and third plot in Figure 3.4 show the distribution of speeds for particles in a Be/NS system, when the neutron star is at apastron and periastron, respectively. When the neutron star is at apastron, the disc is still Keplerian. The spread of speeds is larger than the isolated Be star's disc and the disc is smaller due to the neutron star's truncation (see Section 1.3.4). The final panel in Figure 3.4 reveals the complex behaviour of the disc just after periastron. Many particles in the disc are either sped up or slowed down and there are three distinct groupings of speed in the outer regions of the disc. This is due to the spiral structure that is excited in the disc by the neutron star's passage and will be discussed further in Section 3.2.

3.1.3 Disc flare

The final key property of the disc is flaring, i.e. the disc growing in vertical height with radius. Figure 3.5 shows how the height of the disc increases with radius. The variations in the curve increase with radius because the number of particles and, in turn, the resolution of the disc decreases with radius. The opening angle of the disc from the equatorial plane is found to be $\sim 9^\circ$ and thus, is in keeping with the suggestion that Be stars possess a small opening angle (Quirrenbach et al., 1997).

3.2 Velocity profiles

Initial work with the code aimed to produce structures in the disc that can explain Hα variations seen in observations. This work was performed without using radiative transfer methods and so only the velocity profiles of the disc can be analysed. For all the line profiles presented, the velocities of the SPH particles along the assumed line of sight are used to calculate the Doppler-shifted wavelength. These are then separated into arbitrary wavelength bins and hence the counts are only relative.

During the course of producing simulations for various binary Be/NS systems, a spiral structure in the disc was observed, as mentioned in Okazaki et al. (2002). Figure 3.6 shows the spiral structure that forms at the neutron star's closest approach. One spiral arm tracks the compact object and another arm is induced on the opposite side of the disc. In a circular orbit, a single spiral arm tracks the

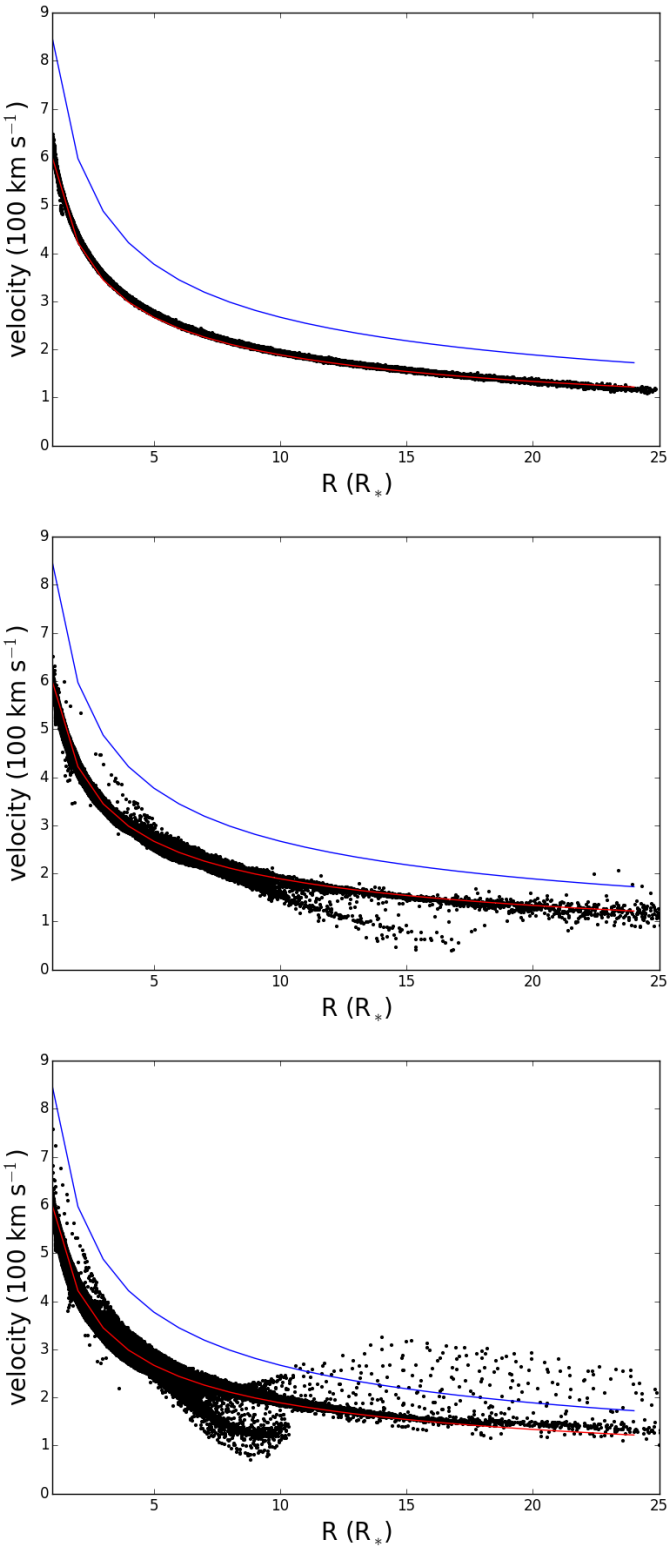

Figure 3.4: The speed of the particles in the disc with radius from the Be star for three different cases. The upper blue line and lower red line show the escape velocity and Keplerian velocity with radius, respectively. Top: An isolated Be star. Middle: A Be/NS binary with a binary period of $P_{\rm orb} = 40$ days and an eccentricity of $e = 0.4$. The neutron star is positioned at apastron. Bottom: The same as the middle plot but the neutron star is at a position just after periastron.

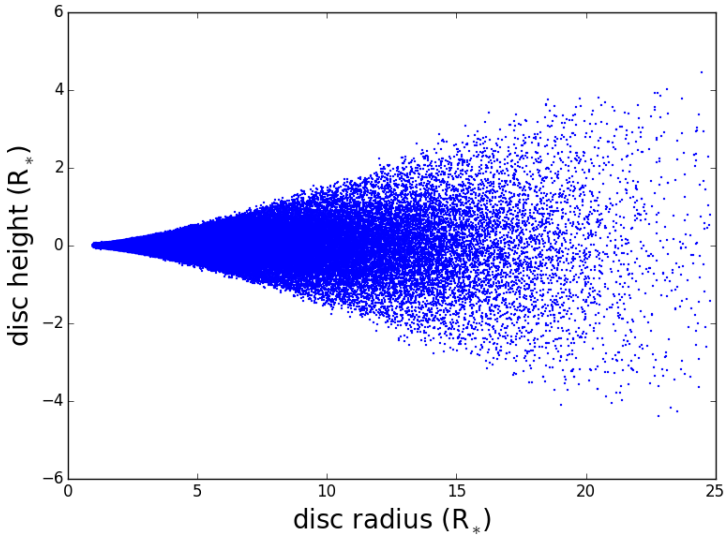

Figure 3.5: The relationship between the height of the disc and radius for the isolated Be star. The scatter points show the radial positions and heights of every SPH particle.

neutron star constantly. After being excited at periastron, this structure dissipates during the remainder of the orbit.

This spiral initially follows the pattern of a logarithmic spiral which is appropriately the most common to occur in natural systems. A logarithmic spiral varies as $r = ae^{b\theta}$. However, after a maximum of 180°, this structure no longer follows such a pattern and the decrease in radius with angle slows. The fact that the spirals do not follow this pattern exactly could be due to the Keplerian motion or continuous interaction of the neutron star with the disc.

It is clear that this spiral pattern creates visible changes in the velocity profile: the bottom right plot shows two additional peaks. If any observations show similar peaks, this would confirm that the interaction of the neutron star with the disc at periastron is accurate. However, with the current resolution in line emission observations, it may well be very difficult to resolve such small features. The feature may also be less pronounced in the emission of a Be star disc and should be investigated using radiative transfer methods.

3.3 Speed-up

Modelling the dynamics of the Be star's circumstellar disc using a three-dimensional SPH code requires a considerable amount of computational resources. It is therefore important to consider how to most efficiently run simulations to complete the maximum amount of work possible. This is one of the reasons that OpenMP is implemented within the code, as it can greatly reduce the amount of required time for a single simulation.

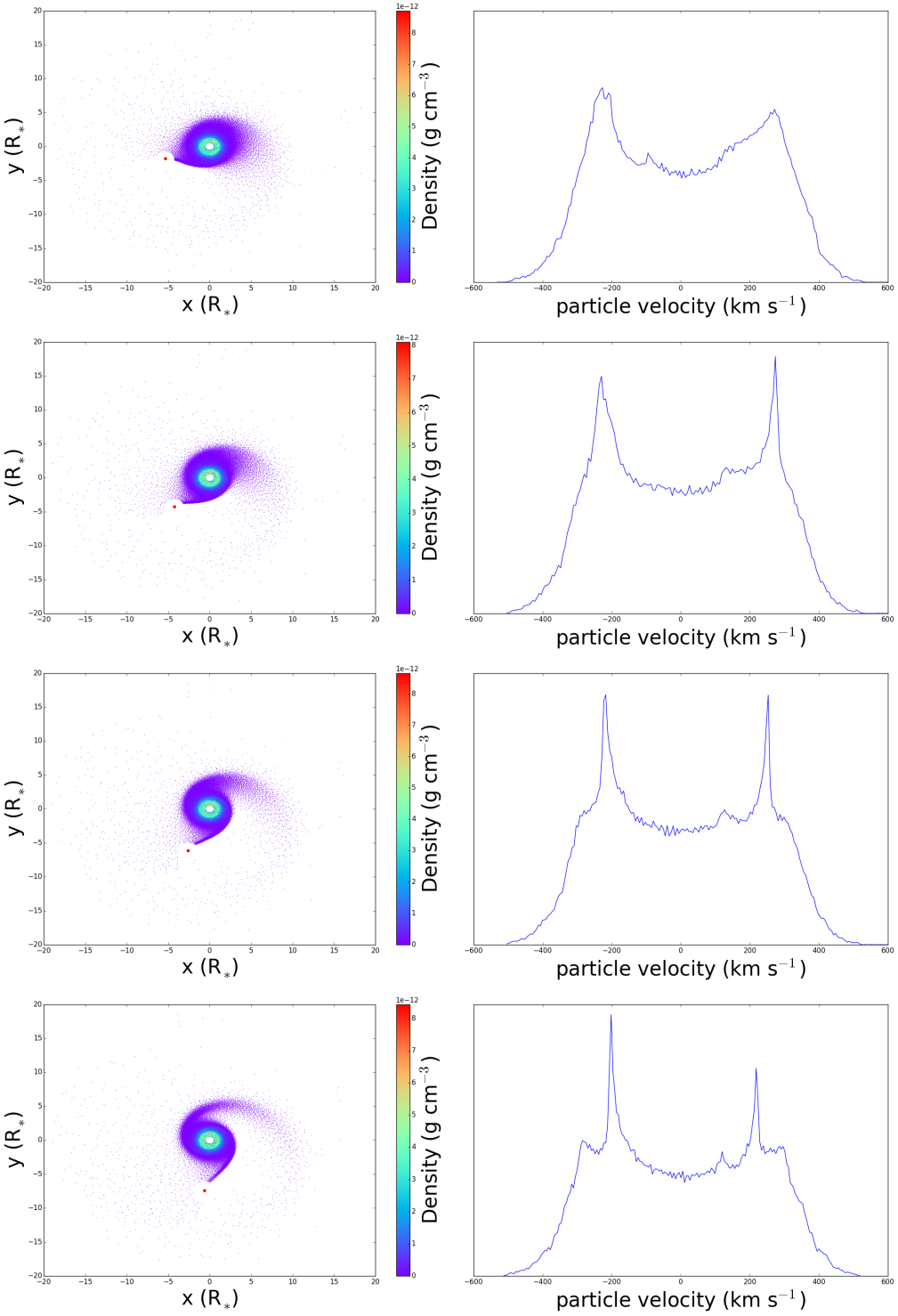

Figure 3.6: Four plots of a Be/NS system at successive points in time. The binary has an orbital period of $P_{\rm orb} = 40$ days and an eccentricity of $e = 0.4$. The neutron star is shown by the red point and the Be star is represented by white space inside the disc. The left panels in each plot show snapshots of the system from above. The right panels show the wavelength, Doppler-shifted from the Hα rest wavelength, 6562.8Å. Doppler shifts are calculated using the velocities of the disc when it is viewed at an inclination of 45°. The y scale for the right panels is arbitrary.

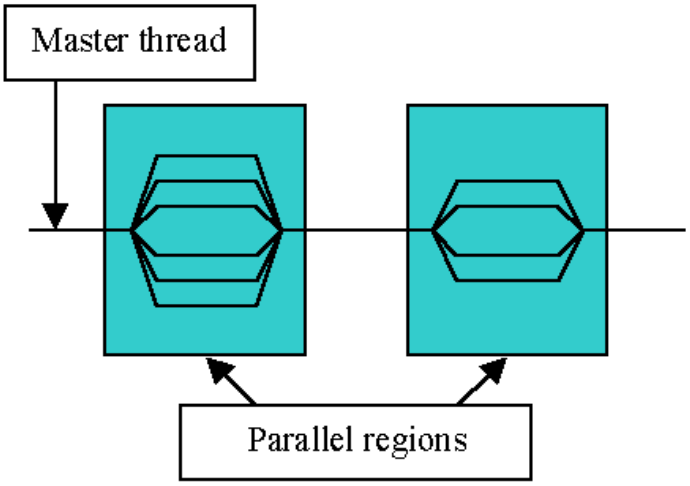

Figure 3.7: Illustration of the process of multi-threading. In the image, there are three serial sections of code, separated by two parallel sections with a differing number of threads. Source: https://www.dartmouth.edu/∼rc/classes/intro_openmp/.

OpenMP is a multi-threading software which means that sections of the program can be distributed across a number of processors in multiple threads (see Figure 3.7). This method requires shared memory between any processors used. The application of multi-threading to a program can be straightforward but it requires caution. One cannot reliably expect the processors to run at the same speed, nor identically every time the code runs. Hence, one thread may interact with the simulation variables at the same time as another thread. This causes inconsistencies and yields incorrect results. One must therefore make sure to separate the sections of the code correctly into parallel and serial sections, so that no errors occur. The code used in this thesis has been tested extensively to make sure that no errors are caused by the parallelisation. This testing consisted of checking vital parts of the code, making sure that the code produced the same results when given identical parameters and reproducing results from previous work including Okazaki et al. (2002) (including the results shown in this chapter).

The "speed up", S, of a program is a measure of the improvement of its runtime with the number of processors used and is given by the following

$$S(N) = \frac{T_N}{T_1}, \tag{3.3}$$

where T_1 is the time for the code to run on one processor and T_N is the time for the code to run on N processors. The case where $S(N)$ is equal to N is called ideal speed-up. Typically, only parts of a code can be parallelised and hence the speed-up is rarely ideal. It is actually possible to achieve a greater than ideal case depending on the parallelisation method and the architecture of the code. For all parallel

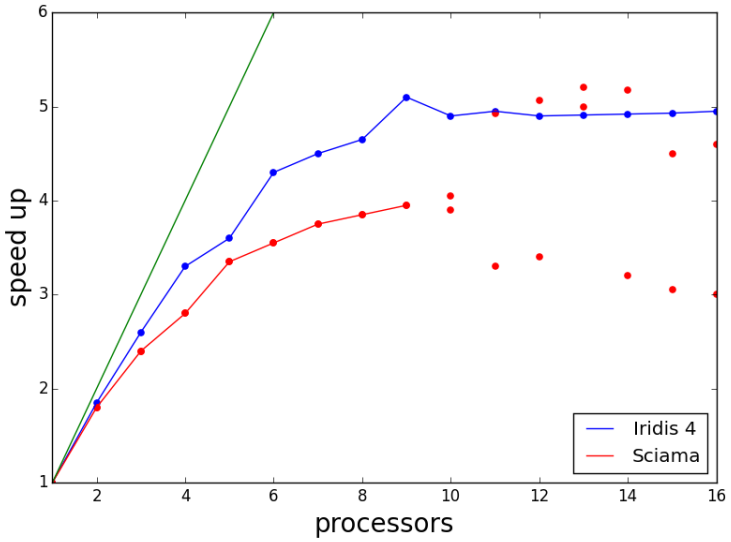

Figure 3.8: The speed-up of Iridis 4 and the Sciama Cluster with increasing number of processors. The solid green line shows the ideal speed-up, i.e $y = x$.

codes, there is always a number of processors after which no speed-up is gained. This can occur for a number of reasons but is most commonly due to the serial aspects of the code becoming much more computationally expensive than the multi-threaded parallel sections.

For the work in this thesis, two computing clusters were used for simulations: Southampton University's Iridis 4 and Portsmouth Institute of Cosmology and Gravitation's (ICG) Sciama Cluster. Due to OpenMP's requirement of shared memory, speed-up can only be tested for a maximum number of processors equal to those available on a single node.

Iridis 4 was, according to the November 2012 TOP500 Supercomputers issue (`http://www.top500.org/list/2012/11/100/`), the most powerful academic supercomputer in the UK and one of the top 30 academic computational facilities in the World. It has 2.6GHz on every core and has 12320 cores overall in the cluster. Iridis 4 has 16 cores per node and thus the code can use up to that many cores for parallelisation. The Sciama Cluster is a supercomputer dedicated mainly to astrophysical computation and is run by the Institute of Cosmology and Gravitation. It also has cores with a speed of 2.6GHz, has 2742 cores overall in the cluster and similarly has a maximum of 16 cores per node.

As the code runs indefinitely, a specific stage in the evolution of the program must be defined as an end point. Thus, the code is run for 10 hours on one processor and the resultant state of the disc is used to benchmark all further simulations. It should be noted that randomness does exist within the code: the particles are injected at random vertical distances from the equatorial plane of the disc (see Section 3.1).

The speed-up of the code when using Iridis 4 and Sciama are shown in Figure 3.8,

with a line along $y = x$ that illustrates ideal speed-up. Iridis 4 shows an impressive improvement in the runtime of the code, up to a maximum of ~ 5 at 8 processors. Any further increase in the number of processors does not improve the speed-up. Sciama behaves similarly, with a slightly smaller speed-up, but continues to change after 9 processors. After this point, the speed-up behaves erratically and no one specific value is found for the runtime of the code. This is likely due to the usage of the processors on each node: if a processor involved in running the simulation is used by another project, they will both be slowed. From these results, 8 processors is the optimal number to use. An additional reason to use 8 processors is that each node has 16 cores and hence, two jobs can fit on one, reducing queue times.

Chapter 4

Decretion discs in Be/X-ray binaries

Coe and Kirk (2015) (hereafter referred to as CK15) investigated a sample of approximately 70 X-ray emitting binary systems containing a Be star in the Small Magellanic Cloud (SMC). All these Be/X-ray binaries show clear X-ray pulse signatures from a neutron star. In the paper, they list all the known orbital periods, eccentricities and neutron star spin periods. Also included is the Be star's spectral type, the size of the circumstellar disc and evidence for non-radial pulsations. The relationship between orbital period and circumstellar disc size seen in galactic sources (Reig, Fabregat and Coe, 1997) is shown to be clearly present in the SMC systems. Figures 8 and 10 in CK15 show two correlations that will be investigated in Section 4.5.

In this chapter, simulations are used to probe fundamental characteristics of Be/NS binaries. In Section 6.2, the methods used to model Be/NS binaries are discussed. Sections 4.2, 4.3 and 4.4 detail the investigations into the disc's base gas density, the disc's size and the neutron star's accretion rate, respectively. The relationships between the disc's characteristics (the base gas density, the accretion rate of the neutron star companion and the disc's size) and the simulation parameters (the viscosity, the mass ejection rate of the Be star, the orientation of the disc, the orbital period and eccentricity) are presented. In Section 4.5 the simulations are used to test the relationships shown in Figures 8 and 10 of CK15. Section 6.4 discusses the results shown in the chapter and compares the findings to previous works.

4.1 Simulations

For the simulations in this chapter, the Be star mass and radius are assumed to be $18M_{\odot}$ and $7R_{\odot}$, respectively, to target a B0V star (Schmidt-Kaler, 1982; Cox, 2000). A mass of $1.4M_{\odot}$ and radius of 10km is adopted for the neutron star. For further details on the implementation of the code, see Section 3.1.

There are a number of simulation parameters that are varied individually to explore the aforementioned characteristics of Be/NS binaries. These include the inclination of the disc to the orbital plane, the mass ejection rate of the Be star, the viscosity of the disc, the binary period and the orbital eccentricity. The behaviour and structure of the disc is dependent on all these parameters. Rímulo et al. (2018) found that the viscosity parameter in the discs of Be stars could be anywhere from a few tenths to more than one. Ghoreyshi et al. (2018) similarly used viscosity parameters from $\alpha = 0.1$ to $\alpha = 1$ to model the Be star ω CMa. Hence, the viscosity explored here is in the range $0.1 \leq \alpha \leq 1.5$. The mass ejection rate of the Be star is varied from 10^{-11} to $10^{-5} M_{\odot} yr^{-1}$ to encompass the large mass ejection rates used by Ghoreyshi et al. (2018) and to include ejection rates inside the range suggested by Vieira et al. (2015). The sample of Be/NS binaries used by CK15 possess orbital periods of up to ~ 500 days. The orbital period of the simulations is varied from 40 days to 400 days in steps of 40 days with the aim to broadly cover this range. Although many interesting systems have orbital periods of less than 40 days, the aim of this chapter is to perform a general examination of the properties of the Be star's decretion disc and extending the simulations to lower orbital periods would not contribute much to this. A more specific investigation of systems at low orbital periods could produce some interesting results and would be a good continuation of the work in this chapter. Eccentricity is tested at $e = 0.0, 0.2, 0.4$ and 0.6 for the systems of varying orbital period and $e = 0.0, 0.2$ and 0.4 when varying disc orientation (see Section 4.1.1). For the simulations where the viscosity of the disc and the mass ejection rate of the Be star are varied, the eccentricity is only tested at $e = 0.0$ and 0.4. This range is chosen because over 90% of Be/NS binaries of known eccentricity have $e \leq 0.6$ (Brown et al., 2018).

When the viscosity and mass ejection rate are not specified, these two quantities are assumed to be $\alpha = 0.63$ and $\dot{M} = 10^{-10}$ $M_{\odot} yr^{-1}$, respectively. These are typical values for observable Be stars as determined through simulations by Rímulo et al. (2018). When the period of the simulation is unspecified, an orbital period of 40 days is assumed. This is because the majority of the systems in the observational sample contained in CK15 have orbital periods of $P_{\rm orb} \leq 150$ days. Given the masses of the Be star and neutron star, the semi-major axis of these systems is ~ 19 stellar radii. The Be star's disc lies in the orbital plane unless it is stated otherwise.

The simulations in this chapter are all considered in a steady state (see Section 3.1)

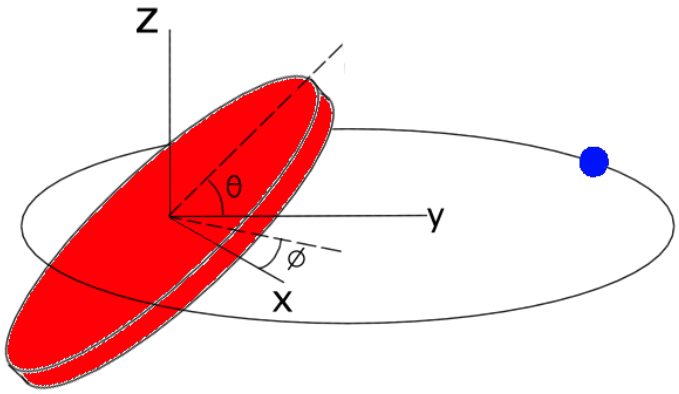

Figure 4.1: An illustration of the geometry used in this chapter. The Be star's circumstellar disc is shown in red and the neutron star is represented by the solid blue circle. The orbit of the neutron star is in the x-y plane. The two angles, θ and ϕ, show the inclination and azimuthal angles, respectively. The inclination and azimuthal angle are defined as the rotation about the x axis and z axis, respectively. Periastron and apastron both lie along the y axis.

because it allows for the best comparison of Be/X-ray binaries across the parameters investigated. However, few Be/X-ray binaries exist in a steady state due to the dynamic nature of the Be star and hence, observable systems cannot be compared to each other so simply. The maximum X-ray luminosity for an observable system is most likely to occur when the disc is not in a steady state and hence the values for luminosity here are best considered as relative.

4.1.1 Misaligned discs

There is a subset of the simulations shown in this chapter that investigate the effect of changing the orientation of the disc relative to the orbital plane. The disc inclination is investigated because there are a number of Be/X-ray binary systems that have had notable observational features that are thought to arise due to large misalignments between the disc and the orbital plane. Examples of these include GX 304-1 (Postnov et al., 2014) and SXP 5.05 (Coe et al., 2015; Brown et al., 2019). Asymmetric supernova explosions can leave the Be star with a disc that is misaligned to the orbital plane (see Section 1.3.5). Figure 4.1 demonstrates the definition of the two orientation angles in this chapter, inclination angle, θ, and azimuthal angle, ϕ. A disc at an inclination angle of 0° lies in the orbital plane and the azimuthal rotation is arbitrary. The x-y plane in the diagram is identical to the orbital plane.

When the circumstellar disc of a Be star is highly misaligned to the orbital plane, the three-body phenomenon known as the Kozai-Lidov mechanism becomes important (Kozai, 1962; Lidov, 1962; Martin et al., 2014). This mechanism causes

Table 4.1: Average disc eccentricities for some of the simulations with discs misaligned to the orbital plane.

orbital e	initial inclination angle (°) [1]	mean disc e
0.0	0	0.11
0.0	30	0.15
0.0	60	0.29
0.0	90	0.34
0.2	0	0.15
0.2	30	0.19
0.2	60	0.32
0.2	90	0.43
0.4	0	0.17
0.4	30	0.22
0.4	60	0.36
0.4	90	0.44

the disc's misalignment to oscillate, trading its inclination for an increase in the eccentricity of the disc. The period of Kozai-Lidov cycles for a particle orbiting the primary of a binary, as derived by Kiseleva et al. (1998), is given by Equation 1.14. All the simulations in this chapter that contain a misaligned disc have the same orbital period and thus have an identical Kozai-Lidov period for the same eccentricity.

Table 4.1 shows the average disc eccentricity of twelve simulations with different disc inclinations and orbital eccentricities. The initial inclination angle is the angle between the equatorial plane of the Be star (the same plane that the disc material is ejected into) and the orbital plane. Disc eccentricity shown is averaged over the final five orbits of the simulation. The simulations have been run for similar times and thus, all the systems of equal eccentricity are at the same approximate point in the Kozai-Lidov cycle. Up until the time the simulations have been evolved, the average disc eccentricity is greater for systems with larger initial misalignments between the disc and the orbital plane. This is expected as the systems with a larger initial inclination angle are capable of achieving larger disc eccentricities. When orbital eccentricity is increased, the Kozai-Lidov period is decreased (see Equation 1.21) meaning that the simulation ends at a later stage of the Kozai-Lidov cycle and hence the modelled disc is, on average, more eccentric. The disc is not completely circular even in binaries with a coplanar disc because of the interaction of the neutron star with the disc. The inclination of the disc does not oscillate in coplanar systems.

[1] Initial inclination angle refers to the angle at which the disc material is injected at, and is not the current inclination of the disc.

4.2 Base gas density

The unperturbed density profile of a Be star's circumstellar disc can be described by a Gaussian-modified power law (Touhami, Gies and Schaefer, 2011; Rivinius, Carciofi and Martayan, 2013). The density at the surface of the Be star, i.e. base of the circumstellar decretion disc, is defined as the base gas density. For the simulations discussed in this chapter, base gas density is determined by the mean density of an equatorial ring of simulation particles at the Be star's surface, averaged over five orbits.

Figure 4.2 shows that the base gas density decreases exponentially with viscosity. The viscosity of the disc matter leads to the transfer of angular momentum, i.e. matter travels outwards due to the angular momentum gained from the particles falling back onto the star. Hence, as viscous forces are diffusive, a larger viscosity leads to a lower base gas density. The base gas density varies by a factor of ~ 10 due to viscosity.

Base gas density increases linearly with the Be star's mass ejection rate as demonstrated by Figure 4.3. The base gas density at equilibrium arises from the balance between the amount of material being ejected into the disc and the matter falling back onto the Be star. Therefore, the base gas density of the disc is heavily dependent on the mass ejection rate, varying by ~ 4 orders of magnitude over the range shown.

Base gas density is not related to orbital period, eccentricity or the orientation of the disc. These quantities only alter the neutron star's interaction with the disc and thus do not affect the innermost regions.

4.3 Disc size

Observations have shown that the circumstellar discs of Be stars can be up to hundreds of stellar radii in size (Dougherty and Taylor, 1992). The size of the circumstellar disc in Be/X-ray binaries is dependent on the tidal truncation caused by the binary partner (Okazaki et al., 2002). In equilibrium, the disc is limited to a radius where the tidal forces balance the viscous forces that is defined as the truncation radius. In this chapter, the size of the Be star's circumstellar disc is defined as the radius that contains 90% of the simulation particles. Note that this definition means that the size of an eccentric disc will be defined by its semi-major axis. Minimum and maximum disc sizes are calculated for individual orbits and then averaged over five orbits. In all plots in this section, solid lines and dashed lines represent the maximum and minimum values of disc size, respectively.

Figure 4.4 shows the variation of the Be star's disc size with viscosity. Minimum

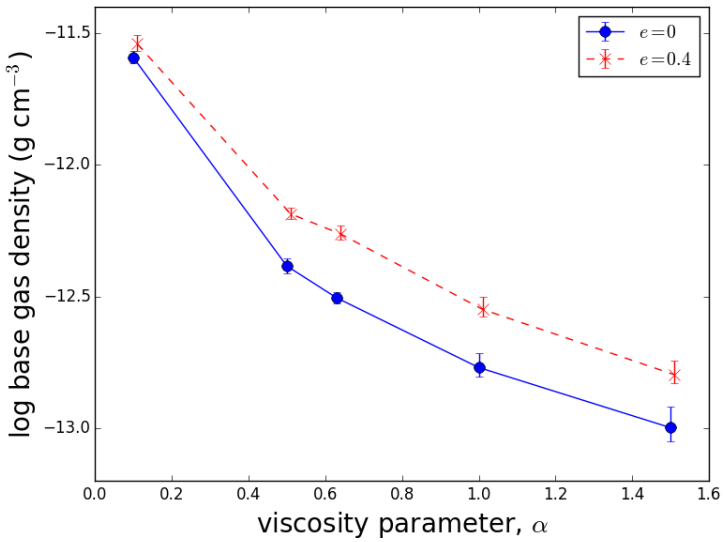

Figure 4.2: The relationship between the base gas density and the viscosity parameter of the disc. The bars show the minimum and maximum values of the base gas density around an orbital cycle. The bars are comparable to or smaller than the size of the symbols. This is for systems with a 40 day period and eccentricities of $e = 0$ and 0.4.

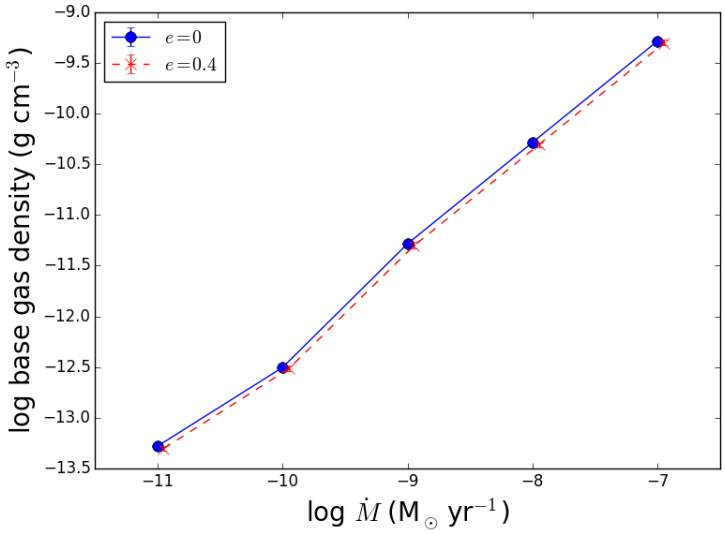

Figure 4.3: The relationship between the base gas density and the mass ejection rate of the Be star. The bars show the minimum and maximum values of the base gas density around an orbital cycle. The bars are comparable to or smaller than the size of the symbols. This is for systems with a 40 day period and eccentricities of $e = 0$ and 0.4.

and maximum disc size both increase with viscosity for all eccentricities. Both the rate that disc size increases and the range from minimum to maximum are larger for higher eccentricities. For the viscosity parameters shown, the disc size increases by $\sim 60\%$.

Figure 4.5 shows the relationship between the disc's size and its orientation. Simulations were performed whilst varying both the inclination angle, θ and the azimuthal angle, ϕ. Disc size increases with the inclination to the orbital plane and at $e = 0.4$; the disc is $\sim 40\%$ larger when the disc is perpendicular to the orbital plane than when it is coplanar. For $e = 0.0$ and $e = 0.2$, the azimuthal angle has negligible effect on the size of the disc and hence the top panel of Figure 4.5 shows the minimum and maximum values of disc size for simulations of any azimuthal angle at each eccentricity. There is a relationship with azimuthal angle at higher eccentricities, as shown by the bottom panel of Figure 4.5. The disc is at its largest at $\phi = 90°$, where the disc is perpendicular to the plane of the orbit but parallel to the semi-major axis. This is where the disc has minimum interaction with the neutron star, i.e. the neutron star passes close to the disc once at periastron. The disc is smaller when it is both perpendicular to the orbital plane and the semi-major axis ($\phi = 0°$). In this case, the neutron star interacts twice with the Be star's circumstellar disc: once before periastron and once after. Like viscosity, the range from minimum to maximum disc size increases with eccentricity.

Figure 4.6 demonstrates the relationship between the orbital period of the Be/NS binary and the size of the Be star's circumstellar disc. The size of the disc increases by a factor of ~ 7 with orbital period. The periastron distance of the neutron star and, in turn, the truncation radius of the Be star's disc increases with orbital period, allowing for a larger maximum disc radius. The difference between minimum and maximum disc size increases with eccentricity.

Disc size is independent of the mass ejection rate of the Be star. A higher mass ejection rate increases the density of the disc but the radius of the tidal truncation remains the same and therefore so does the size of the disc.

4.4 Neutron star accretion rate

The X-ray emission from Be/NS binaries is a defining feature. The compact object is often only detectable by X-ray telescopes, and thus the X-ray flux is a vital quantity to understand in Be/NS binaries. In this chapter, the neutron star mass capture rate is calculated directly from the number of simulation particles falling onto the neutron star. The accretion rate of the neutron star is assumed to be identical to the mass capture rate. The maximum accretion rate is shown because, unlike the average accretion rate, it is independent of the fraction of the orbit that

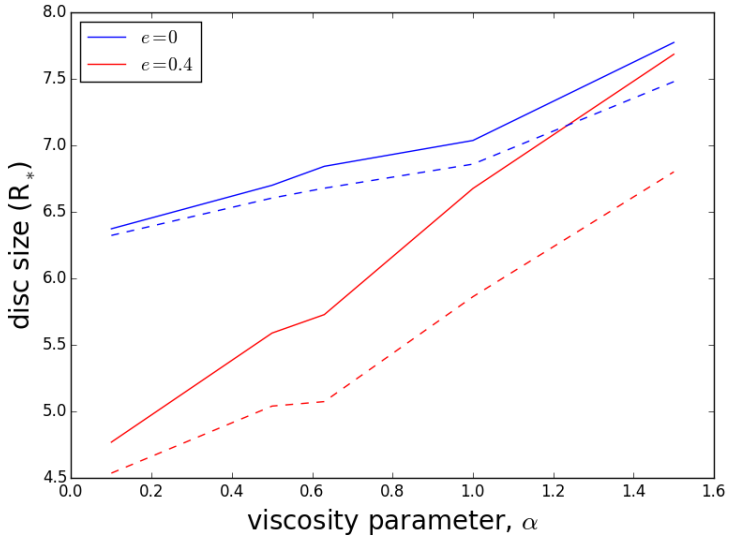

Figure 4.4: The relationship between the time-averaged size of the disc and viscosity parameter for systems with an orbital period of 40 days and eccentricities of $e = 0$ and 0.4. The solid and dashed lines show the maximum and minimum disc sizes, respectively.

the neutron star spends interacting with the Be star's circumstellar disc. Maximum accretion rate is calculated for individual orbits and then the median of five orbits is taken.

The neutron star's accretion rate increases linearly with the mass ejection rate of the Be star. A higher mass ejection rate yields a generally higher density of the disc (see Figure 4.3). When the truncation radius remains the same, the neutron star interacts at the same distance with a higher density disc.

The relationship between the accretion rate of the neutron star and the orbital period of the Be/X-ray binary is shown in Figure 4.7. The periastron distance of the neutron star is dependent on the orbital period and eccentricity of the binary. The density of the disc falls radially as a power law and thus the amount of accreted matter is dependent on the distance from the Be star. Therefore, neutron stars with larger orbital periods accrete less matter and the most eccentric systems have a higher maximum neutron star accretion rate.

The accretion rate of the neutron star has little to no dependency on the viscosity and the orientation of the disc. The orientation of the disc does not greatly alter the neutron star's closest passage to the disc and thus has a small effect on the maximum accretion rate. Larger viscosities both decrease the density of the disc (see Figure 4.2) and increase the size of the disc (see Figure 4.4). This leads to a negligible change in the accretion rate of the neutron star.

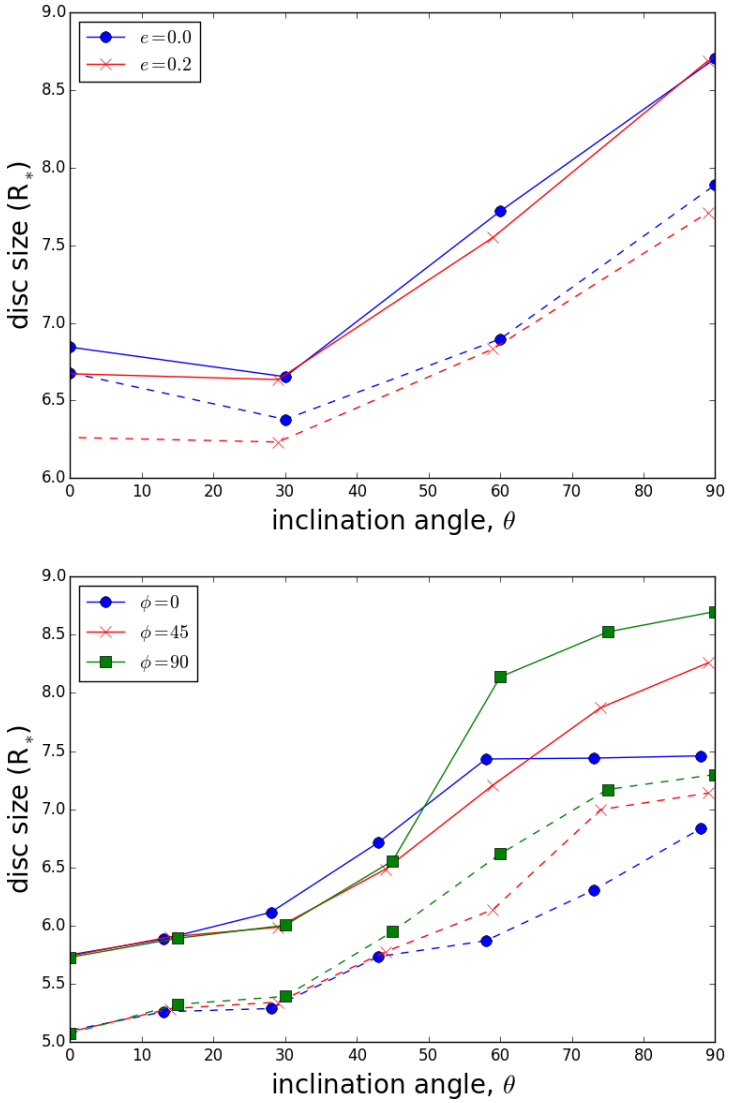

Figure 4.5: Top: Time-averaged size of the disc for various orientations. The systems shown have an orbital period of 40 days and eccentricities of $e = 0.0$ and 0.2. The solid and dashed lines show the maximum and minimum disc sizes, respectively. The values of maximum and minimum disc size are for simulations of any ϕ at each eccentricity. Bottom: Time-averaged size of the disc for various disc orientations. ϕ indicates the azimuthal rotation, i.e. rotation in the plane of the orbit. This is for systems with a 40 day period and 0.4 eccentricity. The solid and dashed lines show the maximum and minimum disc sizes, respectively.

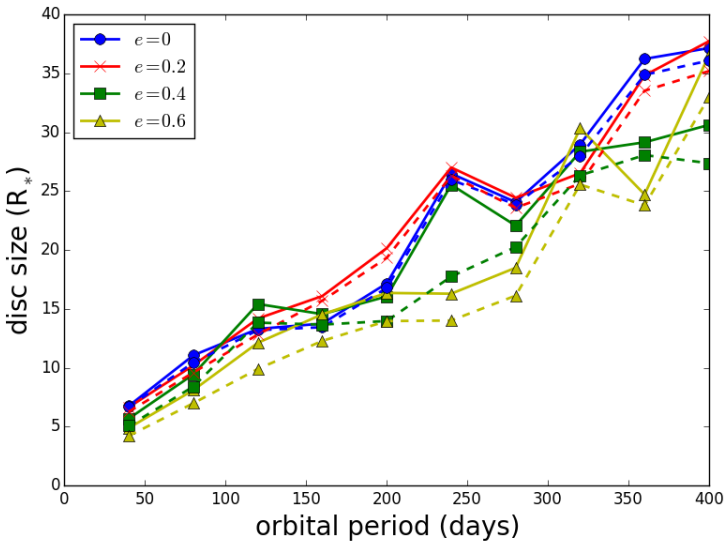

Figure 4.6: The relationship between the time-averaged size of the disc and the orbital parameters of the Be/NS binaries. The data points have a range of eccentricities from $e = 0.0$ to 0.6. The solid and dashed lines show the maximum and minimum disc sizes, respectively.

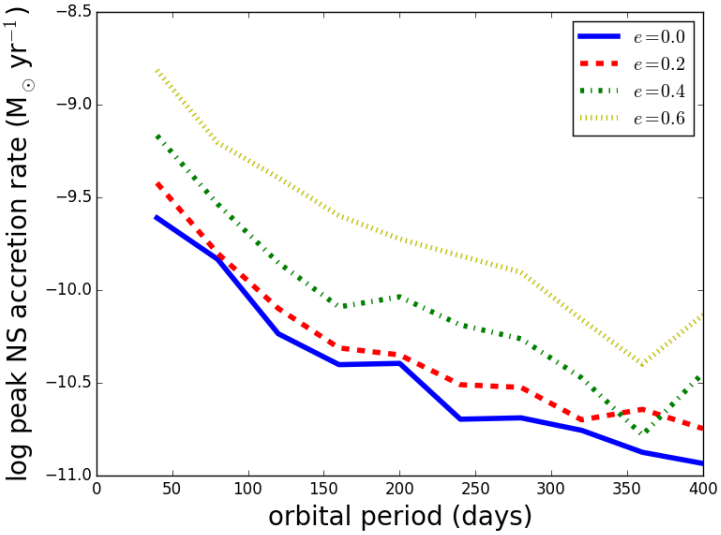

Figure 4.7: The relationship between the maximum accretion rate of the neutron star and the orbital period.

Table 4.2: The gradients and y-intercepts for the linear fits shown in Figure 4.8. The three samples refer to the simulation data, the observational data with orbital periods of less than 150 days and the entire set of observational data. The data for the observed binaries is taken from CK15.

sample	gradient	y-intercept (days)
simulations	0.51	20.99
binaries with $P_{\rm orb} \leq 150$ days	0.51	88.90
complete observational sample	0.27	107.70

4.5 Comparison to observations

CK15 presented two relationships involving the size of the Be star's circumstellar disc in Be/X-ray binaries (see Figures 8 and 10 in their paper). The first is a relationship between the Hα equivalent width and the orbital period. They show two linear fits that utilise the sample of Be/NS binaries contained in the paper. One is a fit to the systems that possess an orbital period of $P_{\rm orb} \leq 150$ days and the other is a fit to the entire observational sample. The former linear fit has a much larger gradient than the latter (see Table 4.2). The second relationship they describe is a quadratic relationship between the semi-major axis of the binary and the size of the disc. The disc size is determined using the following equation found in Hanuschik (1989):

$$log\left(\sqrt{\frac{R_{\rm OB}}{R_{\rm cs}}}\right) = [-0.32 \times log(-EW)] - 0.2, \tag{4.1}$$

where $R_{\rm cs}$ is the size of the circumstellar disc, EW is the Hα equivalent width and $R_{\rm OB}$ is the radius of the Be star that is determined from the individual spectral types recorded for each Be star. In this section, these relationships are investigated using simulations with orbital periods ranging from 40 to 400 days and eccentricities of $e = 0.0, 0.2, 0.4$ and 0.6. The linear fits to the simulations, the observational data with $P_{\rm orb} \leq 150$ days and the complete observational dataset will be referred to as $R_{\rm sim}$, R_{150} and $R_{\rm all}$, respectively.

Figure 4.8 shows the relationship between the size of the Be star's circumstellar and orbital period. The data and fits shown in Figure 8 of CK15 are included. The observational disc sizes are converted from the Hα equivalent widths given in CK15 using Equation 4.1. Values for the Be star radii are taken from Schmidt-Kaler (1982). The gradient of $R_{\rm sim}$ is equal to the gradient of R_{150}. However, the y-intercept differs by a factor of ~ 4. Both the gradient and the y-intercept differ considerably between $R_{\rm all}$ and $R_{\rm sim}$.

Figure 4.9 shows the relationship between the semi-major axis and the disc's size.

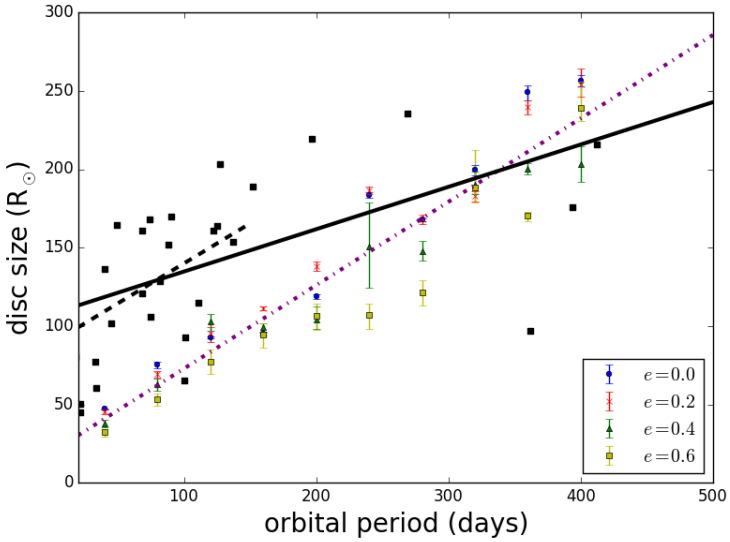

Figure 4.8: The relationship between disc size and orbital period. The black squares show the observational data from CK15. The coloured bars represent the simulation data and have a range of eccentricities from $e = 0.0$ to 0.6. The bars show the maximum and minimum values of disc size. The dot-dashed purple line shows the fit to all the simulation data. The fits from CK15 to systems with $P_{\rm orb} \leq 150$ days (dashed black line) and systems with $P_{\rm orb} \leq 500$ days (solid black line) are included in the plot. The parameters of the fits are described in Table 4.2.

For the simulations, disc size is calculated as described in Section 4.3 and semi-major axis is known from the assumed orbital period of each simulation. CK15 present the following quadratic fit

$$a = (7 \times 10^{-12})R_{\rm cs}^2 + 0.4524R_{\rm cs} + (4.3 \times 10^{10})m. \tag{4.2}$$

where a is the semi-major axis and $R_{\rm cs}$ is the radius of the circumstellar disc in metres. The simulation data agrees with the observational relationship between the disc's size and the semi-major axis of the orbit.

The simulation data in Figures 4.8 and 4.9 have an equal number of binaries at each tested eccentricity ($e = 0.0, 0.2, 0.4$ and 0.6). The sample used by CK15 is missing a large number of the orbital eccentricities and hence there could be an unknown bias. This bias could be the cause of the differences between the observational and predicted relationships shown in this chapter. The differences in the fits could also be related to the fact that there are only a few systems at higher orbital periods.

In Figure 4.8, $R_{\rm sim}$ and R_{150} have the same gradient. This implies that the observed binaries with low orbital periods possess a similar distribution of eccentricities to the simulation data. This is supported by the seven observationally determined eccentricities that are distributed over the range $0 \leq e \leq 0.5$ (see Table

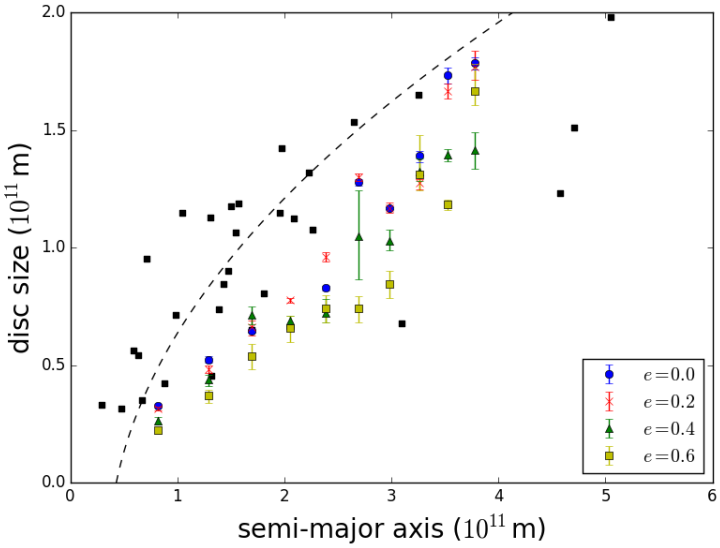

Figure 4.9: The relationship between the Be star's circumstellar disc size and semi-major axis of the neutron star's orbit. The black squares show the observational data from CK15. The coloured bars represent the simulation data and have a range of eccentricities from $e = 0.0$ to 0.6. The bars show the minimum and maximum values of disc size. The quadratic fit from CK15 (dashed black line) is given by Equation 4.2.

4.3). $R_{\rm all}$ has a considerably smaller gradient than $R_{\rm sim}$ and R_{150}. Removing all the simulations with larger orbital periods (i.e. $P_{\rm orb} > 150$ days) that have eccentricities of $e < 0.6$ lowers the gradient of the model fit to 0.41. Hence, the simulations suggest that the eccentricities of the observational sample are higher at larger orbital periods. Figure 4.10 shows that the distribution of eccentricities increases with orbital period for observed Be/X-ray binaries. Despite 80% of the systems having an orbital period of less than 150 days, the only two systems with a confirmed eccentricity greater than 0.6 comprise two of the six binaries of larger orbital period. This supports the suggestion that the systems with higher orbital periods have a larger eccentricity on average.

Of the Be/X-ray binaries with known eccentricities, $\sim 80\%$ have an eccentricity of $e \leq 0.45$ (Brown et al., 2018). CK15 present the eccentricity of seven systems in their sample and all of them are below 0.45 (see Table 4.3). It should be noted that these systems have orbital periods of $P_{\rm orb} < 40$ days. In Figure 4.9, the simulation data lies increasingly far away from the quadratic fit as the eccentricity grows. Therefore, it is suggested that the observational sample is more likely to contain binaries with low eccentricity.

4.6 Discussion and Conclusions

In this chapter, simulations are used to investigate three characteristics (the base gas density of the Be star's circumstellar disc, the accretion rate of the neutron star

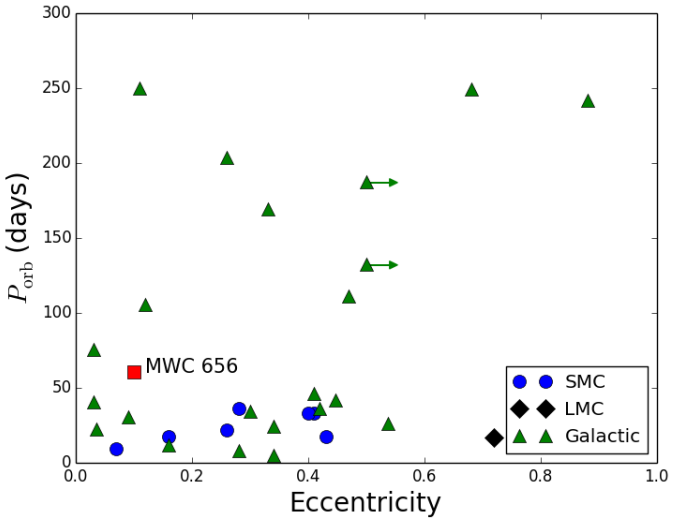

Figure 4.10: The relationship between eccentricity and orbital period for Be/X-ray binaries in the Milky Way, LMC and SMC. The only confirmed Be/BH system, MWC 656, is also included. Arrows demonstrate the lower limit on eccentricity for the 3 systems with $e > 0.5$. The values used for this figure are contained in Brown et al. (2018).

Table 4.3: The orbital period and eccentricity of the seven systems with known eccentricities in the sample contained in CK15.

system	orbital period (days)	eccentricity
SXP 2.37	9.30	0.07 ± 0.02
SXP 5.05	17.20	0.16 ± 0.02
SXP 6.85	22.00	0.26 ± 0.03
SXP 8.80	33.40	0.41 ± 0.04
SXP 11.5	36.30	0.28 ± 0.03
SXP 18.3	17.79	0.43 ± 0.03
SXP 74.7	33.30	0.40 ± 0.23

and the size of the disc) of Be/NS binaries. Five parameters are varied (the viscosity and orientation of the Be star's circumstellar disc, the mass ejection rate of the Be star and the period and eccentricity of the neutron star's orbit) and the effect on the aforementioned characteristics is presented.

The base gas density is both dependent on the mass ejection rate of the Be star and the viscosity of the material in the disc. Using simulations, the density of the inner region of the disc has been shown to drop rapidly when the ejection rate of the Be star is decreased (Haubois et al., 2012). Our simulations also display this dependence of the base gas density on mass ejection rate. When the disc is in a steady state, the base gas density remains in equilibrium due to the balance between the ejection of matter into the disc and the accretion of matter back onto the Be star. Larger viscosities decrease the base gas density of the disc because viscous forces are diffusive. There is little to no dependence of the base gas density on the orientation of the disc or the orbital parameters of the binary. These findings agree with previous work that suggests that the orbital parameters of the binary only affect the truncation of the disc and not the inner regions (Okazaki et al., 2002).

The disc's size in Be/X-ray binaries is limited by tidal truncation that arises from the presence of a compact object. Hence, any properties that affect the interaction between the neutron star and the disc are important - this includes the orbital parameters and the orientation of the disc. Both orbital period and eccentricity vary the periastron distance of the neutron star's orbit and, in turn, increase (or decrease in the case of eccentricity) the size of the disc. The size of the disc increases with misalignment, in agreement with previous work that suggests a smaller tidal torque in binary systems with misaligned discs (Martin et al., 2014). The disc's size increases with viscosity, in agreement with previous work that shows that the truncation radius is the distance where the tidal torque balances the viscous torque (Okazaki et al., 2002). The size of the Be star's disc is not dependent on the mass ejection rate of the Be star as the disc is truncated at the same radius regardless of the density of the disc.

The maximum accretion rate of the neutron star is dependent on the mass ejection rate of the Be star, the orbital period and the orbital eccentricity. The density of the disc at the neutron star's closest passage to the Be star's disc determines the amount of material accreted. Given that the density in the disc falls off rapidly with increasing radius (Touhami, Gies and Schaefer, 2011), the neutron star's maximum accretion rate is heavily dependent on the periastron distance of its orbit. Thus, the neutron star's maximum accretion rate is higher for systems with a smaller orbital period and higher eccentricity. The mass ejection rate of the Be star varies the overall density of the disc and thus it controls the density of the matter that the neutron star accretes. Thus, there is a linear relationship between the Be star's mass ejection rate and the neutron star's maximum accretion rate. The

dependence of the maximum accretion rate on the orientation and viscosity of the disc is negligible. It should be noted however that observable systems will exhibit a maximum X-ray luminosity during particularly dynamic disc events. As all the simulations are in a steady state, the accretion rates here are best considered relative.

The relationship between the size of the Be star's circumstellar disc, the orbital period and the semi-major axis were tested using simulations. The relationship between disc size and semi-major axis was similarly tested. In both cases, the simulation data agrees with the observational fits. The simulations suggest that the observational sample of Be/NS binaries with periods of $P_{\rm orb} \leq 150$ days possess eccentricities that are distributed in the range $0.0 \leq e \leq 0.5$. It is also suggested that the binaries with larger orbital periods have a wider distribution of eccentricities and a larger average eccentricity. The observational data has a much smaller sample of systems at higher orbital periods which could be contributing to the differences in the fits.

Chapter 5

Modelling the observable behaviour of SXP 5.05

SXP 5.05 was first detected via INTErnational Gamma-Ray Astrophysics Laboratory (INTEGRAL) observatory (Coe et al., 2013) as a bright X-ray source based in the Small Magellanic Cloud (SMC). Due to the eclipsing nature of the binary, its orbital period was accurately measured as 17.13 days.

Coe et al. (2015) considered the X-ray behaviour of SXP 5.05 in further detail, allowing for the determination of an accurate orbital model solution. The orbital eccentricity is found to be 0.155 and the orbital period is confirmed to be 17.13 days. It is calculated by fitting to a simple spin-up model and a radial velocity model simultaneously using Doppler-shifted X-ray pulsations. The initial attempts resulted in poor fits. A highly variable accretion rate caused by a clumpy wind was suggested to be the cause. The neutron star is occulted not by the Be star but by some extended structure which is interpreted as the circumstellar disc of the Be star. A simple 2-dimensional model is proposed that involves the neutron star ploughing through the circumstellar disc that is perpendicular to the orbital plane.

Figure 5.1 shows simultaneous optical and X-ray observations of SXP 5.05 over a 200 day period (see Section 5.2). Note that in the optical band, there is often a minimum before periastron and often a maximum following it. There is a large increase in the size of the disc that takes place over ∼3-4 orbits. The X-ray data show an extreme minimum following every periastron for approximately one fifth of an orbital period (see Section 5.5). The maximum value of X-ray flux occurs shortly before periastron.

In this chapter, the effects of a neutron star travelling directly through the disc are investigated. Simulation results are used to explain the behaviour of the observational data shown in Figure 5.1. Section 5.1 states the properties of all the simulations discussed within the chapter. In Section 5.2, the visible area of the disc

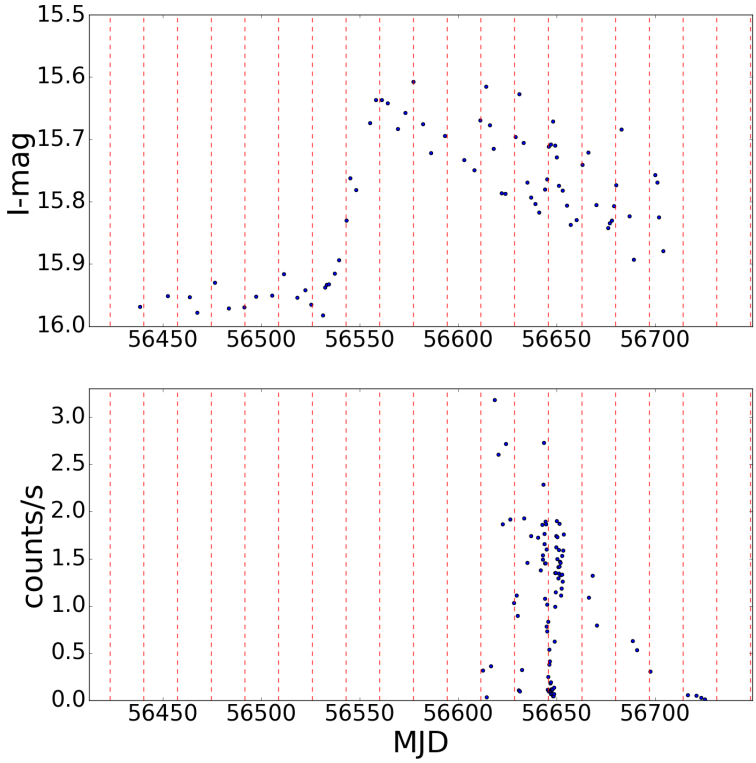

Figure 5.1: Observational data of SXP 5.05 over a period of 200 days. Red dashed lines indicate the neutron star's periastron. Top: OGLE I-band measurements. Bottom: Swift X-ray flux measurements.

is compared to the observed optical data, with the aim of matching the timescales over which the I-band magnitude rises and falls during the outburst. This part of the chapter is used to restrict the parameters and determine the best fitting systems. Section 5.4 discusses the column density of neutral hydrogen that obscures the neutron star for the restricted sample of simulations. The fitting of both the optical timescales in the previous section and the obscuration allows for one simulation to be chosen as the best match to the observational data. Section 5.5 uses the predicted obscuration to determine the X-ray behaviour of the neutron star from an observer's point of view. Section 5.6 shows the evolution of the Hα line emission shape for the Be star's circumstellar disc. Section 5.7 discusses the comparison between the simulation and observational data and it is considered whether the passage of the neutron star through the disc is an explanation for the X-ray occultations in SXP 5.05.

5.1 Simulations

The simulations have an initial mass ejection of 10^{-11} $M_{\odot}yr^{-1}$ and are evolved until they reach equilibrium, i.e. when the number of particles in the disc around an orbit changes by less than 1% for more than 5 orbits. The simulations shown in this chapter contain 20,000 to 50,000 particles at equilibrium. Following this, the mass ejection is increased and the system evolved further. Simulations are performed with increased mass ejections of $10^{-10}, 10^{-9}, 10^{-8}, 10^{-7}$, 10^{-6} and 10^{-5} $M_{\odot}yr^{-1}$. When the mass ejection of the Be star is increased, the disc grows in size temporarily and then shrinks until it reaches a state of equilibrium. During this process, the disc grows larger than the orbit of the neutron star (see Figure 5.2). This causes the neutron star to pass directly through the disc at ~ 10 stellar radii away from the centre of the Be star.

The Shakura-Sunyaev viscosity parameter of the simulation is also varied to best fit the data. The assumed values lie between $\alpha = 0.1$ and 1.5. Note that $\alpha = 0.63$ and $\alpha = 0.26$ have been theoretically determined as the median values of the viscosity parameter during build up and dissipation respectively (Rímulo et al., 2018) and Ghoreyshi et al. (2018) use viscosities varying between $\alpha = 0.1$ and $\alpha = 1.0$ to successfully model the lightcurve of ω CMa.

All systems have a Be star of mass $13M_{\odot}$ and radius $7R_{\odot}$, as determined in Coe et al. (2015), and a neutron star of mass $1.4M_{\odot}$ and radius 10km. The Be star's circumstellar disc is at a 45° angle to periastron (illustrated in Figure 5.2) and is perpendicular to the orbital plane, thus making the rotation of the disc arbitrary when considering accretion onto the neutron star. For further details on the implementation of the code, see Section 3.1.

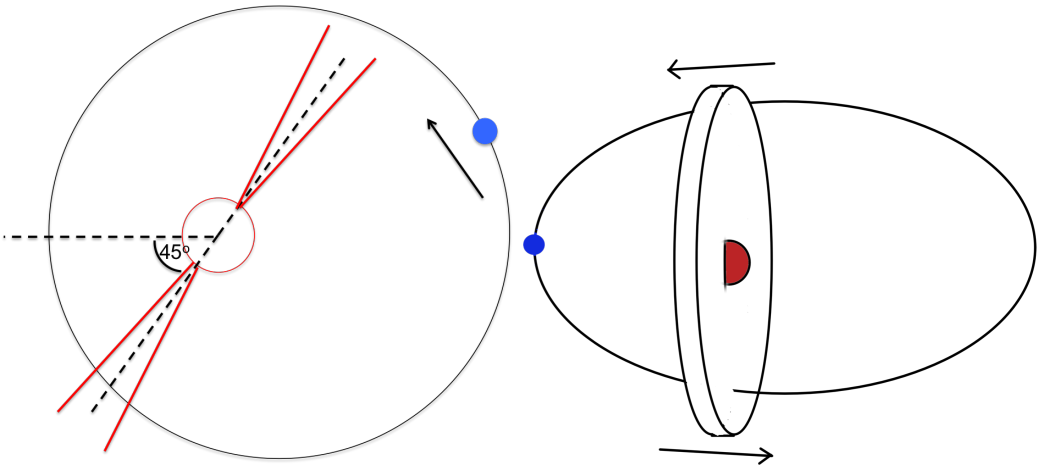

Figure 5.2: Left: An illustration of the proposed geometry of the Be/X-ray binary SXP 5.05. The red circle is the Be star and the connected red lines indicate the flaring circumstellar disc. The blue circle is the orbiting neutron star. Dashed lines depict the 45° angle of the disc to periastron. Right: An illustration of the suggested observer's view of SXP 5.05. The red circle surrounded by a disc and the blue circle represent the Be star and neutron star respectively. The neutron star orbits anti-clockwise, as shown by the arrows, and is at periastron.

5.1.1 Changes in mass ejection

When the mass ejection rate of a Be star is modified, the material in the disc shifts to assume a new density profile that remains in equilibrium with the new mass ejection rate. One such example of this has been shown by Okazaki et al. (2002) where a Be star with no circumstellar disc is given a constant mass ejection rate. The disc is shown to grow into a state of equilibrium. The time it takes for the density to reach equilibrium increases with radius. Haubois et al. (2012) showed that two different regions are created when the mass ejection rate of the Be star (with a built up circumstellar disc) is reduced to zero. The first of these is an inner region of material flowing towards the Be star due to the material being accreted back onto the Be star. The other outer region continues to flow outwards and behaves as if the ejection rate of the Be star is unchanged. The radius that separates these two regions is known as the stagnation point and moves outwards with time until the entire disc is flowing inwards.

In this chapter, the mass ejection rate of the Be star is increased instantaneously by at least an order of magnitude. This creates a region of higher density at the equator of the Be star that propagates outwards. Much like the stagnation point, there is a radial separation between the two regions that moves away from the central star. However, unlike the case where the ejection rate is reduced, both regions are moving outwards. This leads to an increase in the size of the disc that is proportional to the size of the change in mass ejection. The inner and outer regions are separated by a large gradient in density.

In the case of a Be star with a binary companion, the disc can grow larger than the radius at which it would usually be limited to, i.e. the truncation radius (Okazaki et al., 2002). The disc can initially grow rapidly due to the phenomena described above but when the overall density profile of the disc comes closer to equilibrium, the disc shrinks quickly again due to the truncation of the binary partner. This means that the Be star's circumstellar disc can initially grow and then shrink to its original size even when the mass ejection rate remains constant (see Figure 5.3).

5.2 Optical behaviour

Variations in the optical brightness of SXP 5.05 are related to the properties of the circumstellar disc. Hence, the visible area of the disc is calculated and the behaviour of this quantity is used as a preliminary fit to the observational data. The aim is to reproduce the rate of increase and decrease of I-band flux, as shown in Figure 5.1. Variation over time of both mass ejection and artificial viscosity is investigated. Note that there are only observational X-ray data for the final part of the OGLE data.

The visible area of the disc is calculated straightforwardly by placing a grid on the system oriented to the observer's line of sight. The addition of the number of grid squares that contain disc matter provides the resultant area. As this is a simplified method and the emission of the disc is not being modelled accurately, the maximum and minimum of the visible disc area is scaled to the observed I-band flux. Thus, absolute values of flux are not comparable, only the times of the changes.

This treatment assumes that the entirety of the disc is optically thick. Vieira et al. (2015) show that the Be star's disc is optically thick up to a given radius that is wavelength dependent. This region is known as the pseudo-photosphere and its radius, $\overline{R}$, is a function of the stellar parameters as follows

$$\overline{R} \propto \rho_0^{2/(2n-\beta)} \lambda^{(2+u)/(2n-\beta)}, \tag{5.1}$$

where ρ_0 is the base gas density of the Be star's circumstellar disc, λ is the given wavelength, β is the disc flaring exponent and u is given by

$$u = \frac{d\, ln(g_{\mathrm{ff}} + g_{\mathrm{bf}})}{d\, ln\lambda}. \tag{5.2}$$

g_{ff} and g_{bf} are free-free and bound-free gaunt factors, respectively. Vieira et al. (2015) show that a disc with a base gas density of $\rho_0 = 8.4 \times 10^{-11}$ g cm^{-3} has a

pseudo-photosphere that extends to ~ 3.5 stellar radii for a wavelength of $\lambda = 2\mu$m (the I-band includes $\sim 0.1 - 1\mu$m). The base gas density of the simulations during the event are orders of magnitude higher than this (up to $\sim 10^{-7}$ g cm^{-3}) and hence a scaled $\overline{R}$ is certainly larger than the maximum radius that the disc reaches (~ 20 stellar radii). However, there are two issues with this assumption. Firstly, the starting point of the simulation has a base gas density comparable to 8.4×10^{-11} g cm^{-3} and hence $\overline{R}$ does not extend to the edge of the disc in this case. The other issue is that during the event, the density profile of the disc is not well behaved and so it is difficult to consider exactly where the pseudo-photosphere ends. The assumption that the entirety of the disc is equally emissive in the I-band is a simplification and using radiative transfer methods would yield more accurate results.

5.2.1 Effect of viscosity

The left plot in Figure 5.3 shows the visible disc area for four simulations of varying α. The values shown are relative to the visible disc area at the moment the Be star's mass ejection is increased and hence do not represent the size of each individual disc at equilibrium. The area of the disc with a viscosity parameter of $\alpha = 0.1$ is almost two times larger than the disc with $\alpha = 1$.

The rate of disc growth decreases with larger viscosity parameters. However, discs with larger viscosity are found to decrease in size faster after reaching a maximum, implying the need for a lower viscosity when the disc is shrinking. The rate of disc recession remains very close to the rate of growth for all values of α. Reducing the viscosity alone is not sufficient to reproduce the slower decline of the second half of the data.

There is a delay between the increase in ejection and the growth of the visible area of the disc. This is due to the viscosity timescale of the disc, i.e. the time it takes for the region of higher density to propagate through the disc (King et al., 2013). The viscosity timescale of the disc is given by

$$\tau_{\text{visc}} = \frac{r^2}{\nu}, \tag{5.3}$$

where r is the distance the higher density region has travelled. The viscosity of the fluid, ν, is given by

$$\nu = \frac{\alpha c_s^2}{\Omega_{\text{K}}(r)}, \tag{5.4}$$

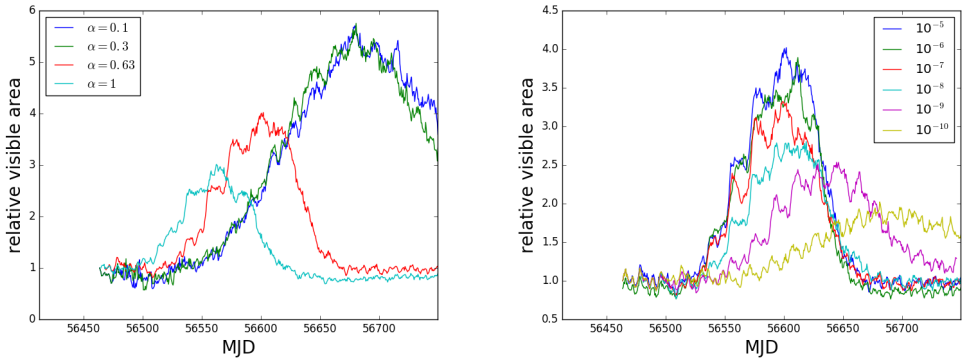

Figure 5.3: Left: The visible area of the disc against time for four systems with viscosities parameters of $\alpha = 0.1, 0.3, 0.63$ and 1. It is relative to the visible area at the time when the mass ejection is increased (the initial point of each line). All four systems have had the mass ejection of the Be star increased from 10^{-11} to 10^{-5} $M_{\odot}yr^{-1}$. Right: The visible area of the disc against time for systems with increased Be star mass ejection of $10^{-10}, 10^{-9}, 10^{-8}, 10^{-7}$, 10^{-6} and 10^{-5} $M_{\odot}yr^{-1}$. It is relative to the visible area at the time when the mass ejection is increased (the initial point of each line). All systems have a viscosity parameter of $\alpha = 0.63$.

where α is the Shakura-Sunyaev viscosity parameter, c_s is the speed of sound in the fluid and Ω_K is the Keplerian velocity at radius r. The decretion disc in the simulations extends to 5-10R_* and α varies from 0.1 to 1. The speed of sound calculated from the simulations is $\sim$ 10km s^{-1}. Thus, the time taken for a feature to propagate from the Be star surface to the disc edge is of the order of hundreds of days for systems with $\alpha \sim 1$. This timescale is closer to a thousand days for the lower values of α. However, the growth of the disc is faster than the viscosity timescale because the newly ejected material displaces the outer disc. Therefore, by the time the higher density region reaches the edge of the initial disc, it has already grown considerably.

5.2.2 Effect of mass ejection

The right plot in Figure 5.3 shows the visible disc area with time for six simulations that have had their mass ejections increased from 10^{-11} $M_{\odot}yr^{-1}$. Greater increases in mass ejection lead to a faster rise and fall in the visible area of the disc, similar to viscosity. Smaller increases of mass ejection require a much longer time for the visible disc area to fall than the time for it to rise. None of the systems shown in the right of Figure 5.3 exhibit both the rapid increase and slower decline that were observed in SXP 5.05. Hence, a more complex variation of mass ejection over time is necessary.

The behaviour of the disc is extremely sensitive to both the duration and magnitude of any mass ejection variation. Maintaining an increased mass ejection for more than two orbits leads to the approximately symmetric behaviour seen in the left of Figure 5.3. We find the only way to replicate the times of both the rise

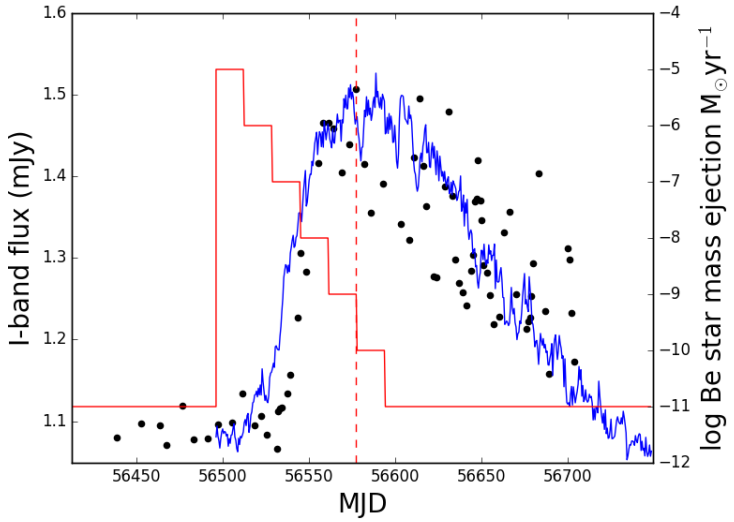

Figure 5.4: OGLE flux (black points) and estimated I-band flux (blue line) for best-fitting simulation as function of time. The mass ejection of the system is initially increased from 10^{-11} $M_\odot yr^{-1}$ to 10^{-5} $M_\odot yr^{-1}$ and then decreased by an order of magnitude every $\sim P_{orb}$ until the ejection rate has returned to 10^{-11} $M_\odot yr^{-1}$. This is illustrated by the solid red line. The vertical dashed red line indicates when the viscosity parameter is changed from $\alpha = 1.5$ to $\alpha = 0.1$.

and fall of the optical data is to have a short and large initial increase in mass ejection, after which, the mass ejection falls again.

5.2.3 Combining viscosity and mass ejection

One would reasonably expect the mass ejection to decrease as a function of time after a large outburst. Thus, the mass ejection of the Be star is decreased in steps until it reaches the original rate of 10^{-11} $M_\odot yr^{-1}$. The time between steps is assumed to be approximately a binary period and the steps are each an order of magnitude in $M_\odot yr^{-1}$. This is combined with a single change in the viscosity parameter from $\alpha = 1.5$ to $\alpha = 0.1$ during the event. In order to recover the rapid rise to maximum visible disc area, the viscosity is changed approximately five orbits after the mass ejection is increased.

Figure 5.4 shows the visible disc area compared against the observational optical data for the best fitting simulation. The system begins at equilibrium, with a Be star mass ejection of 10^{-11} $M_\odot yr^{-1}$. The Be star's mass ejection is then increased to 10^{-5} $M_\odot yr^{-1}$ and the viscosity parameter is set to $\alpha = 1.5$. After approximately one orbit the mass ejection is then decreased by an order of magnitude every orbit until it reaches the original rate of 10^{-11} $M_\odot yr^{-1}$. Approximately five orbits after the initial increase in mass ejection, viscosity is changed to $\alpha = 0.1$ (the same time that ejection is changed to 10^{-10} $M_\odot yr^{-1}$).

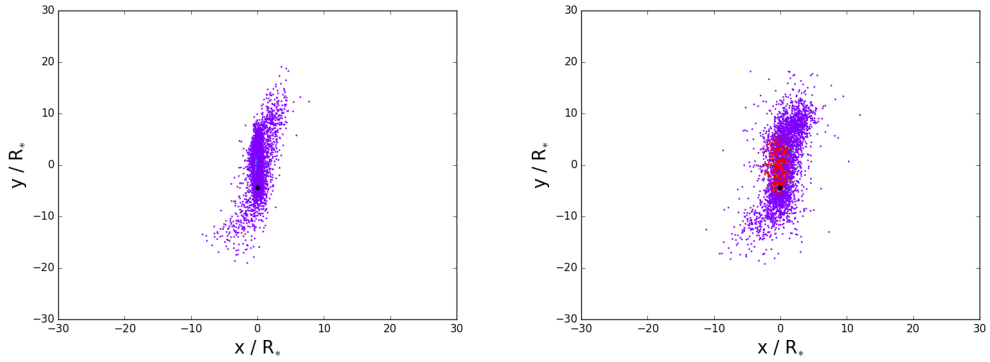

Figure 5.5: Snapshots of the disc and neutron star for the best fitting system shown in Figure 5.4. The left plot shows the system at the moment when the mass ejection is increased and the plot on the right shows the system four orbits after that. Red points shows the inner, higher density region of the disc created by the increased mass ejection and purple points show the lower density region that remains from the initial disc. The solid black circle shows the position of the neutron star that lies in front of the disc. This plot is shown in the assumed observer's line of sight.

Figure 5.5 is an illustration of the best fitting system, shown in Figure 5.4, at two times. The first plot shows the moment the Be star's mass ejection is increased and the second is four orbits after. As the disc grows in size, the outer regions interact more closely with the neutron star. Due to the disc's misalignment to the orbital plane, the outer regions bend out of the plane of the disc. This gives rise to a greater rate of increase in visible disc area. The larger disc also yields a thicker edge and, as the disc is $\sim 30°$ away from edge on, is another contributing factor to the increasing visible area.

The expected range of mass ejection for Be stars is $10^{-12} - 10^{-9} M_{\odot}\mathrm{yr}^{-1}$ (Vieira et al., 2015), with typical values for the mass ejection of observable stars being 10^{-10} $\mathrm{M}_{\odot}\mathrm{yr}^{-1}$ (Rímulo et al., 2018). The outburst that SXP 5.05 undergoes is dependent on both viscosity and mass ejection, and thus, there is more than one possible combination of these quantities that can explain it. However, it is required that either viscosity, mass ejection or both are higher than theory suggests for the observed optical timescales to occur. The system shown in Figure 5.4 is used for the data in the remainder of this chapter.

5.3 Disc eccentricity

The Kozai-Lidov mechanism is important to consider because of the large inclination of the disc to the orbital plane (Martin et al., 2014). This means that the disc could be largely eccentric and even undergo fragmentation in extreme circumstances (Fu, Lubow and Martin, 2017). Using Equation 3 from Martin et al. (2014), the period of the Kozai-Lidov mechanism for this system is of the order of ~ 100 $\mathrm{P}_{\mathrm{orb}}$ and the requirement for equilibrium is <10 $\mathrm{P}_{\mathrm{orb}}$.

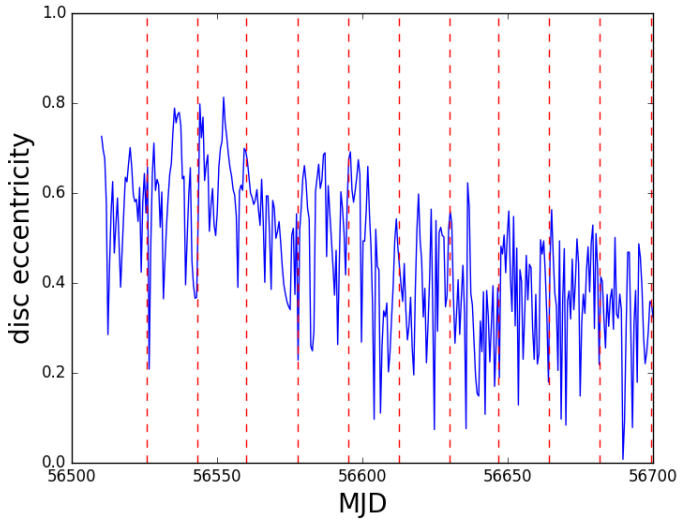

Figure 5.6: The eccentricity of the Be star's circumstellar disc with time for the best fitting system shown in Figure 5.4. The red dashed lines denote periastron.

Figure 5.6 shows the eccentricity of the Be star's circumstellar disc with time. Before the mass ejection of the Be star is increased, the eccentricity of the disc is very high, reaching a maximum of ~ 0.8 and then it decreases over the event. Due to the extreme inclination of the disc, the maximum eccentricity possible is $e \sim 1$. The eccentricity is close to 0.8 when the mass ejection is increased and thus, the Kozai-Lidov mechanism has started to take effect. When the mass ejection is increased, a large number of new particles flow outward from the star with circular orbits around the Be star. This suppresses the eccentricity of the disc as seen in Figure 5.6.

The variation in eccentricity is demonstrated visually in Figure 5.7. The change in eccentricity is greater for discs with a smaller viscosity parameter and hence the system shown has a viscosity parameter of $\alpha = 0.1$. The shape of the disc at the moment the mass ejection is changed is extremely eccentric and within four orbits has circularised considerably. This effect is much less visible in the best fitting system shown in Figure 5.4.

5.4 Neutron star obscuration

The X-ray behaviour of SXP 5.05 can be explained by a disc that grows larger than the neutron star's orbit. If the neutron star passes directly through the disc, any X-ray emission that is visible to an observer will be obscured by the material along the line of sight. The column density of neutral hydrogen, N_{H}, is shown in Figure 19 of Coe et al. (2015). To mimic these observations, the simulation data should show a peak in obscuration at a binary phase of ~ 0.1 with values in the range

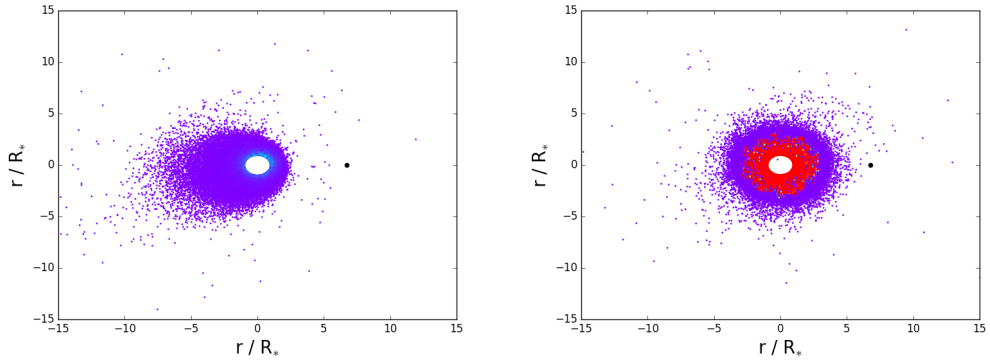

Figure 5.7: Snapshots of the disc and neutron star in the Be/X-ray binary with a viscosity of $\alpha = 0.1$, which has had its mass ejection changed from 10^{-11} $M_{\odot}yr^{-1}$ to 10^{-5} $M_{\odot}yr^{-1}$ (a system contained in Figure 5.3). The left plot shows the system at the moment when the mass ejection is increased and the plot on the right shows the system four orbits after that. Red points show the inner, higher density region of the disc created by the increased mass ejection and purple points show the lower density region that remains from the initial disc. The solid black circle shows the position of the neutron star and the Be star is reprensented by the white space at the centre of the disc. The plots are in the plane of the disc.

$N_{\rm H} \sim 10^{21} - 10^{24}{\rm cm}^{-2}$.

The column density of neutral hydrogen atoms is calculated using the Saha ionisation equation in the following form

$$\frac{x^2}{1-x} = \frac{1}{n}\left(\frac{2\pi m_e kT}{h^2}\right)^{3/2} e^{-13.6eV/kT}, \tag{5.5}$$

where x is the fraction of ionised hydrogen, n is the column density of gas particles and T is the temperature of the gas. The column density is calculated by integrating in a cylinder along line of sight to the neutron star. As the neutron star is only obscured by elements of the disc at ~ 10 stellar radii or greater, a temperature of $T = 0.6T_{eff}$ is adopted. A column density of $N_{\rm H} \sim 10^{21.5}$ is used for the interstellar medium, to match the data in Coe et al. (2015).

The disc is assumed to be composed entirely of hydrogen and a

Figure 5.8 shows the amount of disc material that obscures the neutron star along a viewing angle illustrated in Figure 5.2. There are two occultations per orbit, one just after periastron at a binary phase of ~ 0.1 and one preceding periastron which is negligible in comparison. The duration of the larger obscuration after periastron is approximately one fifth of an orbit. Therefore, the time and duration of the peak obscuration in Figure 5.8 agrees with the observed values shown in Coe et al. (2015). $N_{\rm H}$ in the simulation remains inside the observational data's range of $\sim 10^{21} - 10^{24}{\rm cm}^{-2}$.

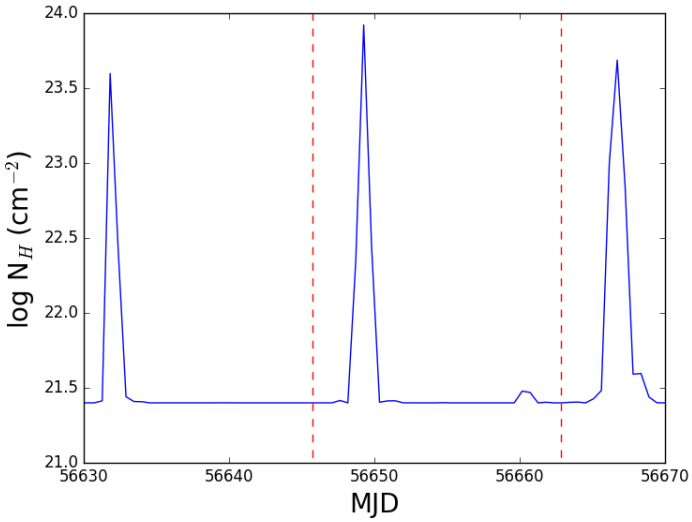

Figure 5.8: The column density of neutral hydrogen obscuring the neutron star against time for the best-fitting system shown in Figure 5.4. The red dashed lines denote periastron.

5.5 Neutron star X-ray luminosity

The X-ray luminosity of the neutron star is calculated from its captured mass as follows

$$L_X = \frac{GM_X\dot{M}}{R_X}, \tag{5.6}$$

where $\dot{M}$ is the rate of mass capture and M_X and R_X are the compact object's mass and radius respectively. This is converted into an observed flux by assuming a distance of 60 kpc (Scowcroft, 2016). Using the amount of obscuring matter (as calculated in Section 5.4) the expected counts per second can be computed using WebPIMMS (found at `https://heasarc.gsfc.nasa.gov/cgi-bin/Tools/w3pimms/w3pimms.pl`). The energy range for WebPIMMS is set to 1-10 keV and the Galactic column density of hydrogen is assumed to be $\sim 10^{21.5}$cm^{-2}. A photon index of 1.53 is used, as determined in Coe et al. (2015). Although the obscuring interstellar medium will be dominated by material with Galactic abundances, the obscuring material from the disc is dependent on the abundances in the SMC. The metallicity of the obscuring material from the Be star's disc is assumed to be [Fe/H] = -0.94 dex to match the average metallicity of the SMC (Choudhury et al., 2018). However, the abundances in the disc are likely even lower than those in the SMC because it consists of the material that was present on the surface of the Be star. Hence, the attenuation from the material is overestimated but only twice per orbit as shown in Figure 5.8.

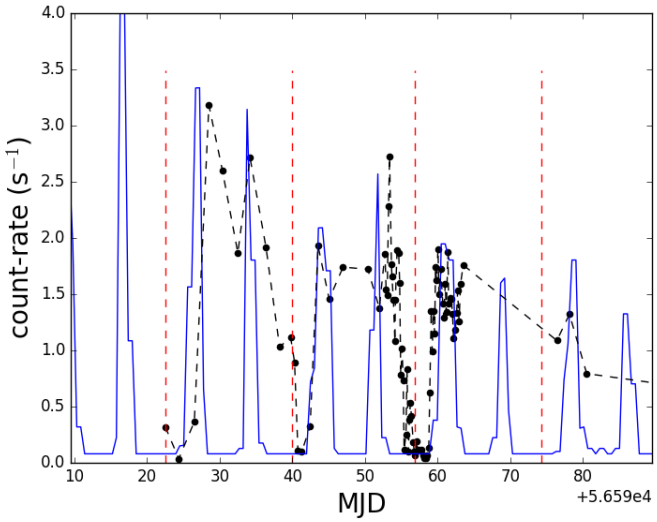

Figure 5.9: The predicted X-ray counts per second of the neutron star calculated for the best fitting system shown in Figure 5.4. The observational X-ray data are shown by the black points. Red dashed lines indicate the time of the neutron star's periastron.

Figure 5.9 shows the neutron star's mass capture converted into a luminosity and then attenuated by the additional local column density of neutral hydrogen associated with the circumstellar disc (see Figure 5.8). The counts per second predicted by the simulations assumes instantaneous accretion of all matter captured by the neutron star. The simulation data replicates the times and magnitudes of the X-ray outbursts. It shows the X-ray count rate dropping to zero between the interactions of the neutron star with the Be star's circumstellar disc, whereas the observational X-ray data show non-zero count rates that steadily decrease over time. Thus, there is a reservoir of mass that fuels the X-ray flux of the neutron star around its orbit (i.e. an accretion disc), which is fed by the Be star's decretion disc during interaction. The interaction with the disc causes an increase of X-ray flux twice per orbit. As the disc shrinks, less matter is captured, leading to the decreasing trend in X-ray flux with time. The peaks in the simulation data seem to often precede those seen in the observational data which would also suggest a delay between mass capture and accretion, which has been suggested previously (Okazaki and Hayasaki, 2004; Brown et al., 2018).

5.5.1 Radiation pressure

The high X-ray luminosities that are observed for SXP 5.05 mean that there is a significant accretion disc surrounding the neutron star which the model in this thesis does not take into account. It should also be expected that the radiation leaving the surface of the neutron star exerts a large pressure on the surrounding material. In this section, the interaction between the radiation pressure and the

circumstellar disc is considered very simply. Calculating the interactions fully would require the use of radiative transfer methods to model the propagation of the photons through the disc. Modelling is particularly important due to the dynamics of the disc when the neutron star is accreting from it. Here it is assumed that the neutron star is emitting isotropically, and that the radiation pressure, $P_{\rm rad}$, can be calculated as follows

$$P_{\rm rad} = \frac{L_X}{4\pi c r^2}, \tag{5.7}$$

where L_X is the X-ray luminosity of the neutron star, r is the distance from the neutron star. This treatment of radiation pressure assumes a large distance from the surface of the neutron star.

Using Equation 5.7, the radiation pressure is compared to the gas pressure of the disc at a given distance. The pressure is calculated directly from the code. This pressure is heavily dependent on the time during the simulation as the mass ejection of the star is varying and the disc is dynamic during the orbit. Thus, the values for pressure that are used are those that occur when the disc is at its densest. These values of pressure are also taken along the equatorial plane (the parameters of the disc vary both radially and along the height of the disc). The neutron star lies approximately 11 stellar radii from the Be star when it emits the maximum X-ray flux. The distance where the gas pressure is equal to the radiation pressure provides an idea of the maximum length scale for which the radiation pressure is important.

Assuming the maximum X-ray luminosity of $\sim 4 \times 10^{37}$ erg s^{-1}, the pressure exerted by the radiation matches the gas pressure in the disc at ~ 2 stellar radii from the neutron star (and thus 9 stellar radii from the Be star). This calculation assumes that there is no interaction between the radiation and the disc but the radiation pressure would be diminished with distance when travelling through the circumstellar disc. The photons would also interact with the surrounding accretion disc. Hence, the distance over which the radiation pressure falls off will certainly be smaller.

This approximate calculation implies that the radiation pressure interacts heavily with the outer parts of the Be star disc. This could be the reason for the large amplitude variations in the second half of Figure 5.5 that the model cannot reproduce.

5.6 Hα profiles

Be stars are well known for the Hα emission produced by their discs (Rivinius, Carciofi and Martayan, 2013). These profiles are the most direct method of observing the behaviour of the circumstellar disc. Hα profiles provide information about the inclination of the system via the prominence of a double peaked structure that arises due to Doppler effects. The size of the disc can be inferred from the equivalent width of the Hα profile.

Horne and Marsh (1986) applied a simplification of radiative transfer techniques to model accretion discs, formulating the line emission shapes for optically thin and optically thick cases. This method has since been applied to Be star accretion discs by Okazaki (1996) and Hummel and Vrancken (2000). The method is unreliable for extreme inclination angles ($\geq$80°).

Horne and Marsh (1986) provided a simplified expression for the broadening of the line emission by Doppler shifts. These Doppler shifts are due to the orbital motion of the material in the disc along the line of sight. This shear broadening is expressed as

$$V_{\rm shear}(R) = -\frac{H}{2R} V_K(R) \sin i \tan i \sin\phi \cos\phi, \tag{5.8}$$

where i is the inclination of the disc, ϕ is the azimuthal angle in the disc plane, H is the disc height, R is the radius and V_K is the local value of the Keplerian velocity. The line optical depth is given by

$$\tau_\nu = \frac{W(R)}{\cos i} \frac{\lambda_0}{\sqrt{2\pi}\Delta V} \exp\left[-\frac{1}{2}\left(\frac{V - V_D(0)}{\Delta V}\right)^2\right], \tag{5.9}$$

where λ_0 is the rest wavelength, V_D is the Doppler velocity shift produced by Keplerian motion and ΔV is given by

$$\Delta V = \sqrt{\Delta V_{th}^2 + V_{shear}^2} \tag{5.10}$$

and ΔV_{th} is the thermal broadening. $W(R)$ is given by

$$W(R) = \frac{\pi e^2}{mc} f \Sigma(R), \tag{5.11}$$

where f is the absorption oscillator strength and $\Sigma(R)$ is the surface density. In the previously mentioned treatments of shear broadening, the disc density is provided by a theoretical function. In this chapter, the density is calculated at each integration step from the simulation particles.

Figure 5.10 shows emission line profiles predicted by the simulation using the method described above. They are compared in the figure to the observational data from Coe et al. (2015) which have been corrected for the redshift of the SMC (Harris and Zaritsky, 2006). The key features of the observational data are replicated by the simulations. The Hα profiles from the simulations exhibit a double peaked structure where the red (right) peak is larger, lies closer to the Hα rest wavelength and has a shoulder on the redward side. This asymmetry can be attributed to the eccentricity of the disc, as discussed in Section 5.3. The profile has the worst fit at apastron (binary phase of 0.5) and the reverse is true for periastron.

5.7 Discussion and Conclusions

In this chapter, a large optical outburst of the Be/X-ray binary, SXP 5.05, is investigated. Simulations are performed using the orbital solution derived in Coe et al. (2015). As the most comprehensive set of observational data, the optical behaviour of SXP 5.05 was used to narrow down the suitable simulations. The only way to fully replicate the observed behaviour of the optical data is to have a short and large increase in mass ejection initially, which then falls. The viscosity is also very high during the build up of the disc and lower during the dissipation - as described in Rímulo et al. (2018). A mass ejection rate that rapidly decreases to the initial rate is assumed. The maximum value of the mass ejection is much larger than the expected range for mass ejection of Be stars and the assumed viscosity is larger than previously suggested, but are similar to those used in Ghoreyshi et al. (2018) to model ω CMa.

The disc eccentricity is high at the beginning of the outburst and decreases over time. Different results would be obtained depending on when the outburst occurs during the Kozai-Lidov mechanism, due to the variation in the inclination and eccentricity of the Be star's circumstellar disc. As the eccentricity is close to 0.8 at the beginning of the outburst, the Kozai-Lidov mechanism has taken effect. Investigating the possible role the K-L effect might play in such Type II outbursts is left for future work.

The increase in mass ejection causes the disc to increase in size, allowing it to grow larger than the truncation radius of the neutron star. Thus the neutron star is occulted twice per orbit: once as it passes behind the disc and once as it passes directly through it. The measured column density of neutral hydrogen that obscures

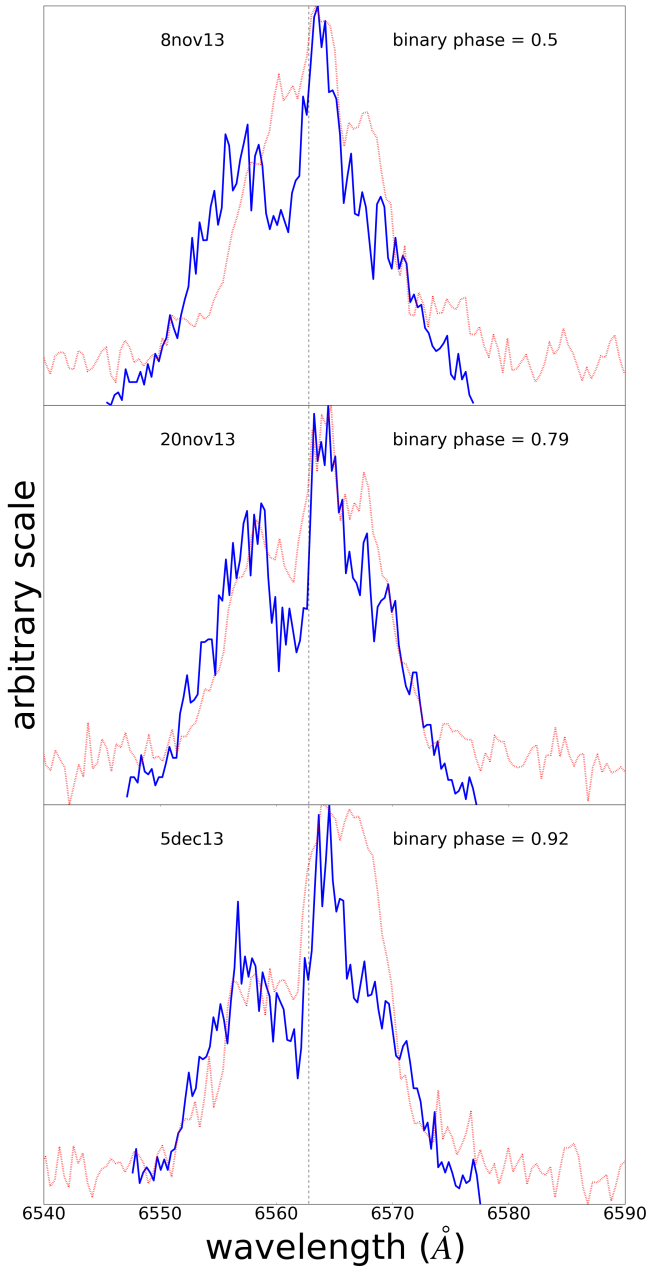

Figure 5.10: Successive Hα line emission shapes for the simulation data (in solid blue) compared against the observational line profiles (in dotted red) taken from Coe et al. (2015). The profiles are produced for 2013 Nov 5, 20 and Dec 5. The black dashed line indicates the Hα rest wavelength, 6562.8Å. The binary phase is shown for each profile, where a binary phase of 0.0 is periastron.

the neutron star allows the appropriate simulations to be constrained further.

The X-ray flux of the simulations can be approximated by calculating the amount of mass captured by the neutron star and then applying a simple extinction function that is dependent on the aforementioned density of obscuring matter. The neutron star accretes twice per orbit with the time of the accretion and the attenuation of the X-ray flux matching the X-ray data from SXP 5.05. Hence, the X-ray behaviour of SXP 5.05 can be described well by the suggested model in this chapter. The feature that the simulations do not model sufficiently, is the underlying X-ray flux seen between outbursts in the observational data. In the model, only the mass capture is used to calculate an instantaneous X-ray flux and so between accretion events, mass accretion drops to zero. The difference in behaviour could be explained by an accretion disc forming around the neutron star in SXP 5.05.

A simple treatment of the Hα line profiles is applied to the modelled disc and yields all the general features of the profiles seen in Coe et al. (2015). The red peak lies close to the rest wavelength and is much larger than the blue. The asymmetry of the predicted Hα profiles is due to the large eccentricity of the Be star's circumstellar disc. There is even a shoulder to the right of the red peak. However, this method does not recover the variations with time seen in the observational data.

Optical variations in Be star systems are be due to changes in the structure and size of the disc. The evolution of the disc is itself dependent on the mass ejection which is, in turn, dependent on the non-radial pulsations of the star. These non-radial pulsations are inherent to the star and do not change. They typically possess periods of the order of days. Thus, the large optical event seen in SXP 5.05 could be the result of the overlap of a number of the non-radial pulsations and hence, this event has a periodicity to it.

The results in this chapter imply a very specific nature to optical outbursts that occur in Be stars; a very sharp and large increase in the amount of matter ejected followed by a rapid decline over time. Although, it is a specific case it can provide more information about the complex nature of these systems. Understanding such extreme cases is important to determine the complete physics of Be star systems. The simulation data implies that any system with a disc heavily inclined to the orbital plane and undergoing a sufficiently large outburst will possess a disc that grows outside of the orbit of the compact object. This can be tested by the presence of an additional occultation of the X-ray source during the outburst. In the case of SXP 5.05, which possesses one obscuration of the neutron star per orbit and an additional one during outburst, it is possible to constrain the inclination angle to the observer. Therefore, this should be possible for similar Be/X-ray binaries.

Chapter 6

Decretion discs in Be/X-ray binaries: black holes versus neutron stars

Binary evolution models have predicted the existence of Be-black hole X-ray binaries, with Raguzova and Lipunov (1999) proposing the detection of such systems. They used Monte Carlo simulations to determine that there is an evolutionary track that leads to formation of Be/BH binaries. They tracked the evolution of 10^6 zero age main sequence binary systems with initial masses 10 to $120M_{\odot}$. A logarithmic distribution for initial binary separation was used. The simulations were run with and without kick velocity. Systems that evolved had a wide range of both orbital period and eccentricity. Orbital period varies from less than ten to thousands of days with a peak at tens of days in every dataset. Eccentricity can have any value between 0 and 1 with a maximum between 0.2 and 0.4 for all the simulations. One black hole binary system for every 20-30 neutron star systems was estimated.

More recent stellar population synthesis models by Ziolkowski and Belczynski (2011) also used varying kick velocities but modelled common envelope evolution and non-conservative mass transfer via Roche lobe overflow. A solar metallicity ($Z = 0.02$) for galactic binaries and a low metallicity ($Z = 0.008$) for Magellanic Clouds binaries were adopted. The Milky Way and Magellanic Clouds also had differing stellar initial mass functions. These initial conditions lead to a ratio in the galaxy of 30-50 neutron stars per black hole and a ratio in the Magellanic Clouds of $\sim$10. Therefore the expected number of Be X-ray binaries with black hole companions in the Galaxy should be $\sim$0 - 2 (Belczynski and Ziolkowski, 2009) and the lack of Be/BH binaries is not surprising. However, in the Magellanic Clouds, there should be $\sim$6 of these systems.

Zhang, Li and Wang (2004) proposed a greater truncation of the circumstellar disc in systems with shorter orbital periods. Given that some synthesis models predict black hole binaries will form with binary periods of less than ∼30 days (Podsiadlowski et al., 2003), it was proposed that all black holes truncate the Be star disc more effectively than neutron star companions. A smaller disc means interaction and accretion is less likely. Hence all black hole systems would be fainter X-ray objects.

The first confirmed Be-black hole binary system, MWC 656, was found by Casares et al. (2014). Its luminosity is less than 1.6×10^{-7} times the Eddington luminosity implying extremely inefficient accretion. This further enforces the link between the lack of known black hole binaries and low X-ray luminosity. Ribó et al. (2017) have shown that it has become ∼7 times fainter since it was observed in 2014. They also found that the observable quiescent behaviour is fully compatible with low mass X-ray binaries (LMXBs) with black hole companions. This suggests that black hole accretion is independent of the donor star. Casares et al. (2014) state that the Be star has a mass in the range of 10-16 $M_{\odot}$. Their observations yield a mass ratio of 0.41±0.07. It has an orbital period of 60.37 days and an eccentricity of 0.1, implying a periastron distance of $\sim28R_{\odot}$. From archival data of ROSAT over 7-11 July 1993 and Swift on 8 March 2011, they set an upper limit on the X-ray luminosity of $L_X < 10^{32}$erg s^{-1}. As the only known Be/BH system, we will use MWC656 as the reference object in our simulations. We also assume that it has the same mass ($13M_{\odot}$) as used in our simulations, and that the BH mass is $5.3M_{\odot}$.

More recently, Grudzinska et al. (2015) investigated the evolution that led to the formation of MWC656, finding that it must involve a common envelope phase followed by a supernova explosion. Given their results, they state that there must be $\sim 3-30$ Be/X-ray binaries containing a black hole in the Galactic disc. It is also suggested that if MWC656 is representative of the Be/BH binaries in the Milky Way, then it may indicate that standard stellar evolutionary theory needs to be revised.

6.1 The distribution of eccentricity in Be/NS systems

Given the importance of eccentricity in accretion in interacting binary systems, it is pertinent to discuss the eccentricity of observed Be/X-ray binaries. Be/NS binaries with known eccentricities in the Milky Way, LMC and SMC are shown in Table 6.1. Orbital period and maximum observed X-ray luminosity, L_{max}, are also included. This table is for demonstrating the low X-ray luminosity of MWC 656 and therefore some values may not be the most recent ones. Figure 6.1 illustrates the distribution of these eccentricities. Almost half of Be/NS systems have an eccentricity between 0.25 and 0.45. The second largest population is systems with circular orbits, the

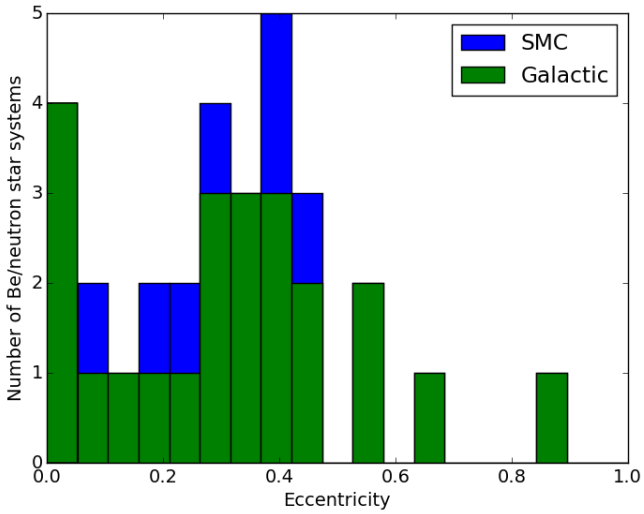

Figure 6.1: A histogram showing the distribution of Be/NS binaries with known eccentricity in the Milky Way and SMC (values from Table 6.1). The bars for the SMC are placed on top of those for the Milky Way. Therefore each bin shows the total number of systems with the given range of eccentricities. Three Be/NS binary systems have a lower limit on eccentricity of $e > 0.5$ and thus are not included.

significance of which is shown in Pfhal et al. (2002). In this sample, ∼82% of Be/NS binaries have an eccentricity of $e < 0.5$.

The relationship between eccentricity and maximum X-ray luminosity is shown in Figure 6.2. The single confirmed Be/BH binary, MWC 656, is included in addition to the Be/NS binaries. There is no clear relation between maximum luminosity and eccentricity for the Be/NS binaries (with a correlation coefficient of 0.02 and a significance of 0.92). MWC 656 has a considerably lower maximum X-ray luminosity than all the Be/NS binaries and is more than two orders of magnitude fainter than the faintest Be/NS system in this sample.

In this chapter, simulations are used to determine the reaction of the Be star's decretion disc to compact objects of different mass. The results predict that Be/BH binaries are fainter X-ray sources than Be/NS binaries. In Section 6.2, results from SPH (see Chapter 2) simulations of Be/X-ray binaries are shown. Systems of varying compact object mass and eccentricity are investigated, and the effects on base gas density, disc size and X-ray luminosity are discussed. Section 6.4 discusses

[1]http://xray.sai.msu.ru/ raguzova/BeXcat/title.html
[2]Reig and Nespoli (2013)
[3]Reig et al. (2016)
[4]Liu, van Paradijs and van den Heuvel (2006)
[5]Rajoelimanana et al. (2017)
[6]Coe and Kirk (2015)
[7]Coe et al. (2015)
[8]Townsend et al. (2011)
[9]Townsend et al. (2011)
[10]Schurch et al. (2008)

Table 6.1: Table of eccentricity and maximum observed X-ray luminosity for Be/X-ray systems in the Milky Way, LMC and SMC.

Milky Way	e	L_{max} (10^{36} erg s^{-1})	Reference
γ Cas*	0.26	0.039	[1]
V635 Cas	0.34	30	1
V615 Cas**	0.537	0.02	1
X Per	0.11	0.3	1
V725 Tau	0.47	20	1
GS 0834-430	0.12	11	1
GRO J1008-57	0.68	20	1, [2]
V801 Cen	>0.5	0.074	1
GX 304-1	>0.5	1	1
2S 1417-624	0.446	8	1
XTE J1543-568	<0.03	>10	1
2S 1553-542	<0.09	7	1
2S 1845-024	0.88	6	1
4U 1901+03	0.036	110	1
XTE J1946+274	0.33	5.4	1
GRO J1948+32	0.03	21	1
EXO 2030+375	0.41	100	1
SAX J2103.5+4545	0.40	3	1
2S 0114+65	0.16	0.49	[3], [4]
V 0332+53	0.42	340	2, 3
AX J1845.0-0433	0.34	1.4	3, 4
4U 1907+09	0.28	23	3, 4
KS 1947+300	0.03	88	3, 4
4U 2206+54	0.30	0.088	3, 4
MWC 656 (BH)	0.1	3.7×10^{-5}	1
LMC			
A0538-66	0.72	1000	1, [5]
SMC			
SXP 2.37	0.07	210	[6], 7
SXP 5.05	0.16	50	6, [7]
SXP 6.85	0.26	33	6, [8]
SXP 8.80	0.41	73	6, 7
SXP 11.5	0.28	10	6, [9]
SXP 18.3	0.43	30	6, [10]
SXP 74.7	0.4	35	6, 7

* γ Cas has a considerably lower X-ray luminosity due to the tidal/resonant interaction with the neutron star and hence it never remains in a steady state. This restricts the accretion of the neutron star (Negueruela and Okazaki, 2001).

** V615 Cas is also different to the other Be/NS binaries in the table because it is possibly another Be/BH system (Massi, Migliari and Chernyakova, 2017).

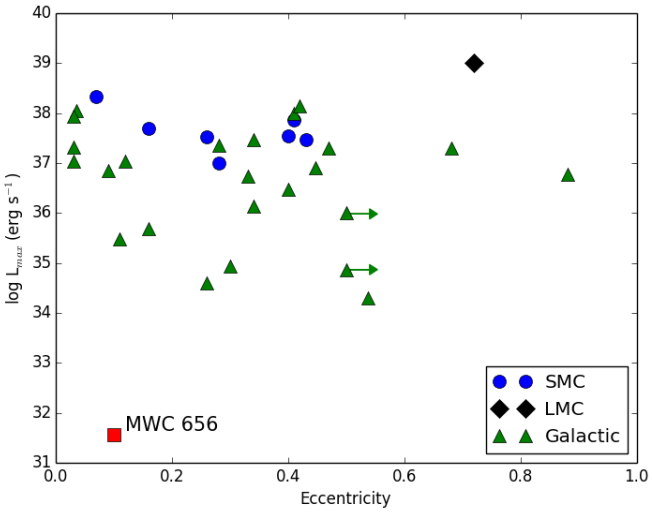

Figure 6.2: The relationship between maximum observed X-ray luminosity, L_{max}, and eccentricity for Be/X-ray binaries in the Milky Way, LMC and SMC. The only Be/BH system, MWC 656, is also included. Arrows demonstrate the lower limit on eccentricity for the 3 systems with $e > 0.5$. The values used for this figure are contained in Table 6.1.

the implications of these results, which are then compared with previous work, allowing predictions to be made for the possibility of future detections.

6.2 Simulations

All systems were evolved until they reached equilibrium. If the number of particles in the disc around an orbit changes by less than 1% for more than 5 orbits, the system is considered to be in equilibrium. The number of particles in the disc at equilibrium ranges from ∼20,000 to ∼200,000 and is dependent of the orbital period of the system. For further details on the implementation of the code, see Section 3.1.

6.2.1 Properties of simulated systems

All systems have a Be star of mass $13M_{\odot}$ and radius $7R_{\odot}$, to match a main sequence star with a B1V spectral type (Silaj et al., 2014). The expected range of mass ejection for Be stars is $10^{-12} - 10^{-9} M_{\odot}\mathrm{yr}^{-1}$ (Vieira et al., 2015), and a constant mass ejection of $\sim 10^{-11} M_{\odot}\mathrm{yr}^{-1}$ is assumed.

All orbits are coplanar and the periastron distance is kept at $\sim 80R_{\odot}$ because the truncation of the disc is heavily dependent on this value, which we take as the semi-major axis for a NS in a circular orbit with an P_{orb} of 20 days. P_{orb} for every simulation is shown in Table 6.2.

The density profile of a Be star's decretion disc is well modelled by the following

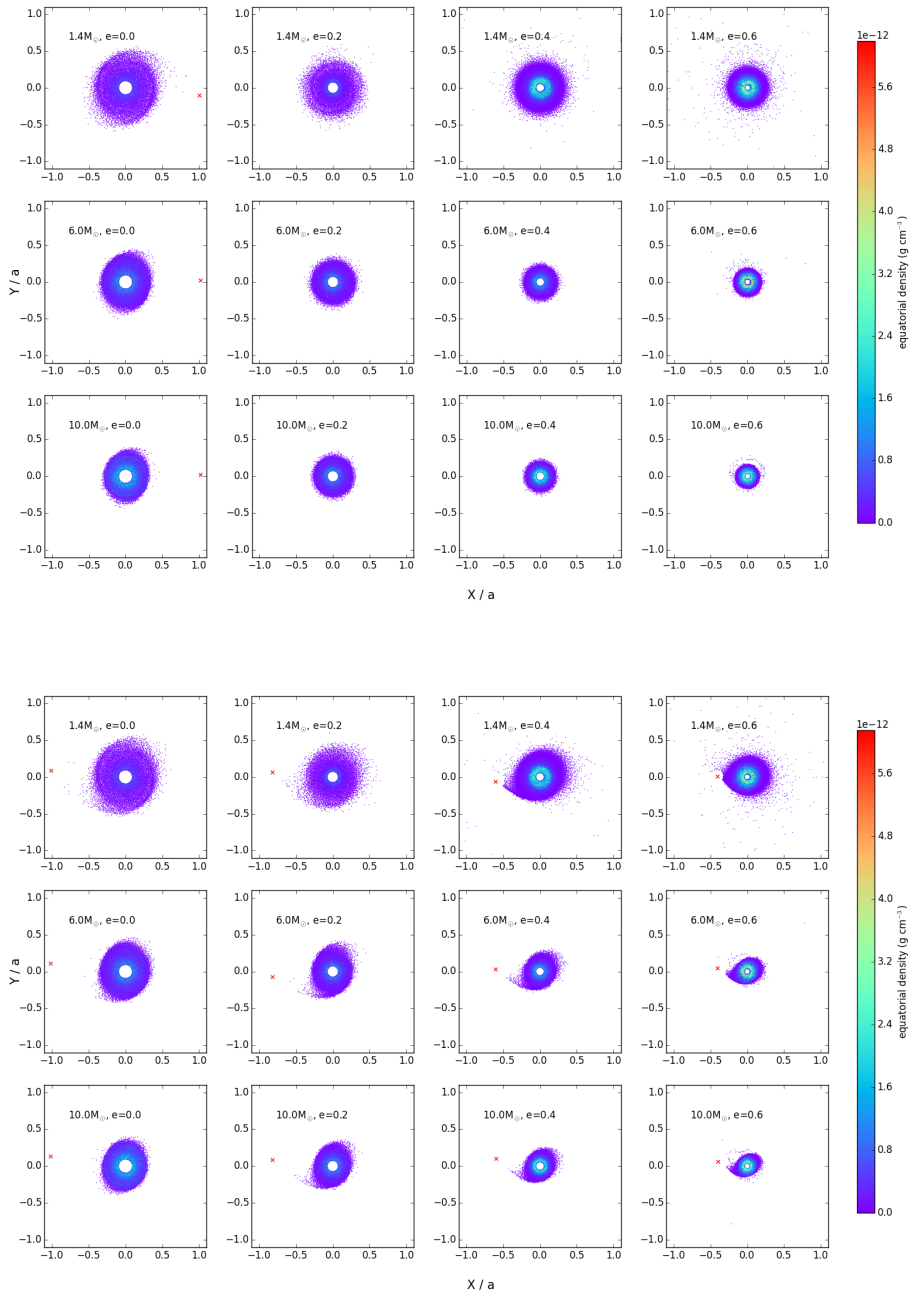

Figure 6.3: Images of the circumstellar disc normalised by the semi-major axis, a. Three different compact object masses are shown (increasing from top to bottom) and four different eccentricities (increasing from left to right). The parameters of the systems shown are M=1.4$M_\odot$, 6$M_\odot$, 10$M_\odot$ and e=0.0, 0.2, 0.4 and 0.6. The colorbar shows the equatorial density within the disc. The compact object is marked with a red cross and lies close to apastron (top 4x3 grid) or periastron (bottom 4x3 grid). Periastron distance is the same for all the simulations.

Table 6.2: Table of assumed orbital periods for all neutron star and 10 $M_\odot$ black hole systems used as input for our simulations.

e	P_{orb} (M_X=1.4 $M_\odot$)	$P_{\rm orb}$ (M_X=10 $M_\odot$)
0.0	20 days	15.8 days
0.1	23.4 days	18.5 days
0.2	28 days	22.1 days
0.3	34.1 days	27 days
0.4	43 days	34.1 days
0.5	56.6 days	44.8 days
0.6	79.1 days	62.6 days

equation (Touhami, Gies and Schaefer, 2011)

$$\rho(r,z) = \rho_0 \left(\frac{r}{R_*}\right)^{-n} \exp\left[-\frac{1}{2}\left(\frac{z}{H(r)}\right)^2\right], \tag{6.1}$$

where ρ_0 is the base gas density and n is the radial density exponent that is variable between 2.5 and 4 (Rivinius, Carciofi and Martayan, 2013). $H(r)$ is the disc's vertical scale height and is given by

$$H(r) = \frac{c_s}{V_K}\left(\frac{r}{R_*}\right)^{\frac{3}{2}}, \tag{6.2}$$

where V_K is the Keplerian velocity at the stellar equator and c_s is the speed of sound in the disc, which is temperature dependent.

The base gas density of the disc can approximate the overall density profile as shown by Equation 6.1. For $e \leq 0.1$, base gas density increases with M_X. The disc is compacted by the black hole or neutron star that spends all of its time in close proximity to the disc. For higher eccentricities, it has the opposite relationship. These systems have longer orbital periods and the compact object spends a smaller amount of time near the decretion disc. This is less disruptive and allows the disc to increase in size and decrease in density.

6.2.2 Truncation of the disc

The truncation of the Be star's disc is an established feature of Be/X-ray binaries (Štefl et al., 2007). Figure 6.3 illustrates the size of the disc for 12 of the systems presented in this chapter and Figure 6.4 shows the numerical relationship between disc size and M_X. The size of the disc is defined as the radius that contains 90% of the simulation particles. The length scale has been normalised by the semi-major

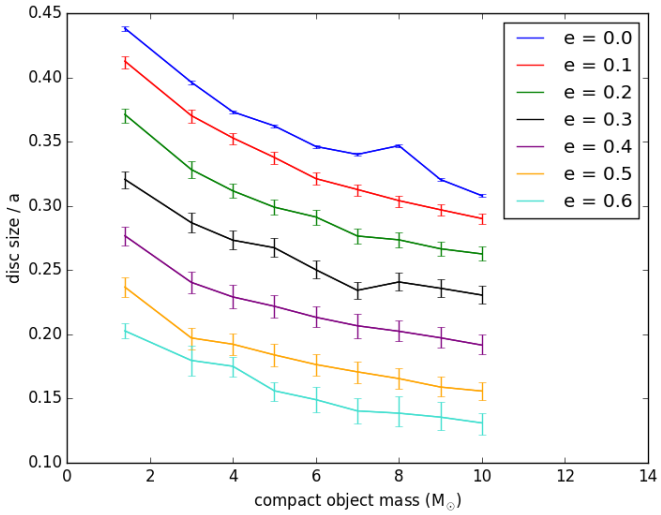

Figure 6.4: The size of the Be star's decretion disc normalised by the semi-major axis, a, for all systems. Disc size is taken to be the radius within which 90% of all the particles are contained. Periastron distance is the same for all the simulations.

axis, a, as this removes dependence on the size of the orbit. The Be star's disc is truncated at smaller (non-dimensional) radii for higher orbital eccentricities.

Figure 6.5 shows the base gas density for all systems. For the simulations of $e \leq 0.2$, base gas density increases with M_X. Base gas density decreases by less than a factor of two as M_X increases for $0.2 < e < 0.4$. For $e > 0.4$, base gas density is almost constant.

6.2.3 X-ray luminosity

The relative difference in X-ray luminosity between Be/BH binaries and Be/NS binaries can be estimated using the mass capture of the compact object. For simplicity, it is assumed that all particles captured by the compact object are accreted instantaneously. This yields X-ray luminosities per unit time. It should be noted that all luminosities in this chapter are calculated from steady state discs and thus, if there were any kind of increase in mass ejection in such a system the X-ray luminosity would be higher. In the case of a giant outburst (see Section 1.4), the system would become considerably brighter than what is considered in this chapter. X-ray luminosity is calculated using

$$L_X = \frac{GM_X\dot{M}}{R_X} \tag{6.3}$$

for neutron star binaries and

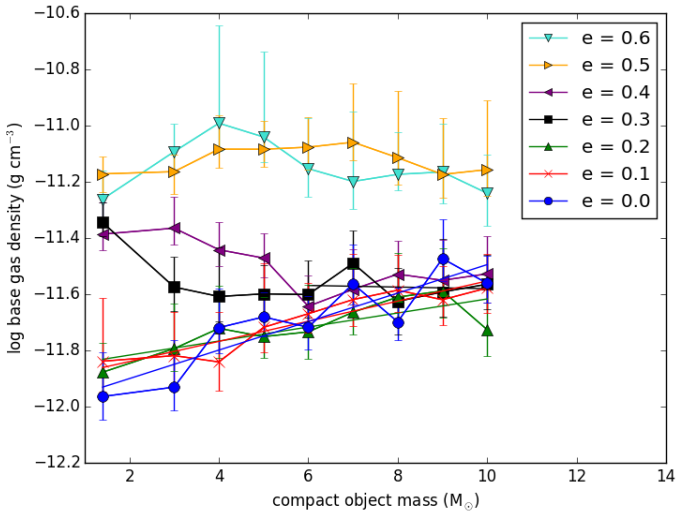

Figure 6.5: Base gas density of the disc as a function of M_X. Vertical bars show the range of density around an orbit, and points show the average over the orbit.

$$L_X = \eta \dot{M} c^2 \tag{6.4}$$

for black hole binaries. Here, $\dot{M}$ is the rate of accretion and η is the conversion efficiency of the rest mass energy of accreted matter into radiation, where $\eta = 0.1$ is adopted in this chapter (Frank et al., 2002). The number of captured particles is converted into solar masses using $M/M_\odot = 2.867 \times 10^{-15} \times N$, where N is the number of particles. Assuming that all matter is converted into an X-ray luminosity instantaneously is a considerable simplification. There is almost certainly an accretion disc involved in accreting Be/X-ray binary systems. Not only would an accretion disc alter the rate at which matter falls onto the compact object but it would interact with any matter in the Be star's disc at periastron.

The maximum measured value of L_X over 5 orbits is defined as the peak luminosity. The average luminosity is the median value of the same 5 orbits. Figures 6.6 and 6.7 show the peak and average L_X for all simulations. The bars on the plots show $\sqrt{N}$ where N is the number of captured particles converted into a luminosity. For the binaries with $e < 0.2$, L_X falls with increasing M_X. For systems of $e \leq 0.2$, the number of captured particles is small. Thus, although L_X varies with M_X, the variations are up to 5000 times smaller than those for higher eccentricities. Peak and average luminosity have a similar dependence on M_X. There is up to an order of magnitude difference between the peak luminosity of a neutron star and a $10\mathrm{M}_\odot$ black hole simulation of equal eccentricity. When comparing simulations of differing eccentricity, this disparity is three orders of magnitude.

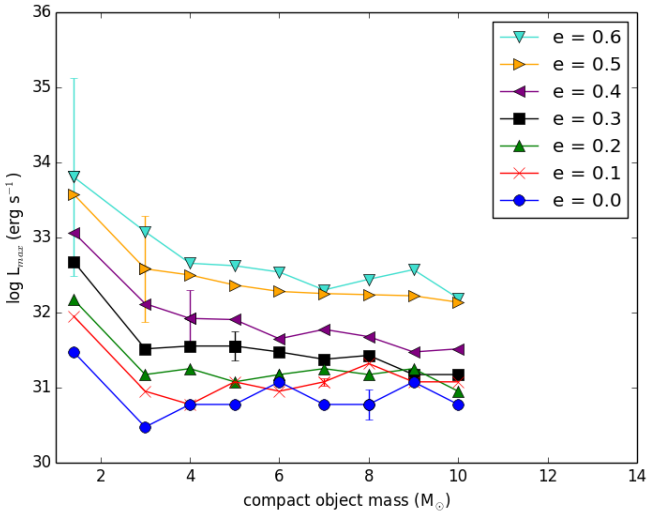

Figure 6.6: The peak daily X-ray luminosity around an orbit. Errorbars show $\sqrt{N}$ where N is the number of particles captured and converted into an X-ray luminosity (see text).

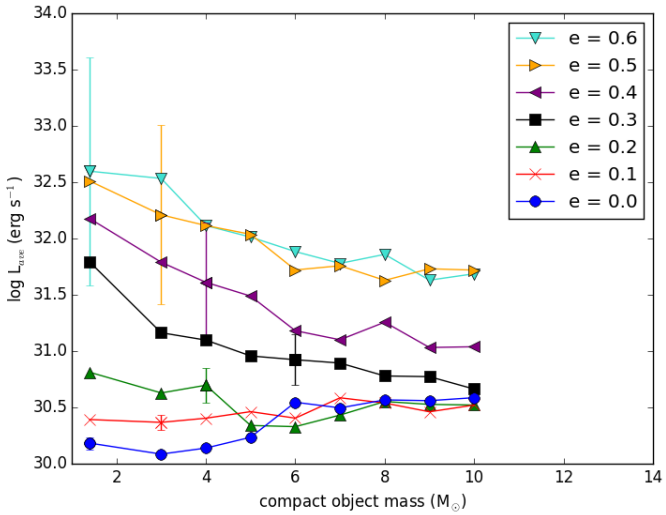

Figure 6.7: The average daily X-ray luminosity around an orbit. Errorbars show $\sqrt{N}$ where N is the number of particles captured and converted into an X-ray luminosity (see text).

Stellar wind accretion

The model in this chapter does not include accretion from the stellar wind of the Be star. In Be/X-ray binaries, it is typically expected that the Be star's circumstellar disc will be the dominant source of matter for accretion onto the compact object. However, if the mass ejection rate of the star is low enough the disc may be more sparse than the stellar wind.

In this section, the Bondi-Hoyle accretion rate (Hoyle and Lyttleton, 1939; Bondi, 1952; Bondi and Hoyle, 1944) is used to calculate an approximate accretion rate and luminosity for the systems in this chapter. This rate is given by

$$\dot{M} \approx \frac{2\pi G^2 M^2 \rho}{(c_{\rm s}^2 + v_{\rm CO}^2)^{3/2}}, \tag{6.5}$$

where ρ is the density of the material that surrounds the compact object, $c_{\rm s}$ is the speed of sound of the surrounding material and $v_{\rm CO}$ is the compact object's velocity. Shima et al. (1985) suggested this should be a factor of two greater as determined by numerical calculations. This treatment is used when considering a compact object that is travelling through the interstellar medium and assumes that the material enters free-fall at a given radius from the compact object.

The calculation of density should be done using models that include thermal or radiation pressure and hydrodynamics (Johnstone et al., 2015). Winds can vary over the surface of the star and can even clump, leading to large fluctuations in the density. For a simple calculation, the base density at the surface of the star is assumed to be 10^{-13} g cm^{-3} (Puls, Vink and Najarro, 2008) and then falls with radius as $(r/R_*)^{-3}$.

Assuming a distance of 80 solar radii (the approximate periastron distance of the systems in this chapter) and a stellar wind outflow rate of $10^{-7} M_\odot \mathrm{yr}^{-1}$, the Bondi-Hoyle accretion rate is $\sim 8 \times 10^{-15} M_\odot \mathrm{yr}^{-1}$. Using equations 6.3 and 6.4, the corresponding luminosities are $\sim 8 \times 10^{31}$ erg s^{-1} and $\sim 4 \times 10^{31}$ erg s^{-1} for neutron stars and black holes, respectively.

Note that for MWC 656, the periastron distance is larger and therefore the predicted luminosity from the stellar wind is ~ 3 times smaller. This is ten times smaller than the maximum X-ray luminosity observed for MWC 656. However, the stellar wind can be stronger than assumed here and the density of the stellar wind is simplified considerably here.

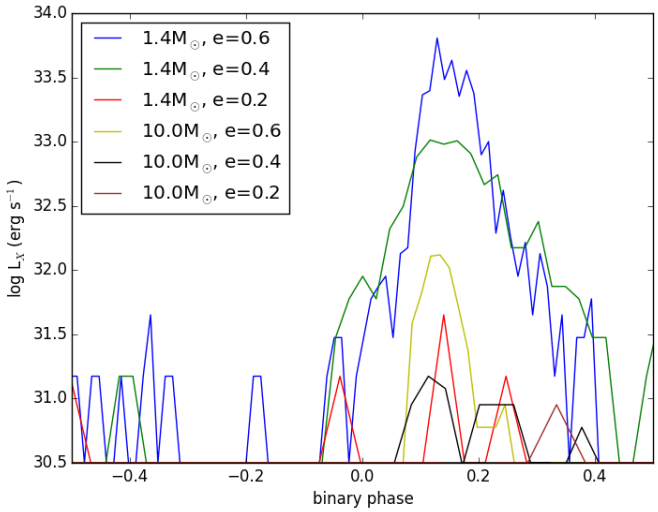

Figure 6.8: The logarithm of X-ray luminosity around an orbit for the neutron star and the $10M_{\odot}$ black hole with eccentricities $e = 0.2, 0.4$, and 0.6. Periastron is at a binary phase of 0.0. The peak mass capture for all systems lies at a binary phase ∼0.15.

6.2.4 Binary phase of accretion

It is often assumed that the maximum X-ray luminosity occurs at periastron. However, there may be a delay between these two events. Previous work on neutron star mass capture by Okazaki and Hayasaki (2004) shows there is a delay between periastron and peak mass capture. Figure 6.8 shows the relation between X-ray luminosity and binary phase. The peak X-ray luminosity occurs at a binary phase of ∼0.15. Note that accretion onto the compact object is not modelled accurately, and therefore, a precise estimate of timing of peak X-ray luminosity cannot be made. Nevertheless, this result confirms the delay found in previous work and reveals that there is no dependence on M_X.

Increasing eccentricity results in higher X-ray luminosities over shorter ranges of orbital phase. This can be understood from the discussion of truncation in Section 6.2.2. The smaller gap between the truncated disc and periastron in systems of higher eccentricity leads to a higher rate of mass capture. Because more massive compact objects produce more significant truncation of the decretion disc, there is a shorter period during which accretion takes place.

6.3 Modelling MWC 656

The maximum observed X-ray luminosity of MWC 656 is 500 times smaller than the faintest Be/NS binary in the sample shown in Table 6.1 and Figure 6.2. It is almost 10,000 times fainter than Be/NS binaries of similar eccentricity. We see from Figure 6.6 that, for a given eccentricity, a change in M_X can only produce a change

Table 6.3: Properties of the MWC 656 simulation.

Disc size / a	0.28 ± 0.1
ρ_0 ($\mathrm{g\,cm^{-3}}$)	$(8.4 \pm 1.4) \times 10^{-12}$
L_{max} ($\mathrm{erg\ s^{-1}}$)	$(3.0 \pm 0.7) \times 10^{32}$
L_{ave} ($\mathrm{erg\ s^{-1}}$)	$(5.1 \pm 0.6) \times 10^{31}$

in L_{max} of ∼20-30.

A simulation of MWC 656 was performed to use as a comparison between the simulations and the sample data. Note that the periastron distance of MWC 656 is ∼2 times larger than the periastron distance for simulations shown in Section 6.2. The base gas density, normalised disc size, peak and average X-ray luminosity are shown in Table 6.3.

The base gas density is comparable to the highest values seen in the other simulations. The normalised size of the disc is smaller than would be expected for a $5M_\odot$ black hole with an eccentricity of 0.1 and thus does not remain constant when varying periastron distance. In dimensional units, however, the disc of MWC 656 is still larger. Both peak and average X-ray luminosity are higher than would be expected for a $5M_\odot$ black hole with an eccentricity of 0.1. X-ray luminosity increases with periastron distance when using constant mass ejection rate.

Further evidence for the inefficient accretion suggested by Casares et al. (2014) is shown by these simulation data. The peak luminosity is greater than the observed maximum for MWC 656. This is despite the mass ejection being less than average for a Be star. A larger periastron distance and, in turn, a less efficient truncation of the disc, leads to a denser disc which allows the accretion of more matter onto the compact object.

This simulation of MWC 656 still has a lower X-ray luminosity than the majority of the other simulated accreting neutron stars. However, the results cannot explain the huge difference between the observed L_X of MWC 656 and the known NS systems. This implies the need for some other explanation as to why MWC 656 is extremely faint. A difference in accretion efficiency is the most likely explanation. While the standard type of accretion was assumed in this chapter, a Radiatively Inefficient Accretion Flow, or RIAF, is likely to occur for such a low accretion rate regime, where the efficiency of accretion has been shown to be as low as $\eta \sim 0.0045$ (Abramowicz et al., 2001). The X-ray luminosity from a RIAF with the simulated accretion rate for MWC 656 would therefore be $\sim 10^{30}\mathrm{erg\ s^{-1}}$, which leads to a similar discrepancy between the X-ray luminosity of MWC 656 and the brightest neutron stars for the simulations and observations.

6.4 Conclusions

In this chapter, a possible difference in X-ray luminosity between Be/NS and Be/BH binaries was investigated. Simulations of Be/X-ray binaries with varying compact object mass, M_X, were performed. It is shown that disc size, base gas density and X-ray luminosity are dependent on the mass of the compact object.

The normalised disc size decreases by up to a factor of 1.5 with M_X, confirming the more efficient truncation of the Be star disc black holes in Be/X-ray binaries. Base gas density increases with M_X by a factor of $\sim$2.5 for systems of $e \leq 0.2$. For systems of $0.2 < e < 0.4$, variations are of the same order but decrease with M_X. Above $e = 0.4$, the relation is closer to constant.

The simulations discussed above predict that the most luminous X-ray systems are ones with high eccentricity and a Be star circumstellar disc that extends to or outside the periastron distance. However, black hole binaries that fulfill both these criteria may still be fainter than neutron star systems that satisfy only one.

With the results in this chapter and in the absence of X-ray pulsations, it is extremely difficult to distinguish between a black hole and a neutron star in a Be/X-ray binary with X-ray observations alone. However, with knowledge of the orbital parameters and the size of the disc it is plausible. Be/X-ray binaries with a $10M_\odot$ black hole can be more than 10 times fainter than a neutron star system with the same accretion efficiency and periastron distance.

Chapter 7

Conclusions

The aim of this thesis is to use computational techniques to investigate the dynamical evolution of the decretion disc of the Be star in Be/X-ray binaries. It is found that there are still some discrepancies between some of the physical parameters inferred from observations and those seen in theoretical simulations.

The work in this thesis was performed using a three-dimensional smoothed particle hydrodynamics (SPH) code. The disc itself is made up of a sea of SPH particles with individual timesteps that are varied depending on the required time resolution at the particle's position in the disc. The code implements the viscous decretion disc (VDD) model that extends the standard Shakura-Sunyaev α-model by assuming a source of disc material at the Be star's surface. This model has been shown to be capable of reproducing the dynamical properties of decretion discs.

Chapter 4 considers some of the important characterstics of the Be star's circumstellar disc and how they vary under the alteration of a number of simulation parameters. A number of relations between three disc properties (the base gas density of the Be star's disc, the neutron star's accretion rate and the size of the disc) and five simulation parameters (the viscosity of the disc, the mass ejection rate of the Be star, the orientation of the disc and the orbital period and eccentricity of the binary) are presented. The same simulations are applied to test the observational relationships between the disc's size, the orbital period and the semi-major axis. The simulations agree with the observations.

The Be/NS binary, SXP 5.05, was then targeted using the same computational methods. In 2013, SXP 5.05 underwent a large optical outburst that is unlike any other behaviour that has been seen in the object to date. The I-band magnitude of the system varies by ~ 0.4 which implies a relative increase in the disc that is rare amongst Be systems in general. It is found that the observational features of the system can be broadly reproduced in multiple wavelengths by assuming large changes in the mass-loss of the Be star and the viscosity in the disc. Although the

simulations are capable of explaining the observational features by evolving the mass-loss and viscosity, this cannot explain the source of the high rate of mass ejection from the Be star. As the variations in mass-loss are considered to arise from constructive interference between pulsation modes of the star, any outbursts should be periodic. Thus, either there is some other physical mechanism playing a role in this event or another such outburst should be expected from the Be star in the future.

Another discrepancy between the theory and observations of Be/X-ray binaries is the number of observed Be/black hole binaries. There is only one confirmed binary system containing a Be star and a black hole, MWC 656. Theory predicts the evolution of a small number of these systems but it is unlikely that none of them have been observed without some other contributing reason. It has been suggested that this additional reason is the faintness of black hole binaries relative to neutron star binaries and this is supported by the low luminosity of MWC 656. Simulating these systems confirms this suggestion; black holes cause greater tidal truncation of the Be star's disc and hence these systems have smaller discs relative to neutron stars. The smaller disc causes less material to be accreted at periastron and yields a fainter X-ray source. Thus, to detect more of these systems, we must look at lower luminosity ranges.

7.1 Future work

The future of the research in this field is in the combination of multiple computational techniques. There are codes that exist, such as the code used for the work in this thesis (Brown et al., 2018), that are capable of dynamically evolving the Be star's disc and can reproduce a large number of observable effects. There are also available radiative transfer techniques that are capable of calculating the internal properties of the gas, such as the temperature distribution and hydrogen levels. The code most widely used for this is the Monte Carlo radiative transfer code, HDUST (Carciofi et al., 2006; Carciofi and Bjorkman, 2008).

Despite the dependence of the dynamics of the disc on its properties, many hydrodynamical models assume an isothermal disc (Bjorkman, 1997; Porter, 1999; Okazaki, 2001) for simplicity. Ideally, the internal properties of the circumstellar disc would be determined at each timestep and then used for the calculation of the next step of the hydrodynamical evolution.

The combination of a 1D hydrodynamical code and radiative transfer code has been applied to isolated Be star discs by Rímulo et al. (2018) allowing constraints to be put on the viscosity of decretion discs and the mass and angular momentum loss of the Be star. Ghoreyshi et al. (2018) applied indentical methods to the isolated Be

star system ω CMa and managed to successfully fit the V-band light curve. Implementing both methods in three dimensions is computationally expensive but has been performed by Panoglou et al. (2018) showing good evidence for phase-locked variations of emission lines. These are some of the earliest attempts to form a complete model of the decretion disc. The success of these three works indicates how powerful these techniques can be and further work needs to be done to develop them.

With a three-dimensional code that implements both of these techniques, many specific Be/X-ray binaries should be targeted. It will then be possible to further understand a large number of events, such as giant outbursts, that occur from interactions between the decretion disc and compact object in Be/X-ray binaries. Finally, models that simulate the NRPs of the central star itself should be added, integrating the mass ejection mechanism into the simulation. This would yield a code that can simulate the entirety of any Be star system.

The resources required to power such a program would depend heavily on the desired runtime and accuracy, the computing power available, the level of optimisation within the code and the effectiveness of the parallelisation in the code. Firstly, consider the code used in this thesis, a 3D SPH code that has OpenMP implementation and an above average optimisation within the code. A simulation with 8 processors and 10,000 particles will take a few hours to run from no disc to a disc in a steady state. In Chapter 3, the speed-up of the code was considered for this code and is shown in Figure 3.8. The runtime's dependence on the number of simulation particles, N, used (particles are equivalent to resolution) is, at worst, N^2. Note there are a number of algorithms implemented in the code that reduce this increase in runtime. Just considering these two factors, a simulation with 8 processors and 10,000 particles can run up to two thousand times faster than a simulation with 1 processor and 200,000 particles. The use of Message Passing Interface (MPI) can extend the parallelisation of the code to a much larger number of processors. The exact speed-up of this is not clear without extensive testing, especially as it can be used in conjunction with OpenMP.

The real difficulty is the implementation of a radiative transfer code as it has to be run at multiple times throughout the simulation. Once again, this part of the program would be dependent on the five aforementioned parameters (runtime, accuracy, computing power, optimisation and parallelisation) but it would be additionally be dependent on how often it is required to be run in between timesteps of the SPH code. The dependence of the dynamics of the disc on the temperature profile determines how frequently the radiative transfer code must be used. This would have to be investigated through testing. Assuming the accuracy used for recent work in the field of radiative transfer modelling of Be star discs (Ghoreyshi et al., 2018), HDUST can be expected to take hours to a day which is

heavily dependent on the number of wavelengths which are modelled. Given that there can be hundreds of thousands of timesteps for the simulation to reach a steady state from no disc, it can be assumed that there will be a large number of radiative transfer simulations. If one run is required per every 100 timesteps, a minimum of 1000 more hours is added by implementing this code. This means that it requires a comparable computational time to the SPH code but as radiative transfer methods are much more capable of parallelisation there is more opportunity to speed it up.

Adding code that would model the Be phenomenon is difficult to benchmark as it is still not completely certain how it works. However, it would be required to run at every timestep during the simulation as it defines the dynamics of the disc in the inner regions and regulates the mass ejection rate of the Be star.

The targets of such a code should include primarily systems that have a large amount of information known about them and thus, the fewest unknowns must be accounted for. It is also important to contain some isolated Be star systems so that any observable effects that arise due to the Be star itself can be separated and compared to binary systems. The isolated Be star that I think would be best to use is ω CMa. A great deal of work has been done on it already as its parameters are well known (Ghoreyshi et al., 2018). This previous work would be very useful in comparing the accuracy of the new code and it would prove that it can reproduce the results. As for Be/X-ray binaries I would choose SXP 5.05 as one possiblity. A lot is known about this system and completely replicating the extremely dynamic event discussed in Chapter 5 would provide confidence in any model. V635 Cas is a well known system and has also been modelled repeatedly in the past, for example by Negueruela and Okazaki (2001) and hence would be a great target. A particularly good system for investigating giant outbursts (a very important aspect of Be/X-ray binaries) is $A0535 + 262$ because its magnetic field is insufficient to steam the flow of matter being accreted (Okazaki, 2013). This removes the need to disentangle effects caused by the magnetic field from those created by the warped disc. However, the power of a complete model lies in its ability to correctly explain the entirety of what we can observe and hence the aim would be to eventually model the entire population of Be/X-ray binaries.

Bibliography

Abramowicz M. A., Igumenshchev I. V., Quataert E. and Narayan R., 2001, Astrophys. J., 565, 1101

Adams F. C., Lada C. J. and Shu F. H., 1987, Astrophys. J., 312, 788

Aerts C., Christensen-Dalsgaard J. and Kurtz D. W., 2010, Asteroseismology. Springer

Albrecht P., 1996, The Runge-Kutta theory in a nutshell, SIAM J. Numer. Anal., 33, 1712

Baade D., 1988, Nonradial Pulsations and the be Phenomenon. In: Cayrel de Strobel G, Spite M (eds), IAU Symposium, 132, 217

Baade D. et al., 2018, 3rd BRITE Science Conference, 8, 69

Bate M. R., Bonell I. A. and Price N. M., 1995, MNRAS, 277, 362

Batygin K., 2012, Nature, 491, 418

Belczynski K. and Ziolkowski J., 2009, Astrophys. J., 707, 870

Benz W., 1990, Numerical Modelling of Nonlinear Stellar Pulsations Problems and Prospects, 269

Benz W., Bowers R. L., Cameron A. G. W. and Press, W. H., 1990, ApJ, 348, 647

Blaauw A., 1961, Bull. Astron. Inst. Netherlands, 15, 265

Bolton C. T. 1982, IAU Symposium, 98, 181

Bondi H., 1952, MNRAS, 112, 195

Bondi H. and Hoyle, F., 1944, MNRAS, 104, 273

Boss A. P. and Black D. C., 1982, ApJ, 258, 270

Boyle C. B. and Walker, I. W., 1986, MNRAS, 222, 559

Bjorkman J. E. 1997, Stellar Atmospheres: Theory and Observations, eds. J. P. De Greve, R. Blomme and H. Hensberge (Berlin: Springer Verlag), Lecture Notes in Physics, 497, 239

Brown R. O., Ho W. C. G., Coe M. J. and Okazaki A. T., 2018, MNRAS, 477, 4810

Brown R. O., Coe M. J., Ho W. C. G. and Okazaki A. T., 2019, MNRAS, 486, 3078

Campana S. et al., 2001, Astrophys. J., 561, 924

Cannizzo J. K., 1993, Astrophys. J., 318, 419

Cappellaro E. and Turatto M., 2001, ASSL, 264, 199, ASSL..264

Carciofi A. C. and Bjorkman J. E., 2006, ApJ, 639, 1081

Carciofi A. C. et al., Astrophys. J., 652, 1617

Carciofi A. C. et al., 2007, Astrophys. J., 671, 49

Carciofi A. C. and Bjorkman J. E., 2008, ApJ, 684, 1374

Carciofi A. C. et al., 2008, ApJ, 676, 41

Carciofi A. C. et al., 2009, A&A, 504, 915

Carciofi, A. C. 2011, in Active OB Stars, eds. C. Neiner, G. Wade, G. Meynet and G. Peters, IAU Symp., 272, 325

Carroll S. M., 2004, Spacetime and geometry / Sean Carroll. San Francisco, CA, USA: Addison Wesley

Casares et al., 2014, Nature, 505, 378

Cassinelli J. P. et al., 1994, ApJ, 421, 705

Choudhury S. et al., 2018, MNRAS, 475, 4279

Coe M. J. and Kirk J., 2015, MNRAS, 452, 1, 969

Coe M. J. et al., 2013, The Astronomer's Telegram, No. 5547

Coe M. J. et al., 2015, MNRAS, 447, 3, 2387

Coe M. J. et al., 2019, MNRAS, 485, 1864

Coleiro A. et al., 2013, A&A, 560, A108

Collins G. W. II, 1987, IAU Colloq., 92: Physics of Be Stars, 3

Conti P.S., 1978, ARA&A, 16, 371

Conti P. S. and Leep E. M., 1974, Astrophys. J. 193, 113

Cox A. N., 2000, Allen's Astrophysical Quantities (New York: Springer-Verlag)

Cox J. P. and Giuli R. T., 1968, Principles of stellar structure, by J.P. Cox and R. T. Giuli. New York: Gordon and Breach

Delaa O. et al., 2011, A&A, 529, A87

Doazan V., Bourdonneau B., Rusconi L., Sedmak G. and Thomas R. N., 1987, A&A, 182, 25

Dougherty S. M. and Taylor A. R., 1992, Nature, 359, 808

Draper Z. H. et al., 2011, Astrophys. J., 728, 40

Evrard A. E., 1988, MNRAS, 235, 911

Faes D. M. et al., 2013, A&A, 555, 76

Fontaine G., Brassard P. and Bergeron P., 2001, PASP, 113, 409

Frank J., King A. and Raine D. J., 2002, Accretion Power in Astrophysics, pp. 398. ISBN 0521620538. Cambridge, UK: Cambridge University Press, February 2002.

Frémat Y., Zorec J., Hubert A. M. and Floquet M., 2005, A&A, 440, 305

Fryer C. L., 2004, Astrophys. J., 601, 175

Fu W., Lubow S. H. and Martin R. G., 2017, Astrophys. J., 835, 29

Gingold R. A. and Monaghan J. J., 1977, MNRAS, 181, 375

Gingold R. A. and Monaghan J. J., 1982, Journal of Computational Physics, 46, 429

Gehrz R. D., Hackwell J. A. and Jones T. W., 1974, Astrophys. J., 191, 675

Ghoreyshi M. R. et al., 2018, MNRAS, 479 (2), 2214

Grady C. A. et al., 1987, Astrophys. J., 320, 376

Grady C. A. et al., 1989, Astrophys. J., 339, 403

Grudzinska M. et al., 2015, MNRAS, 452, 2773

Guinan E. F. and Hayes D. P., 1984, Astrophys. J., 287, 39

Hameury J. M. and Lasota J. P., 2002, A&A, 394, 231

Hanuschik R. W., 1989, APSS, 161, 61

Harris J. and Zaritsky D., 2006, AJ, 131, 2514

Haubois X., Carciofi A. C., Rivinius T., Okazaki A. T. and Bjorkman J. E., 2012, Astrophys. J., 756, 156

Hayasaki K. and Okazaki A. T., 2004, MNRAS, 350, 971

Heinzeller D. and Duschl W. J., 2007, MNRAS, 374, 1146

Heger A. et al., 2003, Astrophys. J., 591, 288

Hernquist L. and Katz N., 1989, ApJS, 70, 419

Horne K. and Marsh T. R., 1986, Monthly Notices of the Royal Astronomical Society, 218, 761

Horne K., 1995, A&A, 297, 273

Hoyle F. and Lyttleton R. A., 1939, Proc. Cam. Phil. Soc., 35, 405

Huang S. S., 1972, ApJ, 171, 549

Hummel W. and Vrancken M., 2000, A&A, 359, 1075

Iben I. Jr. and Livio M., 1993, PASP, 105, 1373

Iben I. Jr., Tutukov A. V. and Fedorova A. V., 1997, ApJ, 486, 955

Innanen K. A., Zheng J. Q., Mikkola S. and Valtonen M. J. 1997, AJ, 113, 1915

Janka H.-T. et al., 2005, ASPC, 332, 372

Jaschek M. and Egret D., 1982, Proceedings IAU Symposium No. 98, Dordrecht: D. Reidel Publishing Co., 261

Johnstone C. P. et al., 2015, A&A, 577, 27

Jones C. E., Sigut T. A. A. and Porter, J. M. 2008a, MNRAS, 386, 1922

Jones C. E., Tycner C., Sigut T. A. A., Benson J. A. and Hutter D. J., 2008b, Astrophys. J., 687, 598

Kaper L., 2001, ASSL, 125, 264

Kaper L. and van der Meer A., 2007, Massive Stars in Interactive Binaries, 367, 447

King A. R., Livio M., Lubow S. H. and Pringle J. E., 2013, MNRAS, 431, 2655

Kippenhahn R. and Weigert A., 1990, Stellar Structure and Evolution, Springer-Verlag Berlin Heidelberg New York.

Kiseleva L. G., Eggleton P. P. and Mikkola S. 1998, MNRAS, 300, 292

Klus H., Ho W. C. G., Coe M. J., Corbet R. H. D. and Townsend L. J., 2014, MNRAS, 437, 4, 3863

Klement R. et al., 2015, A&A, 584, 85

Kozai Y., 1962, AJ, 67, 591

Kraus S. et al., 2012, Astrophys. J., 744, 19

Krtička J., 2014, A&A, 564, A70

Kudritzki R. P. and Puls J., 2000, ARA&A, 38, 613

La Palombara N. et al., 2009, A&A, 505, 947

Lai D., Wang C. and Han J., 2006, Chinese Journal of Astronomy and Astrophysics Supplement, 6, 241

Lee U., Osaki Y. and Saio H. 1991, MNRAS, 250, 432

Lee U., 2012, MNRAS, 420, 2387

Lewin W. H. G. and Joss P. C., 1983, in Accretion-Driven Stellar X-ray Sources, eds. Lewin W. H. G. and van den Heuvel E. P. J., Cambridge University Press.

Lidov M. L., 1962, Planet. Space Sci., 9, 719

Li K. L., Kong A. K. H., Charles P. A., et al., 2012, ApJ, 761, 99

Liu Q. Z., van Paradijs J. and van den Heuvel E. P. J., 2006, A&A, 455, 1165

Lodato G. and Price D. J., 2010, MNRAS, 405, 1212

Lucy L. B., 1977, The AJ, 82, 1013

Manchester R. N., 2017, J. Phys. Conf. Ser., 932, 012002

Marsh T. R., 1987, MNRAS 228, 779

Martin R. G., Tout C. A. and Pringle J. E., 2009, MNRAS, 397, 1563

Martin R. G., Tout C. A. and Pringle J. E., 2010, MNRAS, 401, 1514

Martin R. G., Pringle J. E., Tout C. A. and Lubow, S. H., 2011, MNRAS, 416, 2827

Martin R. G., Nixon C., Lubow S. H., Armitage P. J., Price D. J., Doğan S., King A., 2014, ApJ, 792, 33

Martin R. G., Nixon C., Armitage P. J., Lubow S. H. and Price D. J. 2014, ApJL, 790, 34

Massi M., Migliari S. and Chernyakova M., 2017, MNRAS, 468, 3689

Mazzali P. A., Röpke F. K., Benetti S. and Hillebrandt W., 2007, Sci, 315, 825

McAlister H. A. et al., 2005, Astrophys. J., 628, 439

McGill M. A., Sigut T. A. A. and Jones C. E. 2011, ApJ, 743, 111

McSwain M. V., Huang W., Gies D. R., Grundstrom E. D. and Townsend R. H. D., 2008, Astrophys. J., 672, 590

Meglicki Z., Wickramasinghe D. and Bicknell G. V., 1993, MNRAS, 264, 691

Meilland A. et al., 2007a, A&A, 464, 59

Meilland A. et al., 2007b, A&A, 464, 59

Meilland A. et al., 2012, A&A, 538, A110

Miller J. M., Fabian A. C. and Miller M. C., 2004, Astrophys. J., 614, 117

Monaghan J. J. and Gingold R. A., 1983, Journal of Computational Physics, 52, 374

Monaghan J. J., 1985, Comput. Phys. Rep., 3, 422

Monaghan J. J. and Lattanzio J. C., 1985, A&A, 149, 135

Monaghan J. J., 1989, Journal of Computational Physics, 82, 1

Monaghan J. J., 1992, ARA&A, 30, 543

Naze Y. et al., 2011, VizieR Online Data Catalog, 219,

Negueruela I., 2010, High Energy Phenomena in Massive Stars, 422, 57

Negueruela I. and Okazaki A. T., 2000, IAU Colloq. 175: The Be Phenomenon in Early-Type Stars, 214, 713

Negueruela I. and Okazaki A. T., 2001, A&A, 369, 108

Negueruela I., Steele I. A. and Bernabeu G., 2004, Astronomische Nachrichten, 325, 749

Nelson R. and Papaloizou J. C., 1994, MNRAS, 270, 1

Novikov I. D. and Thorne K. S., 1973, Black Holes (Les Astres Occlus), 343

Okazaki A. T., 1991, PASJ, 43, 75

Okazaki A. T., 1996, Publications of the Astronomical Society of Japan, 48, 305

Okazaki, A. T. 2001, PASJ, 53, 119

Okazaki A. T. and Negueruela I., 2001, A&A, 377, 161

Okazaki A. T. and Negueruela I., 2001, X-ray Astronomy 2000, 234, 281

Okazaki A. T., Bate M. R., Ogilvie G. I. and Pringle J. E., 2002, MNRAS, 337, 967

Okazaki A. T. and Hayasaki K., 2004, Revista Mexicana de Astronomia y Astrofisica (Serie de Conferencias), 20, 144

Okazaki A. T., 2007, Active OB-Stars: Laboratories for Stellare and Circumstellar Physics, 361, 230

Okazaki A. T., Hayasaki K. and Moritani Y., 2013, PASJ, 65, 41

Owocki S. P., 2006, ASP Conference Series, 355, 219

Özel F. and Freire P., 2016, ARA&A, 54, 401

Panoglou D. et al., 2018, MNRAS, 473, 3039

Papaloizou J. C. B., Savonije G. J. and Henrichs H. F., 1992, A&A, 265, L45

Penrod G. D., 1986, PASP, 98, 35

Pfahl E. et al., 2002, Astrophys. J., 574, 364

Piro A. L., Thompson T. A. and Kochanek C. S., 2014, MNRAS, 438, 3456

Podsiadlowski Ph. et al., 2003, MNRAS, 341 (2), 385

Poeckert R. and Marlborough J. M., 1982, Astrophys. J., 252, 196

Pollmann E., 2012, Information Bulletin on Variable Stars, 6023, 1

Porter J. M., 1999, A&A, 348, 512

Porter J. M. and Rivinius T., 2003, PASP, 115, 1153

Postnov K. A. et al., 2014, MNRAS, 446 (1), 1013

Price D. J. and Federrath C., 2010, MNRAS, 406, 1659

Pringle J. E., 1981, Annu. Rev. A&A, 19, 137

Prinja R. K., 1989, MNRAS, 241, 721

Puls J., Vink J. S. and Najarro F., 2008, A&A Rev., 16, 209

Quirrenbach A., Buscher D. F., Mozurkewich D., Hummel C. A. and Armstrong J. T., 1994, A&A, 283, 13

Quirrenbach A. et al.,1997, Astrophys. J., 479, 477

Rajoelimanana A. F., Charles P. A., Meintjes P. J., et al., 2017, MNRAS, 464, 4133

Raguzova N. V. and Lipunov V. M., 1999, A&A, 349, 505

Raguzova N. V., 2001, A&A, 367, 848

Raguzova N.V. and Popov S.B., 2005, Astron. Astrophys. Transactions, 24, 151

Rappaport S. and van de Heuvel E. P. J., 1982, IAU Symposium No. 98 *Be Stars* (M. Jaschek and H.G. Groth, Editors), Reidel, Dordrecht, 327

Rappaport S., Verbunt F. and Joss P. C., 1983, ApJ, 275, 713

Reese D. R., MacGregor K. B., Jackson S., Skumanich A. and Metcalfe T. S., 2009, A&A, 506, 189

Reese D. R., Prat V., Barban C., van't Veer-Menneret C. and MacGregor K. B., 2013, A&A, 550, A77

Reig P., Fabregat J., Coe M. J., 1997, A&A, 322, 193

Reig P. and Roche, P., 1999, MNRAS, 306, 100

Reig P., 2011, Ap&SS, 332, 1

Reig P. and Nespoli E., 2013, A&A, 551, A1

Reig P. et al., 2016, A&A, 590, A122

Ribó et al., 2017, Astrophys. J., 835, 2, 33

Rímulo L. R. et al., 2018, MNRAS, 476, 3555

Rivinius T. et al., 1998, Predicting the Outbursts of the Be Star μ Cen. In: Kaper L., Fullerton A. W. (eds), Cyclical Variability in Stellar Winds, p207

Rivinius T., 2000, ASP Conference Series, 214, 228

Rivinius T., Baade D., Štefl S, and Maintz M.,2001, A&A, 379, 257

Rivinius T., Baade D. and Štefl S., 2003, A&A, 411, 229

Rivinius T., Štefl S. and Baade D., 2006, A&A, 459, 137

Rivinius T., Carciofi A. C. and Martayan C., 2013, A&A Review, 21, 69

Roberts T., Earnshaw H., Walton D., Middleton M. and Mateos S., 2017, The X-ray Universe 2017, 192

Ružđjak D. et al., 2009, A&A, 506, 1319

Samus N. N., Kazarovets E. V., Durlevich O. V., Kireeva N. N. and Pastukhova E. N., 2009, VizieR Online Data Catalog, 1

Schmidt-Kaler Th., 1982, in Schaifers K., Voigt H. H., eds, Landolt-Börnstein, group VI, Vol 2, subvol. b, Stars and Star Clusters. Springer, Berlin, Heidelberg, New York, p. 17

Schurch M. P. E. et al., 2008, MNRAS, 392, 1, 361

Schwarzschild K., 1916, Über das Gravitationsfeld eines Massenpunktes nach der Einsteinschen Theorie, Sitzungsberichte der Deutschen Akademie der Wissenschaften zu Berlin, Klasse fur Mathematik, Physik, und Technik, 189

Scowcroft V. et al., 2016, ApJ, 816, 49

Secchi A., 1866, Astronomische Nachrichten, 68, 63

Shakura N. I. and Sunyaev R. A., 1973, A&A, 24, 337

Sheikh S. I. et al., 2006, JGCD, 29, 49

Shima E., Matsuda T., Takeda H. and Sawada K., 1985, MNRAS, 217, 367

Shaviv N. J., 2002, AIPC, 637, 259

Sigut T. A. A. and Jones C. E., 2007, Astrophys. J., 668, 481

Silaj J., Jones C. E., Tycner C., Sigut T. A. A. and Smith A. D., 2010, Astrophys. J. Suppl. Ser., 187, 228

Silaj J. et al., 2014, Astrophys. J., 795, 1, 12

Slettebak A., 1986, Publ. Astron. Soc. Pac., 98, 867

Slettebak A., 1988, Publ. Astron. Soc. Pac, 100, 770

Smith N. and Owocki S. P., 2006, Astrophys. J., 645, 45

Sonneborn G. at al., 1988, Astrophys. J., 325, 784

Štefl S. et al., 2003, A&A, 402, 253

Štefl S., Okazaki A. T., Rivinius T. and Baade D., 2007, V/R Variations of Binary Be Stars. In: Štefl S., Owocki S. P., Okazaki A. T. (eds), ASP Conference Series, 361, 274

Štefl S. et al., 2009, A&A, 504, 929

Struve O., 1931, ApJ, 73, 94

Sturm R., Haberl F., Pietsch W. et al., 2012c, A&A, 537, 76

Sun W.-H. and Malkan M. A., 1986, In ESA Proceedings of an International Symposium on New Insights in Astrophysics, 9, 641

Taam R. E. and Sandquist, E. L., 2000, ARA&A, 38, 113

Tauris T. M. and Savonije G. J., 1999, A&A, 350, 928

Tauris T. M. and van den Heuvel E. P. J., 2006, Compact stellar X-ray sources, 623

Telting J. H. and Kaper L, 1994, A&A, 284, 515

Touhami Y., Gies D. R. and Schaefer G. H., 2011, Astrophys. J., 729, 17

Townsend R. H. D., Owocki S. P. and Howarth I. D., 2004, MNRAS, 350, 189

Townsend L. J. et al, 2011, MNRAS, 410, 3, 1813

Townsend L. J., Coe M. J., Corbet R. H. D. and Hill A. B., 2011, MNRAS, 416, 2, 1556

Tycner C. et al., 2008, Astrophys. J., 689, 461

van den Heuvel E. P. J., 1994, Saas-Fee Advanced Course 22: Interacting Binaries, 263

van den Heuvel E. P. J., 2004, 5th INTEGRAL Workshop on the INTEGRAL Universe, 552, 185

van den Heuvel E.P.J. and Rappaport S., 1987, IAU Colloquium No. 92 *Physics of Be Stars* (A. Slettebak and T.P. Snow, editors), Cambridge University Press, 291

van Kerkwijk M. H., Waters L. B. F. M. and Marlborough J. M., 1995, A&A, 300, 259

van Kerkwijk M. H., van Paradijs J. and Zuiderwijk E. J., 1995, A&A, 303, 497

Vieira R. G. et al., 2015, MNRAS, 454, 2107

Wade G. A., Grunhut J. H. and MiMeS Collaboration, 2012, ASP Conference Series, 464, 405

Walker G. A. H. et al., 2005, Astrophys. J., 623, 145

Waters L. B. F. M., 1986, A&A, 162, 121

Waters L. B. F. M., Cote J. and Geballe T. R., 1988, A&A, 203, 348

Wheelwright H. E., Bjorkman J. E., Oudmaijer R. D., Carciofi A. C., Bjorkman K. S. and Porter J. M., 2012, MNRAS, 423, 11

Wisniewski J. P., Kowalski A. F., Bjorkman K. S., Bjorkman J. E. and Carciofi A. C., 2007, Astrophys. J., 656, 21

Wisniewski J. P. et al., 2010, Astrophys. J., 709, 1306

Wood K., Bjorkman K. S. and Bjorkman J. E., 1997, Astrophys. J., 477, 926

Zaal P. A., de Koter A., Waters L. B. F. M., Marlborough J. M., Geballe T. R., Oliveira J. M. and Foing B. H., 1999, A&A, 349, 573

Zhang F., Li X.-D. and Wang Z.-R., 2004, Astrophys. J., 603, 663

Ziolkowski J. and Belczynski K., 2011, IAU Symposium, 275, 329

Appendix A

Constants

Table A.1: Table of constants used in this thesis in order of appearance.

Symbol	Description	Value	SI Units
k_{B}	Boltzmann constant	1.38×10^{-23}	$\mathrm{m^2\ kg\ s^{-2}\ K^{-1}}$
m_{H}	mass of a hydrogen atom	1.67×10^{-27}	kg
c	speed of light	2.99×10^{8}	$\mathrm{m\ s^{-1}}$
G	universal gravitational constant	6.67×10^{-11}	$\mathrm{m^3\ s^{-2}\ kg^{-1}}$